

Quantitative Luminescence Imaging of Solar Cells

Vito Konrad Wulfila Huhn

Energie & Umwelt / Energy & Environment Band / Volume 439 ISBN 978-3-95806-363-1



Forschungszentrum Jülich GmbH Institut für Energie- und Klimaforschung IEK-5 Photovoltaik

Quantitative Luminescence Imaging of Solar Cells

Vito Konrad Wulfila Huhn

Schriften des Forschungszentrums Jülich Reihe Energie & Umwelt / Energy & Environment Bibliografische Information der Deutschen Nationalbibliothek. Die Deutsche Nationalbibliothek verzeichnet diese Publikation in der Deutschen Nationalbibliografie; detaillierte Bibliografische Daten sind im Internet über http://dnb.d-nb.de abrufbar.

Herausgeber Forschungszentrum Jülich GmbH

und Vertrieb: Zentralbibliothek, Verlag

52425 Jülich

Tel.: +49 2461 61-5368 Fax: +49 2461 61-6103 zb-publikation@fz-juelich.de

www.fz-juelich.de/zb

Umschlaggestaltung: Grafische Medien, Forschungszentrum Jülich GmbH

Druck: Grafische Medien, Forschungszentrum Jülich GmbH

Copyright: Forschungszentrum Jülich 2018

Schriften des Forschungszentrums Jülich Reihe Energie & Umwelt / Energy & Environment, Band / Volume 439

D 82 (Diss., RWTH Aachen, Univ., 2018)

ISSN 1866-1793 ISBN 978-3-95806-363-1

Vollständig frei verfügbar über das Publikationsportal des Forschungszentrums Jülich (JuSER) unter www.fz-juelich.de/zb/openaccess.



This is an Open Access publication distributed under the terms of the <u>Creative Commons Attribution License 4.0</u>, which permits unrestricted use, distribution, and reproduction in any medium, provided the original work is properly cited.

And finally this question, the mystery of who's story it will be. Of who draws the curtain. Who is it that chooses our steps in the dance? Who drives us mad? Lashes us with whips and crowns us with victory when we survive the impossible? Who is it, that does all of these things? Who honors those we love for the very life we live? Who sends monsters to kill us, and at the same time sings that we will never die? Who teaches us what's real and how to laugh at lies? Who decides why we live and what we'll die to defend? Who chains us? And who holds the key that can set us free... It's You. You have all the weapons you need. Now Fight!

-Sucker Punch

Abstract

Solar energy has the potential to provide clean and sustainable energy to all of humankind and during the past years the amount of operating solar power plants constantly increased. The increasing installation and production volumes call for powerful measuring techniques for the process control of solar cell production lines, but also for the monitoring of modules operating in solar power plants.

Luminescence imaging of solar cells and modules is such a measuring technique. By observing the radiative recombination that is emitted by a solar cell, just like the light emission of LEDs, luminescence imaging provides spatially resolved information about a solar cells electrical and optical properties. Therefore, luminescence imaging has the ability to locate and rate defects and inhomogeneities in solar cells. This thesis focuses on the use of luminescence imaging for quantitative evaluations. Hence, it is not only looked at the ability of luminescence imaging to locate abnormalities in solar cells or modules but also on possibilities to use luminescence imaging as a way to quantify the strength of a defect or to estimate the influence of a defect on the photovoltaic performance of a whole device.

During this work it was made use of two model solar cell technologies. Crystalline silicon solar cells are currently the most successful solar cell technology for which luminescence imaging is already a well established tool. This technology is primarily used in this thesis to test newly developed imaging methods. However, the focus of this thesis lies on the analysis of the so called CIGS solar cells and modules, which belong to the thin-film technologies. Although the market share of the thin-film technologies was only $5\,\%$ of the produced solar cells in 2016 their production volumes are constantly increasing.

To allow for a quantitative evaluation of luminescence images of CIGS solar cells it is first essential to understand the influence of metastable effects in this technology. Metastable effects alter the properties of CIGS solar cells, including the luminescence signal, during the exciation with illumination or the application of bias. An in depth analysis of the metastable effects at different applied currents and temperatures showed that the metastable effects lead in most cases to a reduction of the series resistance and dark recombination current in CIGS solar cells. The changes vary in magnitude for the different conditions and may happen within a matter of seconds. However, a stabilization of the solar cells can only be reached after a constant excitation of several hours. This knowledge is essential for an accurate quantitative evaluation of luminescence images. In this work, an influence of metastable effects on the results were avoided by automation and combining image data only with electrical data measured simultaneously.

In the following a quantitative luminescence method is analyzed in detail that allows to determine the current/junction voltage characteristic of individual cells already connected within a module. The characteristics allow in turn the quantification of defects, like shunts, in the individual cells. The current/junction voltage characteristics obtained by imaging unexpectedly vary depending upon the illumination conditions at which they are measured. The difference is explainable by an error resulting from an averaging procedure of measured local junction voltages. This procedure does not yield an accurate measure for the voltage over a cell.

As a second quantitative evaluation method, the so called photocurrent collection efficiency imaging method is analyzed. The method yields spatially resolved information about the ability of a solar cells to collect photocurrent and was experimentally demonstrated and verified on a crystalline silicon solar cell. The influence of parameters, like series resistances and shunts, on the photocurrent collection efficiency is extensively discussed and demonstrated with the help of simulations. Furthermore, the original method, which only yielded differential information is extended to allow a determination of the total amount of photocurrent collected from a certain area of a solar cell. This total photocurrent collection efficiency is closer related to the actual influence a certain area has on the performance of a solar cell. The new method was also verified experimentally with a crystalline silicon solar cell. On solar modules the photocurrent collection efficiency behaves different to single cells due to the series connection of cells. For example, defected cells may show a larger photocurrent collection efficiency. The effects are demonstrated with CIGS mini-modules and explained using simulations.

At low voltages the photocurrent collection efficiency imaging could not be verified for CIGS solar cells. It is shown that CIGS solar cells exhibit an injection dependent series resistance that increases at low voltages. This injection dependent series resistance could also be reproduced in device simulations and is resulting from the minority charge carrier transport through the CIGS absorber. An equivalent circuit model including an injection dependent series resistance is in the following used to explain the observed deviations in the photocurrent collection efficiency imaging of CIGS solar cells. Finally, it is discussed how this model could also be interesting to describe voltage dependent photocurrent that is often observed in many kinds of new solar cells technologies.

Zusammenfassung

Solarenergie hat das Potenzial, der gesamten Menschheit saubere und nachhaltige Energie zu liefern und in den letzten Jahren hat die Anzahl der betriebenen Solar-Kraftwerke stetig zugenommen. Die steigenden Installations- und Produktionsvolumen erfordern leistungsfähige Messmethoden für die Prozesssteuerung von Solarzellenfertigungslinien, aber auch für die Überwachung von Modulen in Solarkraftwerken.

Die Lumineszenz-Bildgebung von Solarzellen und -modulen ist eine solche Messmethode. Durch die Beobachtung der strahlenden Rekombination, die von einer Solarzelle emittiert wird, wie die Lichtemission von LEDs, liefert die Lumineszenz-Bildgebung räumlich aufgelöste Informationen über die elektrischen und optischen Eigenschaften einer Solarzelle. Lumineszenz-Bildgebung hat daher die Fähigkeit, Defekte und Inhomogenitäten in Solarzellen zu lokalisieren und zu bewerten. Diese Arbeit konzentriert sich auf die Verwendung von Lumineszenz-Bildgebung für quantitative Auswertungen. Daher wird nicht nur die Fähigkeit der Lumineszenz-Bildgebung untersucht Anomalien in Solarzellen oder -modulen zu lokalisieren, sondern auch die Nutzung der Lumineszenz-Bildgebung zur Quantifizierung der Stärke von Defekten bzw. des Einflusses eines Defektes auf die photovoltaische Leistung eines ganzen Bauelements.

In dieser Arbeit wurde auf zwei Modell Solarzellen Technologien zurückgegriffen. Kristalline Silizium-Solarzellen sind derzeit die erfolgreichste Solarzellentechnologie, für die die Lumineszenz-Bildgebung bereits ein etabliertes Werkzeug ist. Diese Technologie wird in dieser Arbeit hauptsächlich zum Testen neu entwickelter Bildgebungsverfahren eingesetzt. Der Schwerpunkt dieser Arbeit liegt jedoch auf der Analyse der sogenannten CIGS-Solarzellen und -module, die zu den Dünnschichttechnologien gehören. Obwohl der Marktanteil der Dünnschichttechnologien 2016 nur 5 % der produzierten Solarzellen betrug, nimmt ihr Produktionsvolumen stetig zu.

Um eine quantitative Auswertung von Lumineszenzbildern von CIGS Solarzellen zu ermöglichen, ist es zunächst notwendig, den Einfluss von metastabilen Effekten in dieser Technologie zu verstehen. Metastabile Effekte verändern die Eigenschaften von CIGS-Solarzellen, einschließlich des Lumineszenzsignals, während der Anregung mit Beleuchtung oder Spannung. Eine eingehende Analyse der metastabilen Effekte bei verschiedenen angelegten Strömen und Temperaturen zeigte, dass die metastabilen Effekte in den meisten Fällen zu einer Reduktion des Serienwiderstandes und des Dunkelrekombinationsstroms in CIGS Solarzellen führen. Die Änderungen variieren in den Größen für die verschiedenen Bedingungen

und können innerhalb von Sekunden erfolgen. Eine Stabilisierung der Solarzellen benötigt jedoch eine konstante Anregung von mehreren Stunden. Dieses Wissen ist essentiell für die quantitativen Auswertung von Lumineszenzbildern. In dieser Arbeit wird der Einfluss von metastabilen Effekten hauptsächlich durch Automatisierung und das Kombinieren von Bilddaten nur mit gleichzeitig gemessenen elektrischen Daten vermieden.

Im Folgenden wird ein quantitatives Lumineszenzverfahren im Detail analysiert, dass es erlaubt, die Strom / Diodenspannungs-Charakteristik einzelner Zellen zu bestimmen, die bereits innerhalb eines Moduls verbunden sind. Diese Charakteristiken erlauben wiederum die Quantifizierung von Defekten, wie Shunts, in den einzelnen Zellen. Unerwarteterweise, variieren die durch die Bildgebung erhaltenen Strom- / Diodenspannungs-Charakteristiken in Abhängigkeit von den Beleuchtungsbedingungen, bei denen sie gemessen werden. Der Unterschied ist durch einen Fehler erklärbar, der sich aus einer Mittelungsprozedur von gemessenen lokalen Diodenspannungen ergibt. Diese Prozedur liefert nicht einen exakten Wert für die Spannung, die über eine Zelle abfällt.

Als eine zweite quantitative Bewertungsmethode wird die sogenannte Photostromsammlungseffizienz Bildgebungsmethode analysiert. Die Methode führt zu räumlich aufgelösten Informationen über die Fähigkeit von Solarzellen, Photostrom zu sammeln und wurde erstmals experimentell an einer kristallinen Silizium-Solarzelle demonstriert und verifiziert. Der Einfluss von Parametern, wie Serienwiderständen und Shunts, auf die Photostromsammlungseffizienz wird ausführlich diskutiert und anhand von Simulationen demonstriert. Darüber hinaus wurde das ursprüngliche Verfahren, das nur differentielle Information lieferte, erweitert, um eine Bestimmung der Gesamtmenge an Photostrom zu ermöglichen, die von einem bestimmten Bereich einer Solarzelle gesammelt wird. Diese gesamte Photostromsammlungseffizienz ist relevanter für den tatsächlichen Einfluss eines bestimmten Bereichs auf die Leistung einer Solarzelle. Die neue Methode wurde auch experimentell mit einer kristallinen Silizium-Solarzelle verifiziert. Bei Solarmodulen verhält sich die Photostromsammlungseffizienz aufgrund der Reihenschaltung von Zellen anders als bei einzelnen Zellen. Zum Beispiel können defekte Zellen eine größere Photostromsammlungseffizienz zeigen. Die Effekte werden mit CIGS-Minimodulen demonstriert und mit Hilfe von Simulationen erläutert.

Bei niedrigen Spannungen konnte die Photostromsammlungseffizienz-Bildgebung für CIGS-Solarzellen nicht verifiziert werden. Es wird gezeigt, dass die CIGS Solarzellen einen injektionsabhängigen Serienwiderstand aufweisen, der bei niedrigen Spannungen ansteigt. Dieser injektionsabhängige Serienwiderstand konnte auch in einer Bauelement Simulation reproduziert werden und resultiert aus dem Transport der Minoritätsladungsträger durch den CIGS-Absorber. Ein Ersatzschaltungsmodell mit einem injektionsabhängigen Serienwiderstand wird im folgendem verwendet, um die beobachteten Abweichungen bei der Photostromsammlungseffizienz-Bildgebung von CIGS-Solarzellen zu erklären. Abschließend wird gezeigt, dass dieses Modell auch interessant sein könnte, um spannungsabhängigen

Photostrom zu beschreiben, der oft in vielen neuen Solarzellen-Technologien beobachtet wird.

Contents

1.	Intro	oduction	13			
2.	Fundamentals					
	2.1.	Physics of Semiconductor Solar Cells	17			
		2.1.1. Charge Carrier Densities in Semiconductors	17			
		2.1.2. pn-Junctions	18			
		2.1.3. Recombination	20			
		2.1.4. Generation and Collection	22			
	2.2.	Equivalent Circuits and the Photovoltaic Parameters	23			
		CIGS Solar Cells	27			
	_	2.3.1. Structure	27			
		2.3.2. Metastabilities	29			
	2.4.	Luminescence of Solar Cells	32			
		2.4.1. Physics	32			
		2.4.2. Imaging Methods	33			
3.	Ехр	erimental Methods and Simulations	37			
	-	Experiments	37			
		3.1.1. Current/Voltage Characterization	37			
		3.1.2. Short Circuit Current/Open Circuit Voltage Characterization	38			
		3.1.3. Luminescence Imaging	39			
		3.1.4. Sample Overview	43			
	3.2.	Simulations	47			
		3.2.1. SCAPS	47			
		3.2.2. PVMOS	48			
4.	Exp	eriments in the Presence of Metastabilities	53			
	4.1.	Experimental Procedure and Results	53			
	4.2.	Simulations and Discussion	60			
	4.3.	Conclusion	62			
5.	Rec	onstruction of Current/Voltage Characteristics of Cells in Modules	65			
	5.1.	• -	65			
	5.2.	Simulations and Discussion	72			
	5.3	Conclusion	78			

6.	Pho	tocurrent Collection Efficiency Imaging	81		
	6.1.	Theory	81		
		6.1.1. The Differential Photocurrent Collection Efficiency \dots	81		
		6.1.2. The Total Photocurrent Collection Efficiency	88		
		6.1.3. From Collected Photocurrent to Collected Power and Net			
		Power	89		
	6.2.	Crystalline Silicon Solar Cells	91		
		6.2.1. Experimental Results	91		
		6.2.2. Simulation and Discussion	97		
	6.3.	Solar Modules	106		
		6.3.1. Experimental Results	107		
		6.3.2. Simulations and Discussion	109		
	6.4.	CIGS Solar Cells	119		
		6.4.1. Experimental Results	119		
		6.4.2. Simulations and Discussion	126		
	6.5.	Conclusion	128		
7.	Inje	ction Dependent Series Resistance in CIGS	131		
	7.1.	Theory	131		
	7.2.	Experimental Results	133		
	7.3.	SCAPS Modelling	134		
	7.4.	Equivalent Circuit Model	140		
	7.5.	Conclusion	149		
8.	Con	clusion and Outlook	151		
Α.	Арр	endix - Chapter 6	155		
		·			
В.	Арр	endix - Chapter 7	157		
Bil	bliog	raphy	157		
Lis	t of	Abbreviations	171		
Lis	ist of Publications				
_					
Cu	irricu	lum Vitae	179		
Αc	know	vledgment	181		

1. Introduction

Life is unfair. The quality of life of any human being in the world is to some extend determined by luck. Whether it is the possibility to eat whenever and whatever they like, to be with the persons they love or to do the sports they like best. Of course everybody can try to achieve his goals by sheer hard work, but even if we do not consider that the chances of success still depend a lot of where and when you are born, illness or accident can strike everybody without exception. Inequality, also in life quality will be existing between humans as long as humans exists, because each human is different. However, what should be striven for and what can be reached is an equality of chances to a good life. Every human being should have the same chances to reach their life goals and find their happiness and every other human being should support that, or at least not worsen the chances of another to find happiness.

This simple approach to life becomes awfully complicated when globalization comes into play. Today, every action a person takes influences the life of people all around the world. Be it the purchase of a new T-shirt, which was made on another continent, or the driving of a car to work. If the consequences of each action for other humans are positive or negative is difficult to estimate.

In contrast, the consequences of burning fossil fuels are well known to cause global warming. Global warming leads to the suffering of humans through more extreme weather conditions, loss of harvests and the rise of the sea level [1–3]. Thus, everybody who burns fossil fuel is in fact increasing his own life quality by harming others. That people still burn fossil fuels even after fully understanding the consequences, is due to the selfishness deeply linked within the human nature. However, another part of human nature is also empathy. And empathy allows humans to overcome their own selfishness. Empathy drives humans to look for other renewable energy sources that can act as substitutions for the burning of fossil fuels, so that the unfairness in life resulting from the use of fossil fuels may be reduced.

Solar cells convert the solar irradiation into electrical energy. As the energy from solar irradiation exceeds the energy demand by far, photovoltaic technologies are expected to play a vital role in satisfying the energy demand with renewable sources. Due to improvements in efficiency and reduction in productions costs, the costs for energy produced by solar power plants has decreased during 2005 to 2015 by about 80 %, making it competitive with new combined cycle gas turbines, coal and nuclear power plants [4, 5]. Consequently, the amount of installed solar cells massively increased. In 2016 76.6 GW were installed increasing the worldwide

installed capacity to 306.5 GW.

The major technology of solar cells used are so called crystalline silicon solar cell, which made up 95 % of the produced solar cells in 2016. The other 5 % is made up from so called thin-film solar cells. Although the market share is less, thin-film solar cells remain important as they promise less production costs and niche applications for example for building integrated solutions. The efficiency of thin-film solar cells is at the moment lower than crystalline silicon technologies, but still the amount of annually produced $Cu(In,Ga)Se_2$ (CIGS) and CdTe solar cells (which belong to the thin-film technologies) steadily increased during the last three years [6].

Solar power plants fundamentally differ from power plants using fossil resources as the fuel powering solar power plants (the solar irradiation) is free. The operating and maintenance costs are low and the costs of producing electrical energy using solar cells are dominated by the initial investment costs. Therefore, the cost of capital has a major influence on the total costs of solar energy [4]. Solar power plants are long term investments that need to provide energy for 25 to 30 years to be profitable. Thus, reliability is an important property of solar power plants. Improved reliability reduces the risk a potential investor takes and therefore also reduces the premium he wants, which will consequently reduce the cost of capital. To sustain the reliability of a solar power plant constant monitoring is needed, which employ methods that can locate defects fast and suggest possible solutions to problems.

Luminescence and thermography imaging methods are powerful monitoring techniques as they not only show if a problem is present (which simple monitoring of the power output also does), but also where the problem is located [7–9]. Additionally, more sophisticated methods could have the potential to also estimated the severeness of a problem for the overall power output, which is especially important if several defects are detected [10, 11]. Thermography detects heat sources within solar plants, which indicate defects like shortages or unusual high resistances [12, 13]. In contrast to that luminescence imaging observes the radiative recombination in solar cells [14]. Radiative recombination is the only loss mechanism within a solar cell, which cannot be avoided. Thus, a large amount of radiative recombination means a lower amount of avoidable loss mechanism and therefore luminescence images are usually bright in regions where the solar cells and modules are working well.

The luminescence signal is related via the reciprocity relation to many physical properties of the solar cell, like the absorption and light trapping properties as well as defect states and the quasi Fermi-level splitting [15–20]. The quasi Fermi-level splitting can be interpreted as a voltage within an equivalent circuit. The approach to use the luminescence signal to obtain information about local voltages within a solar cell led to the development of several imaging methods, which allow the determination of further local properties like the local series resistance [21–25]. These imaging methods are not only valuable for plant monitoring but may also

reduces losses in the production of solar cells and provide crucial information during the research and development process of solar cells.

Most imaging methods were developed for the analysis of silicon solar cells. This work focuses on application of luminescence imaging techniques on CIGS solar cells, which are currently the thin-film technology offering the highest power conversion efficiency [26]. Although, the fundamental principles of the power conversion efficiency in thin-film and crystalline silicon solar cells are the same and additionally the reciprocity relation was already found to be also applicable to CIGS solar cells [27], imaging techniques developed for crystalline silicon solar cells do not necessarily work for CIGS solar cells [28]. The underlying equivalent circuit networks assumed for crystalline silicon solar cells and modules may differ, e.g. due to the larger role shunts play in thin-film solar cells and also non-ohmic transport processes.

In this context, a larger portion of this work will be about the imaging of the photocurrent collection efficiency, which is a method recently developed [29, 30]. The photocurrent collection efficiency describes the portion of locally generated photocurrent that can contribute to the solar cells current output. Therefore, this quantity shows the losses resulting from high series resistance and shunts. The method is applied to CIGS and crystalline silicon solar cells and modules to find possible differences. The method is additionally further developed to provide spatially resolved information about the power a solar cell or module may generate.

In the following an outline of the thesis is given. Chapter 2 describes the fundamentals of solar cells and how they are in general electrically characterized. Additionally, the special properties of CIGS solar cells including metastabilities will be discussed and an overview over the physics and assumptions underlying luminescence imaging techniques are provided. Chapter 3 introduces the experimental and simulation methods used in this work and also presents an overview of the samples used. In Chapter 4 a special look is taken at the role metastabilities play for CIGS imaging. It will be shown how a CIGS samples may alter during measurements and how it is avoided that these changes influence the tested luminescence imaging methods. Chapter 5 shows the results of an imaging technique that reconstructs the current/voltage characteristics of CIGS solar cells that are connected in series to form a module. A recently proposed method is extended to measurements under illumination and the found differences are discussed. A close look at the photocurrent collection efficiency imaging technique is performed in Chapter 6. The method is experimentally demonstrated on CIGS and crystalline silicon solar cells. The applicability of the method to solar modules is discussed and also demonstrated. Furthermore, the method was extended to provide information not only about the differential, but also total amount of current that is collected by a certain region. Finally, in Chapter 7 some special imaging results found for CIGS samples in the preceding two chapters are discussed and a model is proposed which explains the effects using an injection dependent series resistance.

2. Fundamentals

This chapter will introduce most of the fundamental knowledge that is needed for understanding this thesis. It begins with an introduction into the physics of semiconductor solar cells and how they convert solar energy into electrical energy. The information that can be obtained from electrical measurements of solar cells is discussed in the context of equivalent circuit models, which describe solar cells in a simplified way. Furthermore, a detailed look will be taken at the structure and properties of CIGS solar cells as this technology was in the focus of this thesis. Afterwards, the theory behind luminescence measurements is discussed. It will be described what information are obtainable from the observation of the luminescence of solar cells. Finally a choice of imaging methods are presented and their underlying assumptions discussed.

2.1. Physics of Semiconductor Solar Cells

2.1.1. Charge Carrier Densities in Semiconductors

Semiconductor solar cells are the solar cells having the largest photovoltaic conversion efficiency [26]. Although the materials from which semiconductor solar cells can be made are quite different the underlying process of the conversion of light into electrical energy is always similar. Semiconductors are materials, with a valence and a conduction band seperated by a small energy gap of the size $E_{\rm g}({\rm called\ bandgap})$ in which no electrons may exist. In contrast, in insulators the bandgap is large, while metals have no gap at all. Additionally, in a thermal equilibrium (meaning a state at fixed temperature without any illumination of the semiconductor) nearly no electrons exist that have an energy above the bandgap and the states below the bandgap are nearly completely filled with electrons.

The density of electrons $n_{\rm e}$ in the conduction band and the density of holes $n_{\rm h}$ in the valence band can be derived using an integral over the energy of the density of states and the Fermi-Dirac distribution, which describes the occupation probability of the states. The equations for $n_{\rm e,h}$ in the Boltzmann approximation read

$$n_{\rm e} = N_{\rm c} \exp\left(\frac{E_{\rm fn} - E_{\rm c}}{kT}\right) \tag{2.1a}$$

$$n_{\rm h} = N_{\rm v} \exp\left(\frac{E_{\rm v} - E_{\rm fh}}{kT}\right). \tag{2.1b}$$

Here, k is the Boltzmann constant, T is the Temperature, $N_{\rm c}$ and $N_{\rm v}$ are the effective density of states at the energies of the edges of the conduction band $E_{\rm c}$ or valence band $E_{\rm v}$, respectively, and $E_{\rm fn}$ and $E_{\rm fh}$ are the positions of the electron and hole quasi-Fermi levels, which are in equilibrium equal (to the Fermi-level).

In a so called intrinsic semiconductor without any doping all the electrons in the conduction band need to originate from the valence band and it follows $n_{\rm e} = n_{\rm h} = n_{\rm i}$, which is the so called intrinsic charge carrier density. However, solar cells usually make use of doping, which means that defect states are (intentionally or non-intentionally) implemented. When these defects have more or less electrons that are required for a stable chemical bonding they can emit electrons or holes into the conduction or valence band. If a defect can emit an electron it is called a donor, and when it can emit holes it is called an acceptor. With doping it is possible that $n_{\rm e}$ and $n_{\rm h}$ may vary by a large amount. If $n_{\rm e}$ is larger than $n_{\rm h}$ we speak of an n-typed doped semiconductor and vice versa we speak of a p-typed doped semiconductor. Accordingly, the Fermi-level in equilibrium shifts in an n-type layer closer to the conduction band and vice versa (Figure 2.1).

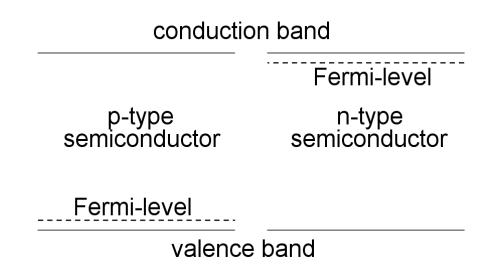


Figure 2.1.: Sketch of the position of the Fermi-level within the band gap of an n- or p-type semiconductor.

2.1.2. pn-Junctions

For a semiconductor solar cell, usually an n-typed material is in contact with a p-typed material that form together a so called pn-junction. In contact the Fermi-levels of the two materials need to align, which results in a band bending of the conduction and valence bands (Figure 2.2). Due to the difference in the electron/hole densities of the two materials, electrons/holes diffuse from the n/p-type material to the p/n-typed material. Thus, negative charges accumulated in the p-type region and vice versa. This results in an electric field between the n- and p-type layers, and thus to drift current. The electric field grows until the drift current resulting from it counteracts the diffusion current resulting from the unequal electron/hole densities, so that in a thermal equilibrium no net current flows.

The region of the electric field is called space charge region (SCR) and within

this field no free charge carriers may exists as they are getting pulled to one of either side. If a negative bias is induced in the n-type region the electric field is reduced and the diffusion current will flow again, so that current will flow through the pn-junction. However, if a negative bias is applied at the p-type layer the electric field between the two layers is increased. As no free charge carriers are existing in the SCR almost no net current will flow [31]. That a pn-junction only allows current flow in only one direction is one of their basic properties. Devices that have this property are commonly known as diodes.

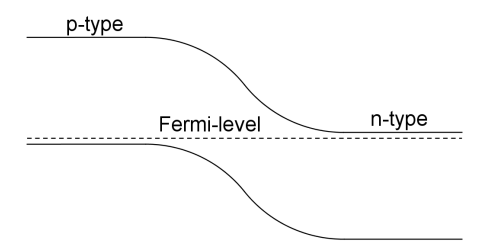


Figure 2.2.: Sketch of the shifting of the conduction and valence band edges, to allow an alignment of the Fermi-levels when a n- and p-type semiconductor are brought together.

In the following the foundations to understanding the current flow through a solar cell, made from a simple pn-junction, are introduced. The charge transport through a semiconductor can be described with the Poisson equation (Equation 2.2a), describing the dependence of the electrostatic potential Ψ on the local space charge density ρ , and the continuity equation describing rate of change of the charge carrier densities (Equations 2.2b and 2.2c)

$$\frac{\mathrm{d}^2 \Psi}{\mathrm{d}z^2} = -\frac{\mathrm{d}E_{\text{field}}}{\mathrm{d}z} = -\frac{\rho}{\epsilon_0 \epsilon_r} \tag{2.2a}$$

$$\frac{\mathrm{d}n_{\mathrm{e}}}{\mathrm{d}t} = \frac{1}{e} \frac{\mathrm{d}J_{\mathrm{e}}}{\mathrm{d}z} + G - R \tag{2.2b}$$

$$\frac{\mathrm{d}n_{\rm h}}{\mathrm{d}t} = -\frac{1}{e}\frac{\mathrm{d}J_{\rm h}}{\mathrm{d}z} + G - R. \tag{2.2c}$$

Here, $\epsilon_0 \epsilon_r$ is the dielectric constant of the semiconductor and G and R are the generation rate and recombination rate, respectively. The quantity z describes the position (e.g. the depth of the semiconductor layer), e is the elementary charge and $E_{\rm field}$ is the electric field. The quantities $J_{\rm e/h}$ describe the electron/hole current density in the conduction or valence bands, which depend on the charge carrier densities, mobilities $\mu_{\rm e/h}$ and quasi-Fermi level gradients in the respective bands

$$J_{\rm e} = \mu_{\rm e} n_{\rm e} \frac{\mathrm{d}E_{\rm fn}}{\mathrm{d}z} \tag{2.3a}$$

$$J_{\rm h} = \mu_{\rm h} n_{\rm h} \frac{\mathrm{d}E_{\rm fp}}{\mathrm{d}z}.$$
 (2.3b)

Simplifying, we assume that the current through the pn-junction is carried mostly by the majority carriers, meaning the current flows through the valence band in the p-region and through the conduction band in the n-region. This leads to the lowest voltage loss, as the quasi-Fermi level gradient is lowest when the charge carrier density is highest. The gradient is usually so low that we neglect it in the following derivation, although the voltage loss due to the carrier transport may play a role (cf. Chapter 7). For now, holes and electrons flow through the region where they are majorities towards the space charge region. To keep the current flowing, recombination of the holes and electrons has to take place. The recombination processes are usually what limits the current through a pn-junction especially at lower applied voltages.

2.1.3. Recombination

Two processes will be discussed that describe the possibility of an electron in the conduction band to recombine with a hole in the valence band. The first process is radiative recombination. This term means that the electron emits the energy it contained, due to its elevated state, as a photon while it moves to a state of lower energy in the conduction band [32]. The rate of the process depends on the densities of electrons and holes and is given by

$$R_{\rm rad} = B n_{\rm e} n_{\rm h}, \tag{2.4}$$

where B is the radiative recombination constant. With the equations for $n_{\rm e}$ and $n_{\rm h}$ (Equations 2.1a and 2.1b) it follows that the radiative recombination is proportional to the exponential of the difference in the quasi-Fermi-levels

$$R_{\rm rad} \propto \exp\left(\frac{-E_{\rm g}}{kT}\right) \exp\left(\frac{E_{\rm fn} - E_{\rm fp}}{kT}\right).$$
 (2.5)

Note, that $R_{\rm rad}$ contains in that form also the radiative recombination happening in the thermal equilibrium, due an excitation of electrons into the conduction band, when the temperature is not zero. To obtain the net recombination due to an applied voltage, the recombination happening at thermal equilibrium, which is given by the equilibrium charge carrier densities $n_{\rm e,0}$ and $n_{\rm h,0}$, needs to be subtracted. If we assume that the applied voltage is completely transferred to the quasi-Fermi level splitting in the region where recombination takes place (no additional voltage losses due to transport resistance) we see that the recombination,

and therefore the current through the pn-junction depends exponentially on the applied voltage.

However, usually in solar cells radiative recombination is not the dominating cause of recombination. A second important recombination process is the so called Shockley-Read-Hall (SRH) recombination [33]. It describes the recombination that takes place via defect states that exists within the bandgap. These defects states may catch an electron or hole from the conduction or valence band and when it catches both they recombine. The energy lost during such a process is turned into heat via an interaction with phonons. A simplified equation describing the SRH recombination $R_{\rm SRH}$ via a defect in the middle of the bandgap reads

$$R_{\rm SRH} = \frac{n_{\rm e}n_{\rm h} - n_{\rm e,0}n_{\rm h,0}}{(n_{\rm e} + n_{\rm h})\tau}.$$
 (2.6)

Where τ describes the lifetime of the electrons/holes which is assumed to be equal in the present case. Usually the lifetime is different for electrons and holes and depends on the position of the defect states in the bandgap. We can easily derive that the recombination rate is roughly proportional to the minority carrier density, or the intrinsic charge carrier density when $n_{\rm e}$ and $n_{\rm h}$ are equal. Thus, the voltage dependence of the recombination current depends on the rate of change of these charge carrier densities on the applied voltage. In a p-type layer the quasi-Fermi levels of the holes is fixed and any voltage will only shift the quasi-Fermi level of the electrons. Therefore, the minority carrier density depends exponentially on the applied voltage. The same goes for n-type layer where only the hole quasi-Fermi level gets shifted. However, if n_e and n_h are the same (e.g. in the space charge region) an applied voltage will move the quasi-Fermi levels of the electrons and holes, meaning that the quasi-Fermi level of the electrons is only shifted by half of the amount of the applied voltage. This adds an additional factor of two in the exponential dependence of the recombination current on the voltage. This additional factor is called ideality factor $n_{\rm id}$. In reality it may vary due to the position of the defects in the bandgap and due to the applied voltage as recombination positions may change.

We obtain the following equation describing the current through a pn-junction due to an applied voltage

$$J = J_0 \left[\exp\left(\frac{eV}{n_{\rm id}kT}\right) - 1 \right]. \tag{2.7}$$

The quantity J_0 is called the dark saturation current, describing the recombination happening in the thermal equilibrium. It is important to note, that J_0 depends also on the temperature and increases with rising temperature (cf. Equation 2.5). Therefore, the current through a pn-junction increases with rising temperature and constant applied voltage.

2.1.4. Generation and Collection

According to the Equations 2.2b and 2.2c the local charge carrier densities also depend on the generation of charge carriers. Generation describes the process of absorbing the energy of a photon to lift an electron from the valence band to the conduction band. As this process happens in one step, the used photon needs to have at least the energy equal to the bandgap. How much light can be absorbed at which wavelength is described with the absorbtion constant. Of course the amount of absorbed light and generated charge carriers also depends on other optical properties of the device, like the reflection at the surface, the thickness, the reflection at the back of an absorber or other light trapping properties.

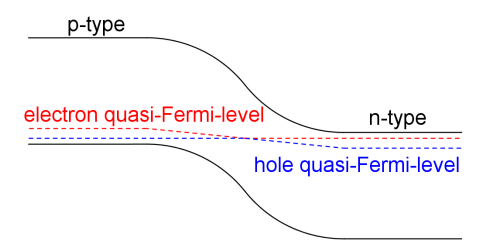


Figure 2.3.: Sketch that shows the splitting of the quasi-Fermi levels due to an illumination of a pn-junction. It is visible that the position of the quasi-Fermi levels changes from the n- to p-layer.

However, the absorption of light and the creation of charge carriers are not sufficient for a solar cell to work as a power source. The generated charge carrier also need to be collected to provide a current. The charge carrier collection is achieved by the pn-junction. The process is in the following described in simplified terms. From Equations 2.3a and 2.3b it is known that a current is driven by a gradient in the electrochemical potential (quasi-Fermi levels) of charge carriers. In a pn-junction illumination creates such a gradient in the quasi-Fermi level. The illumination generates electrons and holes in the p-region. Due to the larger amount of holes in the p-region, such an increase of charge carriers shifts in principle only the quasi-Fermi level of the electrons and does not influence the quasi-Fermi level of the holes. In the n-type region however the quasi-Fermi level of the electrons stays mostly fixed even when additional electrons and holes are generated. Thus, due to the absorption of light, the electron quasi-Fermi level in the p-type region shifts above the electron quasi-Fermi level in the n-type region (Figure 2.3). This differences drives in the following an electron current from the p-type region to the n-type region. How much of the generated charge carriers can be actually collected by solar cell depends on the charge carrier collection efficiency, which depends on properties like the diffusion constant or the distance of the position at which the charge carrier are generated to the pn-junction.

Usually it is assumed that the amount of collected charge carriers, e.g. the current that flows due to the illumination of the solar cell is superimposed with the current that flows through a solar cell due to an applied voltage. As this photocurrent $J_{\rm ph}$ is flowing in the opposite direction of the recombination current (cf. Equation 2.7), the photocurrent is substracted from the recombination current to obtain the net current flow under illumination and applied bias.

2.2. Equivalent Circuits and the Photovoltaic Parameters

So far the current through a solar cell due an applied voltage was derived and it was explained that under illumination the current is superimposed with a constant photocurrent. In a realistic solar cell, in general two more aspects are important for its current density/voltage (J/V) characteristic describing the dependence of the current on the voltage. That is the series resistance $R_{\rm s}$ and the shunt resistance $R_{\rm p}$. A series resistance is a resistance connected in series to the pn-junction and describes any ohmic resistance that results for example from the contacting of the solar cell. A shunt resistance describes the fact that any current might also bypass the pn-junction for example due to defects in the solar cell. Including these two resistances into a model of the solar cell yields the equivalent circuit seen in Figure 2.4. The pn-junction is represented by a diode, a current source represents the generated photocurrent, and ohmic resistances represent the shunt and series resistances.

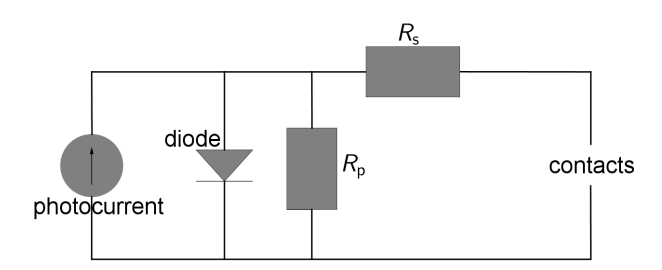


Figure 2.4.: One-diode equivalent circuit model that consists of a diode modeling the pn-junction, a current source modeling the generated photocurrent, a shunt resistance, and a series resistance.

The current through the one-diode equivalent circuit is given by the following equation [34]

$$J = J_0 \left[\exp\left(\frac{eV - JR_s}{n_{\rm id}kT}\right) - 1 \right] + \frac{V - JR_s}{R_p} - J_{\rm ph}. \tag{2.8}$$

The equation cannot be solved analytically for J but is solvable numerically. An example for a J/V characteristic is given in Figure 2.5. Note that in the representation used in this work a negative current at a positive voltage means that the solar cell is providing power. The power output is calculated via multiplying current and voltage of the characteristics. The maximum power point MPP shows the point at which the power output P of the solar cell is at its maximum $(P_{\text{MPP}} = J_{\text{MPP}} V_{\text{MPP}})$. The efficiency η of a solar cell is calculated by dividing its maximum power output by the power of the illumination, impacting the area of the solar cell. Other important values of the solar cell J/V characteristic are the open circuit voltage $V_{\rm oc}$, which describes the voltage of the solar cell when it is at open circuit, i.e. the current is zero, and the short circuit current density $J_{\rm sc}$, which describes the absolute value of the measured current, when the solar cell operates at zero voltage, divided by the solar cell area. Usually $J_{\rm sc}$ is equal to the generated photocurrent $J_{\rm ph}$, but it might differ when the series resistance is very large. Another parameter used to described the form of a J/V characteristic is the so called fill factor FF. It is calculated by dividing the maximum power output of the solar cell by the product of $V_{\rm oc}$ and $J_{\rm sc}$

$$FF = \frac{V_{\text{MPP}}J_{\text{MPP}}}{V_{\text{collec}}}.$$
 (2.9)

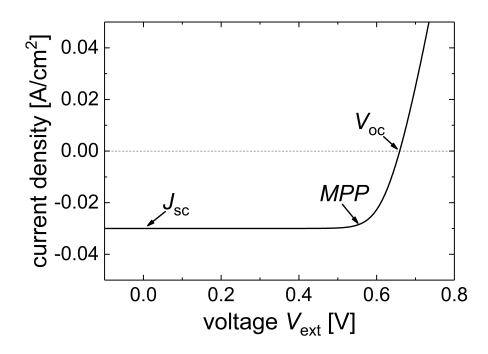


Figure 2.5.: Example for a current voltage characteristic of an equivalent circuit of a solar cell.

As mentioned the equivalent circuit is not analytically solvable for the current J and therefore the different influences of the various parameters on the J/V characteristic is not clear to see. To demonstrate the various effects of the parameters the equivalent circuit was solved numerically with changing parameters (see Figure 2.6). An increase of the series resistance mainly reduces the power output of a solar cell by reducing its fill factor (Figure 2.6 (a)). The size of a series resistance can be estimated by observing the gradient of the J/V characteristic at large voltages. The open circuit voltage is not affected by the series

resistance, as at $V_{\rm oc}$ no current flows through the series resistance. In contrast to that, changes in J_0 influence mainly the open circuit voltage (Figure 2.6 (b)). An increase of the short circuit current shifts the J/V characteristics down (Figure 2.6 (c)). However, note that the down shift decreases towards larger voltages. The reason for that is the series resistance, as the voltage loss across it depends on the current flow across it and therefore also on the short circuit current. Thus, the superposition principle is already violated when only a simple series resistance exists in the solar cell. However, as small series resistances are unavoidable, a violation of the superposition principle usually means that the violated happens already at lower voltages, where a normal ohmic series resistance should not have any influence [35]. A decrease of the shunt resistance results similar to the series resistance also in a decrease of the fill factor, but it may also influence the open circuit voltage (Figure 2.6 (d)). The strength of a shunt is usually estimated by the gradient of the J/V characteristic around zero volts.

In Section 2.1.3 it was mentioned that the recombination processes may either have an ideality factor of one or two. This is implemented into the so called two-diode model which expands the one diode model by an additional diode that is connected in parallel to the original diode [34]. The current through the two diodes in the circuit is still given by Equation 2.7 but one diode has a $n_{\rm id}$ of one and the other of two and the respective dark saturation currents of the two diodes $J_{0.1}$ and $J_{0.2}$ may be different.

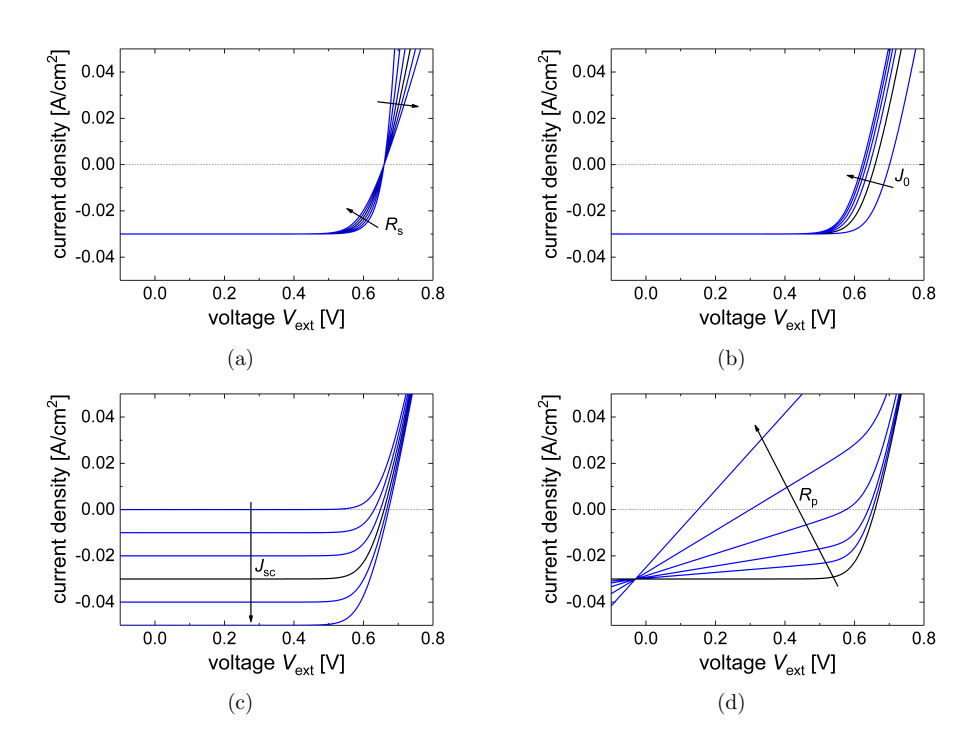


Figure 2.6.: Influence of various parameters on the current voltage characteristics of a solar cells. The arrows show in the direction of increasing parameters (a) $R_{\rm s}=0.1-1.6\,\Omega{\rm cm^2}$ in $0.3\,\Omega{\rm cm^2}$ steps. (b) $J_0=0.5-10.5\times10^{-13}\,{\rm A/cm^2}$ in $2\times10^{-13}\,{\rm A/cm^2}$ steps. (c) $J_{\rm sc}=0-0.05\,{\rm A/cm^2}$ in $0.05\,{\rm A/cm^2}$ steps. (d) $R_{\rm p}=5,10,20,40,80,10^{10}\,\Omega{\rm cm^2}$. Baseline shown in black. Parameters: $R_{\rm s}=1\,\Omega{\rm cm^2}$, $J_0=2.5\times10^{-13}\,{\rm A/cm^2}$, $J_{\rm sc}=0.03\,{\rm A/cm^2}$, $R_{\rm p}=10^{10}\,\Omega{\rm cm^2}$

2.3. CIGS Solar Cells

2.3.1. Structure

So called CIGS solar cells are thin film solar cells where the absorber is made from Cu(In,Ga)(S,Se)₂ (CIGS), which is a I-III-VI semiconductor and belongs to the group of chalcogenide compounds. Together with a buffer layer, which is in this work CdS, and a window layer (here ZnO) a pn-junction is formed. As the materials have different bandgaps the structure is called heterostructure. The structure is sketched in Figure 2.7. The back contact is made from molybdenum sputtered on soda lime glass. The absorber layer can be either deposited on the back contact via co-evaporation (used for the samples produced by Manz, cf. Section 3.1.4) or via a deposition reaction (use for the samples produced by Bosch, cf. Section 3.1.4). During co-evapoaration the formation of the CIGS takes place directly out of the gas phase. For a deposition reaction first a precursor layer is deposited that is afterwards transformed into the final semiconductor film via annealing or a chemical reaction [36].

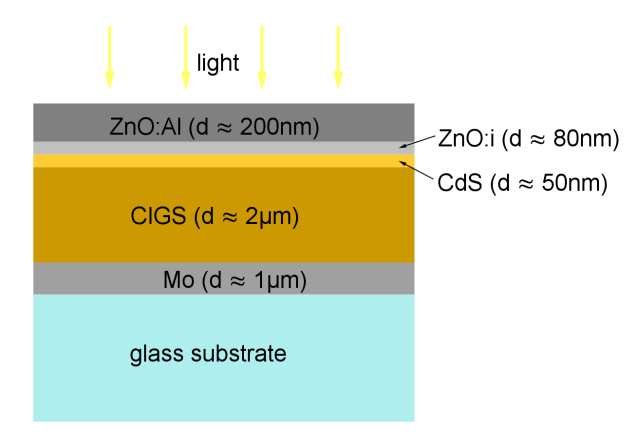


Figure 2.7.: Structure of a typical CIGS solar cell.

An advantage of CIGS solar cells is that by varying the stoichiometry of the material (e.g. the relation of the amount of In to the amount of In+Ga) the bandgap of the material can be adjusted [37]. Thus, the bands within the absorber layer can be changed to maximizes the absorption of sun light and additionally can be graded via adjusting the stoichiometry of the material during the depositions process. Bandgap grading may lead to a better collection of absorbed charge carriers and reduces recombination losses at surfaces [38]. Together with improved film formation properties and adjustment of the composition properties during depositions, bandgap grading leads to better solar cells, which was shown with the so called three-stage process [39].

For the cells analyzed in this work CdS was deposited onto the CIGS absorber via chemical bath deposition. The CdS serves as a so called buffer layer, which stabilizes the underlying CIGS layer and passivates its surface [40, 41]. Above the CdS buffer layer the so called window layer is deposited. It consists of two transparent conductive oxide (TCO) layers, intrinsic and Aluminum doped ZnO which are radio frequency and DC magnetron sputtered onto the CdS layer. The intrinsic ZnO: i brings a larger resistance into the stack. However, it was found to protect the absorber layer from ZnO:Al sputtering damage and also hinders the dopant from the ZnO:Al from diffusing into the absorber layer [42, 43]. Furthermore, the combination of CdS and ZnO:i mitigates the formation of shunts, which is especially important to improve reproducibility for large area production [44]. The function of the ZnO:Al is to act as a front contact that allows the collected charge carriers to move to the terminals of the device, while allowing at the same time light to enter the solar cell. It has to be as transparent and conductive as possible. Still, after optimization the front contact sheet resistance is about 50 times larger than the molybdenum back contact resistance.

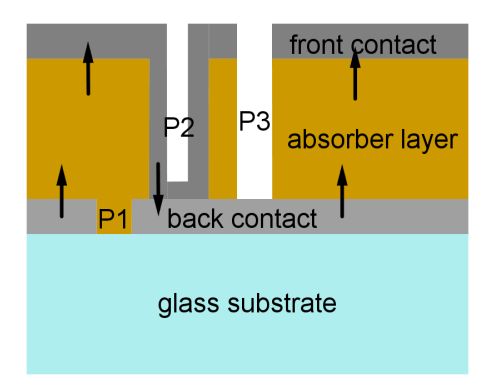


Figure 2.8.: Structure of a the monolithic interconnection used to divide thin film layers into series connected solar cells. The arrows indicate the current flow.

To reduce the power loss from series resistance, solar cells are usually connected in series to form a solar module. This reduces the total current flow and therefore the power loss, which scales quadratic with the current across any resistance. Thin-film layers have the advantage that they can be produced on a large area, which introduces the possibility to define solar cells and interconnect them all on one substrate. For that a so called monolithic interconnection technique is used. A scheme of the connection layout is seen in Figure 2.8. It is achieved by scribing lines into the films after different depositions steps. The first scribing line is the P1 line which separates the back contact. After the absorber and buffer deposition the P2 line separates these layers without harming the back contact. Finally, when the window layer was deposited the P3 line is used to separate the absorber layer

and front contact of cells connected in series. The scribing may be achieved via physical scratching or laser ablation [45, 46].

2.3.2. Metastabilities

In this section an introduction to the metastable effects that occur within CIGS solar cells is given with a short literature overview. The term 'metastabilities' is used for states of a sample that are inherently unstable, meaning a change between the different states is possible during the normal working cycle of a solar cell. The states exists at different energies but are separated by a barrier. Exciting the solar cell with illumination or biasing may move the sample into its energetically higher state. That the state is metastable means that the thermal energy at room temperature may be enough to move the sample across the energy barrier back to its original state of lower energy with time.

The metastable effects reported most often for CIGS solar cells describe an increase of their performance with illumination and/or biasing. This is an advantage compared to the metastable effects found for amorphous thin-film silicon solar cells, which degrade the solar cell due to illumination [47]. The first metastable effects in CIS solar cells were reported by Ruberto and Rothwarf in 1987 [48]. They describe an increase of the open circuit voltage due to illumination of the solar cell. The effect was explained by the tunneling of electrons, trapped in deep defects in the CdS near the interface, into the CIS valence band, where they may recombine with holes if they are sufficiently present (under illumination or forward bias conditions). This would create holes trapped in the CdS that act as a barrier for interface recombination. The reduction of the interface recombination then leads to an increase of the open circuit voltage. However, usually newer CIGS cells are not limited by interface recombination [49]. The metastable effects due to illumination and forward bias were further analyzed by other research groups [50, 51]. It was found that the metastable effects resulting from illumination and biasing are at least in part related, as metastable changes due to illumination could be reduced by biasing the sample before the measurement. In [52] a so-called amphoteric defect that describes a defect, which may exist at different charge states, was held responsible for metastable effects. Such an amphoteric defect may move from being an electron defect to a hole defect by capturing two electrons. The change would be accompanied by large lattice relaxation, which is a slow process and would describe the observed time constant. The idea was developed as it was found that the concentration of hole defects increases while the electron defect concentration decreases.

Additionally, it was observed that CIGS thin films show an increase of the conductivity due to illumination, which is consistent with the observed increased concentration of hole defects [53]. To observe an increase of the conductivity by a factor of two, illumination intensities as low as $2 \,\mathrm{mW/cm^2}$ were sufficient and the larger conductivity persisted for several hours. Thus, the effect was called

persistent photo conductivity (PPC). A model was developed that holds the same defect, which is responsible for the increase of the conductivity, also responsible for the metastable effect inducing an increase of the $V_{\rm oc}$. A larger amount of hole defects reduces the size of the SCR in the CIGS. As the recombination within the SCR was found to be dominant a decrease of the size of the SCR would automatically result in a decrease of overall non-radiative recombination, which increases the $V_{\rm oc}$ [54].

Table 2.1.: Overview of the different preconditioning techniques and their influence on the solar devices V_{oc} , capacitance C_{cell} , conductivity σ , and FF [55].

Preconditioning		References
Red Light	$V_{\rm oc} \uparrow, C_{\rm cell} \uparrow, \sigma \uparrow$	[56-59]
Blue Light	$FF\uparrow$	[60]
White Light	$V_{\rm oc} \uparrow$, $FF \uparrow$, $C_{\rm cell} \uparrow$, $\sigma \uparrow$	[48, 50, 51, 54, 57]
Forward bias	$V_{\rm oc} \uparrow, C_{\rm cell} \uparrow$	[48, 50-52, 61, 62]
Reverse bias	$C_{\text{cell}} \uparrow, FF \downarrow$	[61, 63-65]

Further research started to distinguish between metastable effects resulting from different preconditioning techniques. The results are summarized in Table 2.1. The effect of illumination was separated into effects resulting from red and blue light. Also the influence of reverse bias on the metastable states was analyzed. As the illumination with red light (energy less then the CdS band gap) led to an increase of the open circuit voltage and the capacitance as well as the conductivity, it was assumed that the red light is sufficient to excite the amphoteric defects responsible for PPC effect describe above [56]. Blue light was found to cause an increase of the solar cells FF. In [60] the effect was explained by holes that occupy acceptors within the CdS layers and increases its n-doping and conductivity. This increase was expected to decrease photocurrent barriers that inhibit the collection of photocurrent when no blue light is present.

However, further experiments lead to the assumption of Fermi-level pinning at the CIGS/CdS interface due to a large density of donor-like states. The Fermi-level pinning would no longer allow a change of a photocurrent barrier at the interface. Thus, the idea was replaced by the introduction of a p+ layer (a highly acceptor-doped layer) into the CIGS absorber close to the interface [66]. The p+ layer would act as a photocurrent barrier but may be reduced due to blue light as holes generated in the CdS may reach it and reduce it [67]. Reverse bias led to a decrease of the FF of a sample while its capacitance increases [56, 65]. The effect was explained by Cu-ions migrating away from the interface, leaving behind negative charge that serves as a barrier for the photo induced electron current [68].

As all the discovered metastable effects seem to originate from the CIGS absorber material, Lany and Zunger did first-principle total energy calculations to

search for possible defects responsible for the metastable changes [69]. They found that the Se vacancy $V_{\rm Se}$ can show two different defects states, i.e. a bonding Indium-Indium (In-In) state and an anti-bonding In-In state. When the $V_{\rm Se}$ defect is populated it is electrically neutral V_{Se}^0 and results in a short In-In bond. When the $V_{\rm Se}$ defect is depopulated it becomes positively charged (V_{Se}^{2+}) and the In-In distance increases, which results in a shift of the bonding and anti-bonding state towards higher energies. The lattice relaxation between the two states makes the changes metastable. Which state is dominant depends on the occupations of the defects states and therefore on the position of the Fermi-level. An occupation of the anti-bonding states becomes only possible at large Fermi-energies but results in negatively charged states.

Furthermore, Lany and Zunger found that the formation energy of the selenium copper divacancy defect complex $(V_{Se}-V_{Cu})$ is smaller then formation energy of the isolated selenium vacancy. The divacancy complex behaves similar to the isolated one except that its charge properties are different. The V_{Se}^{2+} defect becomes the $(V_{Se}-V_{Cu})^+$ state and acts as a shallow donor, while the (V_{Se}^0) states becomes the $(V_{Se}-V_{Cu})^-$ state and acts as a shallow acceptor. The conversion processes between the states were described by configurations coordinate diagrams and the dominating processes are described in the following reaction processes

$$(V_{\rm Se} - V_{\rm Cu})^+ + e \to (V_{\rm Se} - V_{\rm Cu})^- + h$$
 (2.10a)

$$(V_{\rm Se} - V_{\rm Cu})^- + 2h \to (V_{\rm Se} - V_{\rm Cu})^+.$$
 (2.10b)

The conversion of a donor into an acceptor by the capture of a generated free electron and emission of a hole is given by Equation 2.10a. At the same time a thermal activation across a barrier of 0.1 eV is needed. Equation 2.10b describes the conversion of an acceptor into a donor. This reaction needs the capture of two holes and an activation energy of 0.35 eV. The activation energies may change depending on the Ga content in the CIGS. Which configuration is dominant depends, as already mention on the position of the Fermi-level within the bandgap. Where the Fermi-level is close to the valence band the donor state is dominant, but free electrons due to the illumination with (red) light accelerate the conversion into an acceptor. The increase of acceptors results in the mentioned decrease of the SCR width and decreased recombination (increase of V_{oc}). A p+-layer close the interface may also be explainable with the $V_{\mathrm{Se}} - V_{\mathrm{Cu}}$ defect complex as it should act as an acceptor when the Fermi-level is closer the conduction band, which is the case at the interface. Blue light accelerates the conversion into donors at the interface due to the injection of holes from the CdS layer and reduces the p+-layer [56, 70].

Furthermore, Tobias Eisenbarth proposed that a back contact barrier in CIGS solar cells plays an essential role when trying to explain metastable effects [56, 71]. He analyzed in detail the properties of the shallow N1-defect, which was formerly assumed to be located near the CIGS/CdS interface [72]. However, Eisenbarth

interpreted the defect as a hole barrier at the back contact of the solar cell, as he found that the activation energy of the defects is only lowered by preconditioning techniques that affect the electron concentration at the back of the solar cell. This barrier was described to be resulting from donor like defects (e.g. $(V_{\rm Se} - V_{\rm Cu})$). A change in the electron concentration would converse the donors into acceptors reducing the metastable barrier. This change in the barrier is seen as the metastable effect.

Nevertheless, metastabilities in CIGS solar cells remain a highly discussed issue. More recent research show that the acceptor to donor conversion of the selenium copper divacancy defect complex is not sufficient to explain the measured magnitude and timescales of metastable changes on its own, but suggest that additional defects play a role [73–75]. Thus, more research is needed to understand metastabilities in CIGS. The topic remains important especially for the CIGS industry. Metastabilities influence the performance of installed CIGS solar modules and complicate the performance prediction and power rating, which are crucial to estimate the value of a CIGS module. Additionally, the correct preconditioning technique of a CIGS solar cell or module that may be used to measure a performance in the lab that is relevant for the behavior of the solar cell in the field is still missing [76, 77].

2.4. Luminescence of Solar Cells

2.4.1. Physics

Luminescence of solar cells is another term for the radiative recombination described in Section 2.1.3. The luminescence is inherently linked to the absorption of light by the solar cell [78]. This connection was used to develop the reciprocity relation [15], which applicability to solar cells was extensively analyzed [79, 80]. The measuring of luminescence of solar cells is very interesting as it yields information about the absorption and charge carrier collection properties of a solar cell, which are relevant for the performance of a solar cell. Luminescence can be measured by injecting charge carriers into a solar cell either by the injection of current [electroluminescence (EL)] or by illuminating the sample [photoluminescence (PL)]. A formula describing the luminescence (EL and PL) ϕ^{em} in general was developed by U. Rau in [16] and reads

$$\phi^{em}\left(E,T,V_{\rm j}\right) = \phi^{\rm sc}\left(E\right) + Q_{\rm e}\left(E\right)\phi_{\rm bb}\left(E,T\right) \left[\exp\left(\frac{eV_{\rm j}}{kT}\right) - 1\right]. \tag{2.11}$$

The equation also holds for a situation where a sample is illuminated, but not kept at open circuit and instead operated with an additionally modulated external voltage. In this work this situation is called electro-modulated luminescence (EM-PL). Equation 2.11 is in the following related to as the reciprocity relation.

The quantity ϕ^{sc} describes a voltage independent part of the luminescence that results from the illumination of the sample. The quantity $Q_{\rm e}$ is the so called external quantum efficiency of the solar cell. This quantity describes the probability that a photon of certain energy is absorbed by the solar cell and creates a current. The hemispherical radiation per unit energy of a black body is described by $\phi_{\rm bb}$ which reads [27]

$$\phi^{bb}(E,T) = \frac{2\pi E^3}{h^3 c^2} \frac{1}{\exp\left(\frac{E}{kT}\right) - 1},$$
 (2.12)

where h is the Planck constant and c is the velocity of light. It follows that we cannot expect luminescence at arbitrarily large energies as the emission is suppressed by the black body spectrum part in Equation 2.11. Additionally the luminescence in Equation 2.11 is depending on the so called junction voltage V_j . When the reciprocity relation was derived, the junction voltages described in principle the quasi-Fermi level splitting within the solar cell in the space charge region, where the dominant parts of the recombination took place. However, when the Equation 2.11 is applied to thin-film solar cells where the space charge region takes up a large part of the absorber the junction voltages needs to be rather understood as the average quasi-Fermi level throughout the cell [81].

The advantage of the concept of the junction voltages lies in the fact that it can also be understood in the context of an equivalent circuit. When describing a solar cell using the equivalent circuit from Figure 2.4 the junction voltage $V_{\rm j}$ would correspond to the voltage across the diode. Thus, it is given by

$$V_{\rm i} = V_{\rm ext} - JR_{\rm s},\tag{2.13}$$

where $V_{\rm ext}$ is the voltage at the contacts.

Certain conditions have to be fulfilled to use Equation 2.11. The luminescence spectrum has to be compatible with the quantum efficiency of the device and the spectrum must not change at different bias conditions. Additionally, the total luminescence should follow a diode law with the ideality factor of one. If the ideality factor is not one, e.g. due to recombination via tail states, the reciprocity relation might still be usable, but then the ideality factor needs to be measured at first [82]. Finally, Equation 2.11 also demands a linear superposition of the luminescence resulting from illumination and biasing. It was found that those conditions are fulfilled for mono-crystalline silicon solar cells [83]. Additionally, was the viability of the reciprocity relation for several thin-film solar cell technologies discussed in detail in the work of Thomas Müller [27] and he concluded that the reciprocity relation is also applicable to CIGS solar cells.

2.4.2. Imaging Methods

Luminescence imaging enables the acquiring of two-dimensional information about a solar cells properties and became popular with the work of Fuyuki et. al who was

the first to use luminescence imaging on silicon solar cells [14]. The luminescence emitted by a solar cell is measured spatially resolved using cameras with a silicon or InGaAs detector. In the following different methods were developed to use the resulting luminescence images to localize and quantify varying properties and defects of solar cells.

Most luminescence imaging methods focus on the determination of a local series resistance or dark saturation current [21, 22]. These properties were found to be quite variable especially for silicon solar cells. The methods often make use of the reciprocity relation to determine first a junction voltage image, which is then used for further calculations. How a junction voltage image is determined from a luminescence image in this work is discussed in more detail in Section 3.1.3, although the exact procedure applied by others may vary in details.

As underlying model to describe the two-dimensional nature of a solar cell and locally varying properties, the first imaging methods used the so called *independent diode model* (see Figure 2.9 (a)). This model divides a solar cell into several smaller equivalent circuits, each of them describing a certain location in the sample and each of them may be different. The equivalent circuits are connected in parallel. Thus, each diode, relating to a certain position on the sample, is connected with a well defined series resistance to the terminals. Such a model simplifies a solar cells real physical properties but has the advantage that it allows to define a local series resistance independently from the properties of other locations.

When assuming an independent diode model a local series resistance can be determined by applying Equation 2.13 to each location. However, although the local junction voltage can be determined from luminescence images, the local current J may also vary and is more complicated to determine. The different methods to determine a local series resistance differ mainly in their procedure to determine a local current. In [23] the local current is determined with the combined use of lock-in thermography and luminescence imaging. The thermography image is scaled using the total dissipated power to obtain a locally dissipated power image. The local current is in the following determined by dividing the locally dissipated power image by the local junction voltage obtained from luminescence imaging. However, this method assumes that all the locally dissipated power is lost over the pn-junction which is not necessarily the case. Another, way to determine the local current would be to assume a dependence of the local current on the local junction voltage. Such approaches only work if the variations in the local dark saturation current are expected to be small [21] or may be determinable from a local calibration constant obtained from the determination of the junction voltage image [24, 25]. Another method, determining not only the local series resistance but also the local dark saturation current, is using several luminescence images to fit for each position a function relating the local series resistance and local dark saturation current to the local luminescence signal, local junction voltage and external voltage [22].

The independent diode model does not consider that in a real solar cell all local

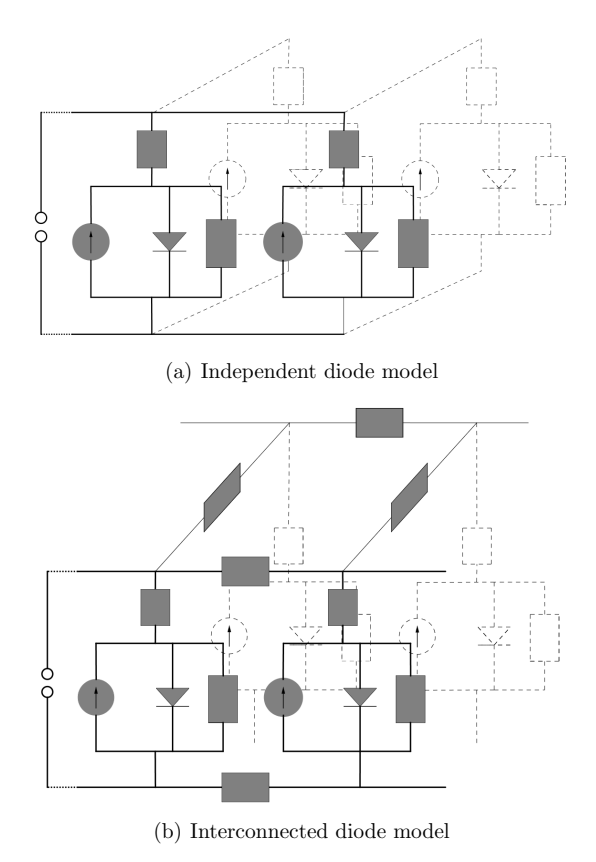


Figure 2.9.: Sketch of two-dimension equivalent circuit models used for the derivation of luminescence imaging methods. While the independent diode model is simpler the interconnected diode model is much closer to the real physical properties of a solar cell.

diodes are connected via a resistive layer and are therefore interconnected with a finite distributed resistance. A more physically correct two-dimensional model is therefore the interconnected diode model shown in Figure 2.9 (b). The relevance of the interconnection can be easiest explained, when assuming a large shunt at a certain position in the solar cell. In the independent diode model, the voltage would only drop at the position of the shunt, as the others areas are connected in parallel to the shunt. Within an interconnected diode model the junction voltage will also drop across the areas neighboring the shunt. The current will take the path of least resistance, which is through the shunt. Due to the interconnection the voltage drop resulting from the current flow through the series resistance to the shunt is also relevant for the non-shunted region and will reduce the voltage drop in these regions across the diode. Furthermore, the interconnected diode model allows the presence of so called balancing currents. When a solar cell is illuminated, the photocurrent generated at one location may not only flow across the contacts of the device but may also flow in a circuit within the solar cell, for example again due to a shunt. These balancing currents are not possible in the independent diode model as the resistance towards the contacts will always be smaller than the resistance towards a different location in the sample.

Thus, all imaging methods based on the independent diode model are bound to fail when larger local variations of the cell properties are present [84, 85]. One method that does not assume an independent diode model is based on the use of the Laplacian operator to calculate from local voltage changes the local current flow in the z-direction of a device [86, 87]. However, this method relies on images having a very good signal to noise ration and correct image deconvolution processes [88]. Another imaging method that does not assumed an independent diode model is the photocurrent collection efficiency method, which is tested, discussed and further developed in this work (cf. Chapter 6).

Additionally, it needs to be mentioned that due to the interconnection of areas in a solar cell or module it is often not trivial to estimate from the knowledge of local properties their actual influence on the performance of a solar cell. For example depends the power loss due to a shunt in a certain area not only on the size of the shunt but also on the series resistances in other areas. To correctly estimate the effects certain local properties have on the overall solar cell performance network simulations need to be applied that are able to simulate a solar cell including all its (assumed) local variations [89]. A comparison of different simulations with and without certain defects may then give information about the importance of a certain area for the performance of a solar cell.

3. Experimental Methods and Simulations

This chapter describes all the experimental setups and simulation programs used in this work. Additionally, it will be shown how the results of the experiments or simulations can be processed to obtain further information. The basics of electrical characterization of solar cells are explained briefly and the used imaging setup and measurement procedures are described in detail, as the work is mainly about luminescence imaging. Afterwards, a short overview over the samples used in this work is given. In the second part of this chapter the simulation programs PVMOS and SCAPS are introduced, which were used for three and one-dimensional device simulations, respectively.

3.1. Experiments

3.1.1. Current/Voltage Characterization

Current density/voltage (J/V) characteristics are measured regularly for all analyzed solar cells. They are essential to analyze basic parameters of the solar cells, but also to test simple experimental conditions like the contacting of a sample. A current/voltage characteristic is measured by a source-measurement unit, which automatically sweeps through a set voltage range and measures the current at defined steps. The characteristic can be measured in the dark or under illumination. The standard test conditions to determine the main solar cell parameters $J_{\rm sc}$, $V_{\rm oc}$, FF and η (cf. Section 2.2) under illumination dictate an illumination close to the AM 1.5 G spectrum at 25 °C [90].

To reach standard test conditions the J/V characteristics are measured using a steady state sun simulator or a so called flasher. The steady state sun simulator uses a xenon and a halogen lamp to reach the acquired spectral conditions, while the flasher only employs a single xenon lamp. Both systems count within their defined area sizes (8 \times 8 cm² for the steady state and 120 \times 180 cm² for the flasher) as class A setups, showing only small spectral mismatch and spatial intensity inhomogeneities of less than 2 %. The measurements with the sun simulator are used to obtain the voltage and current regions relevant during luminescence imaging.

Additionally, J/V measurements are possible in the luminescence imaging setup

(cf. Section 3.1.3). However, this setup does not have the possibility of a real sun spectrum illumination. Thus, the measurements under standard test conditions in the sun simulators were used to set the illumination intensities in the PL setup to adequate values.

3.1.2. Short Circuit Current/Open Circuit Voltage Characterization

Another electrical characterization method of solar cells used in this work is the measurement of so call short circuit current/open circuit voltage $(J_{\rm sc}/V_{\rm oc})$ characteristics [91]. For this characteristic the short circuit current and open circuit voltage is measured at several different illumination conditions and then plotted against each other. The special property of the resulting characteristic is that it only describes the recombination properties of a solar cell without the influence of series resistance. Under open circuit conditions no current flows through the sample and therefore no voltage drops over a series resistance. If we assume that at short circuit conditions all charge carriers are extracted from the sample, then the short circuit current describes the current recombining within the solar cell at open circuit conditions. Thus, plotting the short circuit current versus its corresponding open circuit voltage yields a characteristics that describes how much current recombines within the solar cell depending on the junction voltage (at open circuit conditions the junction voltage is equal to the open circuit voltage).

As a $J_{\rm sc}/V_{\rm oc}$ characteristic is not influenced by series resistance a comparison with a usual dark J/V characteristic can be used to measure the series resistance $R_{\rm s}$ of a solar cell at different currents in the dark. For that the external voltages $V_{\rm ext}$ measured at a certain current density J needs to be compared to the open circuit voltage that is measured when the corresponding short circuit current is equal to J. The equation reads

$$R_{\rm s} = \frac{V_{\rm ext}\left(J\right) - V_{\rm oc}\left(J_{\rm sc} = J\right)}{J}.\tag{3.1}$$

It is also possible to use a $J_{\rm sc}/V_{\rm oc}$ characteristic to determine the series resistance at a certain illumination for different currents. For that the $J_{\rm sc}/V_{\rm oc}$ characteristic needs to be compared with a J/V characteristic measured under the desired illumination condition. Additionally, it has to be assumed the current recombining within the solar cell is equal to the current, measured during the illuminated J/V sweep, added to the short circuit current $J_{\rm sc,JV}$ of the J/V characteristic. It follows

$$R_{\rm s} = \frac{V_{\rm ext} (J) - V_{\rm oc} (J_{\rm sc} = J + J_{\rm sc, JV})}{J}.$$
 (3.2)

In this work $J_{\rm sc}/V_{\rm oc}$ characteristics were measured using the illumination source in the luminescence imaging setup (laser, see Section 3.1.3). Using an easily tun-

able illumination source like a laser or LED has the advantage that the $J_{\rm sc}/V_{\rm oc}$ characteristic can be measured automatically. A program can be used to sweep the illumination intensity from zero to a certain value in small steps and a source measurement unit measures $J_{\rm sc}$ and $V_{\rm oc}$ at each illumination step. As an alternative filters could be used to change the illumination intensity of a stable light-source, but setting up an automated filter change or changing filters manually is more experimentally challenging.

3.1.3. Luminescence Imaging

Setup

Most of the experiments used for this work are performed within a luminescence imaging setup. Figure 3.1 shows a sketch of the setup. In principle everything needed to perform electro- and/or photoluminescence imaging is a source measurement unit, an illumination source and a camera. As a camera the setup makes used of a Princeton Instruments Nirvana640 InGaAs Camera with a resolution of 640 x 512 pixels. Within the same setup it is also possible to use an Apogee Imaging System Si-CCD camera with a resolution of 3056 x 3056 pixels. However, for this work only the InGaAs camera is used as its sensitivity for the emitted spectrum of the luminescence light is superior and therefore its signal to noise ration is much better [82]. This also leads to lower exposure times and therefore faster imaging. The usual exposure times with the InGaAs camera range for CIGS solar cells from 30 to 500 ms, depending on the applied voltages and the defects analyzed.

As a light source the setup makes use of a 90 W 808 nm diode laser. The laser is widened using a beam homogenizer to obtain a maximum deviation of the average illumination intensity of 5% on $20 \times 20 \, \mathrm{cm}^2$. The intensity of the laser can be set by varying its current. Illumination intensities up 1.3 suns equivalent are possible. To avoid an accidental exposure to the invisible laser light, the sample stage is placed within a cabinet and the laser is secured with an interlock so that it can only be turned on when the cabinet door is closed. The cabinet is also needed to reduce the influence of stray light on the luminescence imaging process. The laser is cooled using water cooling, but it is still prone to overheating when turned on to long (> 5 min). When constant illumination over longer timescales is needed it is also possible to use within the setup four white LEDs, which can reach also an intensity of one sun equivalent depending on their positioning. However, the homogeneity of the LED illumination is worse than the laser illumination.

Within this work two different source measurement units were used to set and measure the electrical state of the solar cells. A Keithley 238 source measurement unit is used for all the CIGS samples. It range goes up to 100 mA and 110 V or 1 A and 15 V, which is sufficient for these samples. For the c-Si solar cells a Keithley 228A source measurement unit is used, which has range of 10 A and 10 V. This

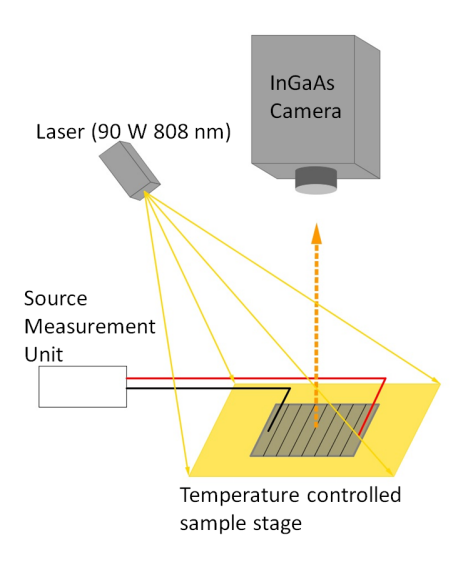


Figure 3.1.: Sketch of the setup used to measure electro- and photoluminescence images. The setup consists of a camera to measure the luminescence radiation of a solar cell, an illumination source (laser) to excite photoluminescence, and a source measurement unit to apply a bias to a sample to excite electroluminescence in the dark or electro-modulated photoluminescence under illumination. The analyzed solar cell is placed on a temperature controlled stage and can be electrically contacted. The source measurement unit, the laser and the camera can all be externally controlled via a computer. The sample stage and the camera are placed within a cabinet to avoid the influence of stray light on the measurements and to avoid accidents due to the laser light.

was needed as the c-Si solar cells exhibits much higher current densities mainly due to their larger cell size.

The sample is placed on a temperature controlled stage. The temperature was controlled by peltier elements, which were in turn cooled by water cooling. The elements allow for a temperature range from $15\,^{\circ}$ C to $85\,^{\circ}$ C. The temperature was monitored and controlled using a Pt-100 sensor that is placed next to the sample.

Electrical contacting of sample is done either by rows of spring contact pins, which can be positioned at arbitrary distances, or by single spring contacts, which can be positioned using manipulators fixed on magnetic stands. Four point measurements are used. This setup allows for maximum flexibility when contacting solar cells from the front, which is the case for the analyzed CIGS solar cells. When contacting solar cells from the back sticky silver tape was used to lead the contacts out. The tape is then contacted via alligator clips. This procedure can lead to larger series resistance, as the contacts of the silver tape to the cell is not perfect and the four point measurement cannot be fixed directly at the cell contacts but is fixed at the silver tape (which might also add to the resistance).

All the parts of the setup can be externally controlled via a computer and for all the parts Labview libraries were either available or written. This allows for highly flexible experiment design and automation. Thus, experiments can be fastened a lot as the desirable conditions for images can be set via a program, which then runs automatically and takes images at all the different illumination conditions or biases set.

Junction Voltage Imaging

An essential part of the luminescence image processing performed in this work is the calculation of junction voltage images. This process transfers a luminescence image with a local intensity given by a number of counts into an image where the pixel intensity describes the junction voltage of a solar cell. This means that after the image processing junction voltages of the same solar cell under the same operating conditions should look the same independent of the camera, which is used for imaging. The procedure used in this work for determining a junction voltage image was published in [92], but will be described in the following for the sake of completeness.

The dependence of the luminescence intensity is given by Equation 2.11 in Section 2.4.1. Thus, for EL images or for EM-PL images, after subtracting an image where we assumed the junction voltage to be zero, the local image intensity S_{cam} is given as

$$S_{\text{cam}} = \int Q_{\text{cam}}(E)Q_{\text{e}}(E)\Phi_{\text{bb}}(E)\exp\left(\frac{V_{\text{j}}}{V_{\text{th}}}\right)dE.$$
 (3.3)

Here, Q_{cam} is the sensitivity of the used camera to light of a certain energy E and V_{th} is the thermal voltage equal to e/kT.

Taking the natural logarithm of the signal intensity and multiplying with the thermal voltage yields a non-calibrated junction voltage V_i ' image

$$V_{\rm i}' = V_{\rm th} \ln (S_{\rm cam}) = V_{\rm i} + C,$$
 (3.4)

where C is a constant which includes the quantum efficiency of the solar cell, the camera sensitivity and the black body spectrum. This constant has to be determined to obtain a real junction voltage image. In this work, the determination of C will be named as the calibration of the junction voltage image.

For the solar cells analyzed in this work the assumption was made that C is position independent. With this assumption the calibration is possible with an image where we can assume that the average junction voltage is known. Two cases come into consideration. The first case would be an image taken in the dark with a low amount of injected current. In that case a low amount of voltage drops across any series resistance and it can be assumed the average local junction voltage over the active sample area A is equal to the external voltage applied. The second case would use an image taken while the sample is under illumination at open circuit conditions. Under these operating conditions no current flows and therefore the average local junction voltage is expected to be equal to the open circuit voltage measured externally. In this work, the second case is used as the available setup has the option of PL imaging and the use of an open circuit voltage image has several other advantages. The open circuit voltage image has a larger intensity than a low current image and is therefore less affected by noise. Also it ensures that no current flows; hence no voltage drops across any series resistance, which in the dark at a low current only holds approximately.

However, both mentioned calibration processes can be described with the following equation

$$C = \frac{1}{A} \int V_{j}' dA - V_{\text{ext}}.$$
 (3.5)

Here, V_j ' needs to be calculated from a luminescence image taken under low injection conditions or an image taken under illumination and open circuit voltage, and $V_{\rm ext}$ is the respective external voltage at which the image was taken. The spatial average of V_j ' across the active sample area is used for the calibration as V_j still might vary due to local differences in the diode properties or shunts and the average of the V_j over the entire active area is more likely to be equal to the external voltage than just a local V_j value.

Once C is determined it may be used to calibrate images taken at arbitrary conditions using the same setup and settings. For example in this work the calibration constant determined from a PL image is used to determine the junction voltage images measured in the dark via EL.

Determination of the Series Resistance from Luminescence Images

By determining the average junction voltage of a solar cell at different currents it is possible to determine a $J/V_{\rm j}$ characteristics for a solar cell (cf. Chapter 5). This characteristic describes similar to a $J_{\rm sc}/V_{\rm oc}$ characteristic the properties of a solar cell without the influence of series resistance. Thus, it is possible to obtain from luminescence images a $J_{\rm sc}/V_{\rm oc}$ characteristic of a solar cell.

Additionally, it was shown in Section 3.1.2 (Equation 3.2) how a $J_{\rm sc}/V_{\rm oc}$ characteristic can be used to determine the total series resistance at different operating conditions of a solar cell. Thus, a $J/V_{\rm j}$ characteristic is equally suitable to calculate the series resistance. It is easily done by replacing the open circuit voltage in Equation 3.2 with the measured junction voltage

$$R_{\rm s} = \frac{V_{\rm ext}(J) - V_{\rm j}(J)}{J}.$$
(3.6)

Although the J/V_i characteristic might differ slightly from the $J_{\rm sc}/V_{\rm oc}$ characteristic of the solar cell (cf. Section 5.2) there are advantages which justify the use of J/V_i characteristics to calculate the series resistance. Firstly, is the presented measurement procedure less influenced by metastable changes or temperature variations during the measurement. Once the calibration constant is determined for the junction voltage image, a series resistance value can be determined for any operating point with a current/voltage measurement and a simultaneously taken luminescence image. In contrast determining the series resistance with the $J_{\rm sc}/V_{\rm oc}$ characteristic requires two electrical measurements at different illumination conditions. In between the measurements, metastable changes or temperature variations can always occur that then lead to errors in the $R_{\rm s}$ determination. Secondly, it is also interesting to determine $R_{\rm s}$ under illumination. Doing that with $J_{\rm sc}/V_{\rm oc}$ characteristics requires precise shifting of the characteristic by the generated photo current within the solar cell $(J_{\text{sc,JV}}, \text{ cf. Equation 3.2})$. If the shift cannot be precisely determined due to a photocurrent loss even under short circuit conditions additional errors are introduced. When a J/V_i characteristic is used to determine the series resistance no current shifting is needed as the current value is the same for electrical measurement and the image.

3.1.4. Sample Overview

CIGS Samples: Manz

In this work most of the CIGS samples were industrially produced by the MANZ CIGS Technology GmbH. In the vicinity of the project OptiCIGS the company delivered several minimodules and cells. For the cells every second p3 line of an industrial module was not patterned and material was removed perpendicular to the scribing lines so that one cell was divided into several small cells with a length

of only $1.6\,\mathrm{cm}$ and a width of $0.4\,\mathrm{cm}$. Afterwards the module was cut so that one substrate of $10\,\mathrm{x}\,10\,\mathrm{cm}^2$ contained up to $44\,\mathrm{single}$ cells which can be individually contacted. The contacting was performed over the front contact of the adjacent cells of the cell to be analyzed. This was possible due to the missing p3 lines. To contact the TCO, wires were soldered directly to the TCO using ultrasonic soldering. A photo of the substrate with the several contacted cells is shown in Figure 3.2. An example photovoltaic parameter set for the analyzed cells is shown in Table 3.1.

Table 3.1.: Photovoltaic parameters of an analyzed CIGS cell produced by Manz.

$J_{\rm sc}~[{\rm mA/cm^2}]$	$V_{\rm oc}$ [V]	FF [%]	$\eta~[\%]$
29.21	0.71	68	14.2

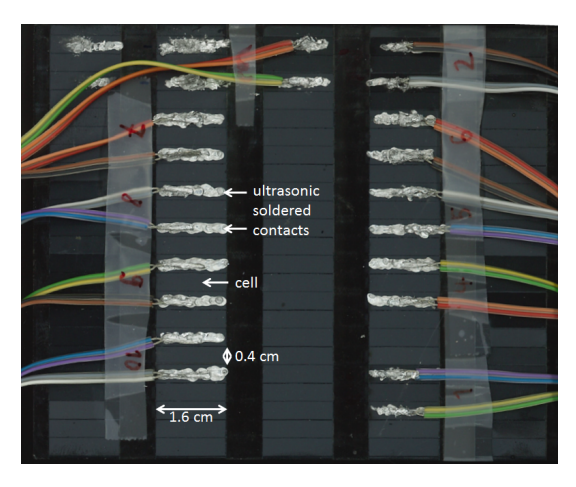


Figure 3.2.: Photo of the substrate produced by MANZ from a real industrially produced module, which exhibits several individually contactable cell.

The minimodules analyzed in this work were also cut from industrial sized modules and contained 17 cells which were 0.4 cm wide and 8.6 cm long. The cells were connected monolithically as described in Section 2.3.1 at the long sides. To contact the module spring contacts pins are place on the outer most cells of the module. On the positive side of the module the p3 line was not patterned to allow a contacting via the front contact. A photo of a sample module with descriptions where the contacts are placed is shown in Figure 3.3. The photovoltaic parameters of an example minimodule without any visible defects is given in Table 3.2.

Table 3.2.: Photovoltaic parameters of an analyzed CIGS minimodule produced by Manz.

$J_{\rm sc}~[{\rm mA/cm^2}]$	$V_{\rm oc} [V]$	<i>FF</i> [%]	η [%]
26.53	11.57	73.8	13.3

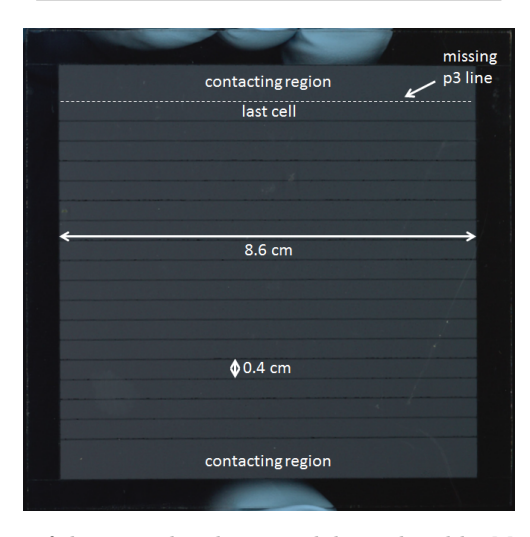


Figure 3.3.: Photo of the an analyzed minimodule produced by Manz. To contact the sample, spring contact pins are placed in the contacting regions. Note, that the last p3 line on the top is missing (indicated by dashed line) to contact the last cell via the front contact.

CIGS Samples: Bosch

To analyze a sample with larger spatial inhomogeneities a CIGS sample produced by Bosch Solar CISTech GmbH is used in this work (cf. Section 6.2). This sample was contacted on the front via a grid. The sample cell is $1.2 \times 0.9 \, \mathrm{cm^2}$ large and the front contact grid consists of four fingers. The sample was contacted via spring contact pins that were placed on the grid and beside the sample where the back contact was laid bare. Eight cells were produced on one glass substrate. A photo of the substrate with the solar cells is shown in Figure 3.4. The photovoltaic parameters of a sample are given in Table 3.3. Note however, that the results are given for the whole area of the cell and not active area. The contacting scheme leads to some shadowing which reduces the solar cell performance.

Table 3.3.: Photovoltaic parameters of an analyzed CIGS minimodule produced by Bosch.

$J_{\rm sc} \ [{\rm mA/cm^2}]$	$V_{\rm oc} [{ m V}]$	FF [%]	η [%]
16.92	0.57	65.6	6.3

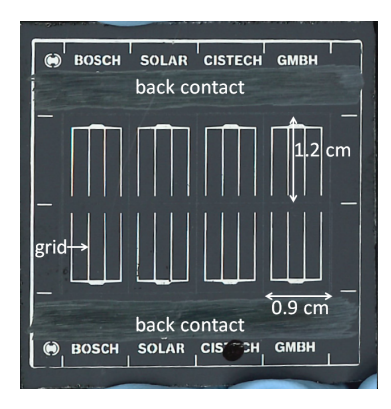


Figure 3.4.: Photograph of the solar cells produced by Bosch. Eight cells are positioned on one glass substrate. The front exhibits a grid for contacting while the back is contacted via the bare molybdenum.

c-Si Sample

To test new measurement procedures, a mono-crystalline silicon solar cell was used in this work. The sample is $12.5 \times 12.5 \,\mathrm{cm}^2$ large. The front the sample exhibits a grid consisting of two bus-bars and several fingers. The bus-bars were contacted via several spring contact pins. To contact the back of the solar cell silver tape is placed on the back contact and lead out. A photo of the sample can be seen in Figure 3.5. The photovoltaic parameters of the sample are given in Table 3.4. Note, that the sample showed some cracks and additionally the contacting scheme via the silver tape showed a high series resistance that reduced the performance of the sample.

Table 3.4.: Photovoltaic parameters of an analyzed c-Si Solar cell.

$J_{\rm sc}~[{\rm mA/cm^2}]$	$V_{\rm oc}$ [V]	FF [%]	η [%]
32.7	0.61	65.15	13.0

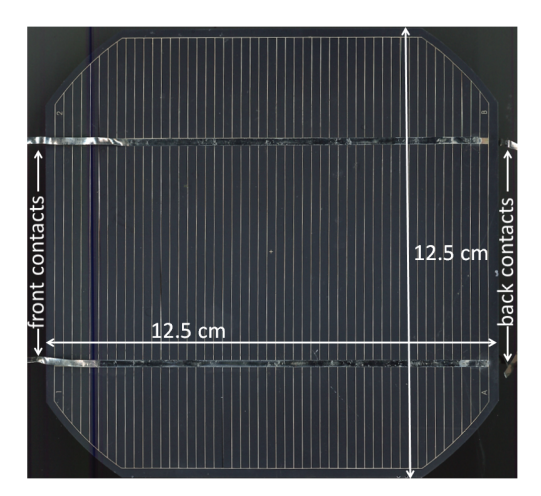


Figure 3.5.: Photo of the crystalline silicon solar cell used for the experiments. The front was contacted via pins on the bus-bars or as shown in the image via silver tape. The back is also contacted via silver tape.

3.2. Simulations

This section introduces the programs which are used in this thesis to simulate the luminescence and electrical measurements. One dimensional device simulations were performed using the program SCAPS to simulate CIGS solar cells using the basic semiconductor equations. To model the two dimensional aspects of luminescence images the program PVMOS was used which works with an equivalent circuit network.

3.2.1. SCAPS

The program SCAPS [93] was developed especially to model CIGS solar cells. In principle the program solves in one dimension the Poisson equation (Equation 2.2a) and the continuity equations (Equations 2.2b and 2.2c) for the charge carrier densities and the electrostatic potential at any point of a stack of up to seven semiconductor layers. The generation is calculated from definable absorption and transmission constants.

Parameters

A large number of parameters needs to be set for the simulations. First the geometric properties of the solar cell is defined by setting a thickness d for each semiconductor layer of the solar cell. Second the properties of the individual semiconductor layers have to be set. These properties include the bandgap $E_{\rm g}$,

the electron affinity χ , relative dielectric permittivity $\epsilon_{\rm r}$, the conduction and valence band density of states $N_{\rm c,v}$, the electron and hole mobility $\mu_{\rm e,h}$, the thermal velocity $v_{\rm th}$, the acceptor or donor doping $N_{\rm A/D}$, and a radiative recombination constant B. Additionally, defects are introduced which determine the non-radiative recombination (cf. Section 2.1.3). The relevant properties of the defects are their capture cross section for electrons and holes $\sigma_{\rm e,h}$, their position within the bandgap $E_{\rm T}$ (above the valence band, if not otherwise mentioned), their characteristic energy $\sigma_{\rm T}^{\rm E}$, which defines the gaussian distribution of the defect density around $E_{\rm T}$, and their peak density $N_{\rm T}$.

The base parameter set used in this work to simulate a CIGS solar cell was mostly taken from [94] and [95]. These works were performed by project partners on similar cells also from MANZ, which proposes the use of these parameters also for the present analysis. Two slightly different sets were developed for two different metastable states (one dark annealed state and one light soaked state). An overview of the parameters is given in Table 3.5, where the values in brackets refer to the values in the dark annealed state. The gallium content x in the CIGS absorber was graded linearly from the back to the front contact from 0.5 to 0.22, resulting in a larger bandgap at the back. As absorption parameters for the CIGS layer a standard set provided together with the SCAPS program was used (which considered the gallium grading), and for the ZnO absorption coefficients measured by the project partners were used. Additionally, in alignment with the experiments, an external series resistance of $3.5 \,\Omega \text{cm}^2$ was added.

Determining Series Resistance

Using SCAPS simulations it is also possible to simulate the total series resistance of a device at any given operating point with an approach similar to the experimental approach discussed before that uses the luminescence of a device (cf. Section 3.1.3). First the radiative recombination in the device is calculated by determining the electron hole product everywhere in the device. Simplifying, it was assumed that the sum across all this local radiative recombination within the device, yields the total luminescence signal of the device. From the luminescence signal we can now calculate the junction voltage of the device using the approach discussed in Section 3.1.3. And by using Equation 3.6 it is again possible to calculate the series resistance for the device. The series resistance calculated in this way not only includes the external series resistance, which is manually set, but also all the resistive effects resulting from the charge carrier transport through the semiconductor.

3.2.2. PVMOS

To model the two dimensional luminescence imaging results using a device simulator as SCAPS would be too calculation intensive. Thus, in this thesis the free and

Table 3.5.: List of parameters used for the SCAPS simulations of CIGS devices within this thesis. Values in bracket correspond to a dark annealed state of the solar cell.

	CIGS	CdS	iZnO	ZnO:Al
$d [\mu m]$	1.92	0.06	0.07	0.87
$E_{\rm g}$ [eV]	1.36-1.1808	2.4	3.3	3.33
χ [eV]	4.2-4.368	4.27	4.47	4.47
$\epsilon_{ m r} \; [{ m r.u.}]$	13.6	10	9	9
$N_{\rm c} \ [{\rm cm}^{-3}]$	$2.2 \cdot 10^{18}$	2.2×10^{18}	2.2×10^{18}	2.2×10^{18}
$N_{\rm v}~{ m [cm^{-3}]}$	1.8×10^{19}	1.8×10^{19}	1.8×10^{19}	1.8×10^{19}
$v_{\rm th} \ [{\rm cm/s}]$	10^{7}	10^{7}	10^{7}	10^{7}
$\mu_{\rm e}~[{\rm cm^2/Vs}]$	60	100	100	100
$\mu_{\rm h}~{ m [cm^2/Vs]}$	5	25	25	25
$N_{\mathrm{A/D}}~\mathrm{[cm^{-3}]}$	$4.9 \times 10^{16} \ (3.8 \times 10^{15})$	5×10^{17}	5×10^{17}	10^{20}
$B [cm^3/s]$	2×10^{-9}	-	-	-
Defect 1				
Type	Donor	Acceptor	Neutral	Neutral
$\sigma_{\rm e}~[{ m cm}^2]$	10^{-14}	8×10^{-17}	10^{-12}	10^{-12}
$\sigma_{\rm h} \ [{\rm cm}^2]$	10^{-14}	8×10^{-12}	10^{-12}	10^{-12}
$E_{\rm T} \ [{\rm eV}]$	0.094 (0.119) (below EC)	0 (above Ei)	1.65	1.65
$\sigma_{\mathrm{T}}^{\mathrm{E}} \; [\mathrm{eV}]$	0.018 (0.016)	0.1	0.1	0.1
$N_{\rm T} \ [{\rm eV^{-1}cm^{-3}}]$	$3.16 \times 10^{16} \ (1.1 \times 10^{16})$	4.514×10^{17}	9.986×10^{16}	$9.99E \times 10^{16}$
Defect 2				
Type	Acceptor			
$\sigma_{\rm e}~[{\rm cm}^2]$	3×10^{-14}			
$\sigma_{\rm h} \ [{\rm cm}^2]$	10^{-14}			
$E_{\rm T} \ [{\rm eV}]$	0.227 (below EC)			
$\sigma_{\mathrm{T}}^{\mathrm{E}} \; [\mathrm{eV}]$	0.05			
$N_{\rm T} \ [{\rm eV^{-1}cm^{-3}}]$	1.41×10^{15}			

open-source solar module simulator PVMOS developed by Bart E. Pieters was used [96]. With PVMOS it is possible to represent a solar cell with a network of distributed resistors and diodes and a finite differences approach is used to solve the relevant differential equation of the network. Furthermore, PVMOS features a variable adaptive mesh which allows for efficient simulation of small features within a large solar cell or module.

A solar cell is modeled with PVMOS in the simplest case using three layers. A 'solar cell layer' is placed between a front and a back contact layer. The front and back contact layer are a two dimensional (in the following understood as the x-y dimension) network of connected resistors, which can be defined by setting a sheet resistance. The contact layers are connected at their nodes via the 'solar cell layer'. Here, each connection between the nodes of the electrodes (in the z-direction) is given by a one- or two-diode equivalent circuit model or just a resistance (to represent a shunt). The properties can be locally varied to allow the simulation of inhomogeneities or to implement the monolithic interconnection of thin-film modules. If needed, additional layers can be used to introduce additional electrodes, such as a contacting grid, or additional solar cell layers (e.g. for tandem solar cells).

Table 3.6.: Major parameters used to simulate the experimental measurements of CIGS cells and modules with PVMOS.

$J_{0,1} [{\rm A/cm}^2]$	$J_{0,2}$ [$[A/cm^2]$	$J_{\rm sc}~[{\rm A/cm^2}]$
1.55×10^{-1}	^{.3} 1.9	0×10^{-8}	0.0283
$R_{\rm i}~[\Omega {\rm cm}^2]$	$R_{\rm f} \left[\Omega\right]$	$R_{\rm b} \left[\Omega\right]$	$R_{\rm p2}~[\Omega {\rm cm}^2]$
0.3	24	0.6	4×10^{-7}

For the simulation of luminescence measurements performed on CIGS solar cells or modules a parameter set was developed, which reproduces the experimentally found properties of the analyzed samples well. The geometric properties are adjusted to the respective samples. A two-diode model is used to represent the solar cell layer. The dark saturation currents $J_{0,1}$ and $J_{0,2}$ can be easiest deduced from the open circuit voltage. More difficult to estimate are the different resistances. The front and back contact resistances ($R_{\rm f}$ and $R_{\rm b}$) of the ZnO and the Molybdenum were estimated from measurements performed by MANZ. Additionally an internal series resistance $R_{\rm i}$ of the solar cell layer describing the transport through the bulk of the CIGS is defined as well as the resistance of the p2 laser line $R_{\rm p2}$, which connects the different modules. Both resistances can have a significant influences on the solar cells behavior and they were estimated so that the electrical characteristic of the modules fits to the measurement. However, no automated

fitting was used as especially the effects resulting from the resistance parameters are correlated. A list of the parameters used is given in Table 3.6.

Table 3.7.: Major parameters used to simulate a c-Si Solar cell with PVMOS.

$J_{0,1} [{\rm A/cm^2}]$	n_{id}	$J_{\rm sc}~[{\rm A/cm^2}]$	$R_{\rm i}~[\Omega {\rm cm}^2]$	$R_{\rm f} \left[\Omega\right]$	$R_{\rm b} \left[\Omega\right]$
7×10^{-11}	1.19	0.035	0.004625	40	0.0005

To simulate new imaging methods on a different type of solar cell, also a baseline parameter set for the simulation of a crystalline silicon solar cells exhibiting a grid was developed. The grid contains bus-bars and fingers, which have a sheet resistance of $2.4\times10^{-3}\,\Omega$ and $3\times10^{-6}\,\Omega$, respectively and are placed on top of the transparent emitter with the sheet resistance $R_{\rm f}$. For the silicon layer only a one-diode model is used with an ideality factor $n_{\rm id}$. The parameters are given in Table 3.7.

4. Experiments in the Presence of Metastabilities

As discussed in Section 2.3.2 CIGS solar cells are subject to metastable changes. As these metastable changes alter the electrical properties of a CIGS solar cell depending on illumination and bias it follows that the luminescence signal of a CIGS solar cell is also altered. This was already shown in [97] and [98].

For quantitative analysis of luminescence images of CIGS samples it is mandatory to avoid the influence of metastable changes. Thus, it is required to determine the influence and understand the timescales on which metastable changes are happening. In this chapter it is analyzed in detail how biasing and light alters a CIGS solar cell and how the changes are seen in luminescence measurements. Furthermore, a mechanism published in literature to explain metastabilities in CIGS is investigated using device simulations in comparison to experimental results. Finally, the measures taken to avoid an influence of metastable changes on the experimental results are described. These measures are in effect throughout the rest of the work.

4.1. Experimental Procedure and Results

Open Circuit Voltage Transients under Illumination

We start the discussion of metastabilities with an experiment observing the changes happening to a sample under illumination and open circuit. For the experiment a $1.6 \times 0.4\,\mathrm{cm^2}$ CIGS solar cell from Manz (Section 3.1.4), is first kept for several hours in the dark, and is subsequently illuminated with white light from LEDs within the luminescence measurement setup. The intensity was set in a way that the short circuit current of the solar cell was approximately equal to the short circuit current measured under an AM 1.5 G spectrum.

Several cycles of the excitation of the solar cell with light were run. Each cycle consisted of six hours of illumination and every 20 seconds the open circuit voltage of the device was measured, while simultaneously a photoluminescence image was taken. From the luminescence image a $V_{\rm j}$ ' image is calculated as discussed in Section 3.1.3. Between the cycles, breaks were taken where the LEDs were turned off and the sample was allowed to relax. The duration of each break was varied from one to four hours in one hour steps. Hence, we obtain additional information

about the relaxation process between the different illumination cycles.

Figures 4.1 shows the results of the experiment. At the beginning of each illumination cycle the open circuit voltage decreases fast and starts to rise afterward (Figure 4.1 (a)). It is assumed that the initial decrease happens due to an increase in temperature that is caused by the illumination. The temperature increase can be estimated from the change in the open circuit voltage. The temperature dependence of $V_{\rm oc}$ is given by [99]

$$qV_{\rm oc} = E_{\rm a} - n_{\rm id}kT \ln(\frac{J_{00}}{J_{co}}),$$
 (4.1)

where $E_{\rm a}$ describes the activation energy of the recombination rate and J_{00} is a prefactor of the dark saturation current density J_0 . If we assume E_a to be 1.2 eV close to the bandgap of CIGS, J_{00} and $n_{\rm id}$ to be temperature independent and the temperature of the device at the beginning of the illumination to be 298 K, Equation 4.1 yields a temperature change of approximately 10 K at the beginning of the third excitation step ($V_{\rm oc}$ changes from 0.681 V to 0.663 V). This temperature change seems large, but it is not unrealistic. Although the temperature of the stage below the sample is controlled, the setup cannot counter the heating due to the illumination, as between the solar cell and the cooling stage lies the 3 mm thick glass substrate.

The increase of the open circuit voltage after the initial decrease caused by heating is attributed to a metastable change of the solar cell. This change is happening over a long time as the sample does not stabilize even after six hours of illumination. In these six hours the open circuit voltage increases by about 1.5 %. That the increase is caused again by another change in temperature (e.g. by a delayed cooling effect of the stage) seems unlikely, as such a process should stabilize within six hours.

After each illumination cycle the temperature of the sample changes again such that an exact value for the amount of relaxation that is happening in the dark is difficult to obtain. However, when comparing the last $V_{\rm oc}$ value of an illumination cycle with the lowest $V_{\rm oc}$ of the next cycle it is visible the sample relaxed in the dark and that the sample relaxes more if the time in the dark is increased. However, even four hours of relaxation is not enough to bring the sample back to a state before the six hours of illumination.

The trend of the average cell V_j ' (and therefore the luminescence intensity) is similar to the behavior of the open circuit voltage except that the initial decrease is smaller (Figure 4.1 (b)). The linked behavior of the open circuit voltage and the average cell V_j ' is clearly seen when looking at the offset C (the difference between the open circuit voltage and V_j ', Figure 4.1 (c)). The offset changes at the beginning of a each illumination cycle fast and is constant later.

In literature metastable changes were attributed to changes in the series resistance and non-radiative recombination [98]. The decrease in non-radiative recombination is reproduced in the present experiments. Changes in the series resistance

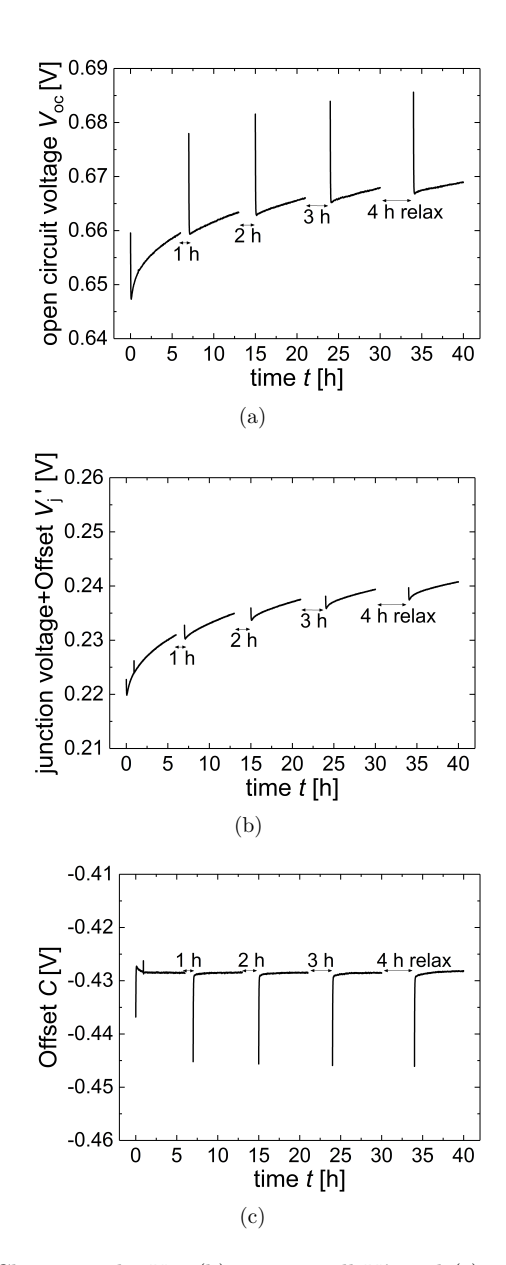


Figure 4.1.: (a) Change in the $V_{\rm oc}$, (b) average cell $V_{\rm j}$ ', and (c) calibrations constant C of a CIGS solar cell during 5 cycles of illumination with white light. Between each cycle the sample was kept in the dark for 1,2,3 and 4 hours

do not have an influence on the present measurements, as they are performed under open circuit. A constant offset C would be expected unless $Q_{\rm e}$ or the temperature change during the measurements (cf. Equation 3.4). As the changes in the offset happen on a similar timescale as the initial decrease of the open circuit voltage, which we attributed to a temperature change of the sample, the change in the offset is probably also resulting from a temperature change. As after some time the offset C is mostly constant, C is expected to be constant in the following experiments when the series resistance is observed.

Temperature and Injection Dependence of Metastable Changes

To get a better understanding on the metastable changes further experiments were performed. As experiments using illumination have to deal with larger temperature changes of a sample during the initial phase and are also influenced by instabilities of the illumination, it is in the following focused on operating conditions in the dark using current injection to induce the metastable changes. The metastable changes arising under these conditions are relevant for electro-luminescence measurements and are also expected to be at least similar to the dominant metastable changes arising under illumination and biasing of the sample (cf. Section 2.3.2).

A constant current is injected into a CIGS solar cell from Manz and the metastable changes are observed. At an interval of 10 or 20 seconds the external voltage $V_{\rm ext}$ is measured, simultaneously with a luminescence image. From the luminescence we can determine the change of the junction voltage $\Delta V_{\rm j}$ and the change of the series resistance $\Delta R_{\rm s}$ of the solar cell at a point in time t using

$$\Delta V_{j}(t) = V_{j}'(t) - V_{j}'(0) = V_{\text{th}} \ln(S_{\text{cam}}(t)) - V_{\text{th}} \ln(S_{\text{cam}}(0))$$
(4.2)

and

$$\Delta R_{\rm s}(t) = \frac{V_{\rm ext}(t) - V_{\rm j}'(t) - ((V_{\rm ext}(0) - V_{\rm j}'(0))}{I}. \tag{4.3}$$

As mentioned we assume here that the calibration constant C does not change due to metastabilities.

After the excitation the sample was relaxed in the dark under open circuit. The relaxation process was also recorded by taking measurements of the voltage and luminescence images at the same injected current as was used for the excitation, every five minutes. Compared to the excitation process the time between the measurements was longer and no current is injected between the measurements to allow the sample to relax.

The process of exciting the sample with an injected current and observing the subsequent relaxation was performed for various injected currents and temperatures. The measurements were automated for fixed temperatures, meaning that after a successful relaxation cycle automatically the next excitation started with

a different injected current. The temperature changes were manually set, which means that for each temperature a new measurement cycle was started. Between the experiments at different temperatures the sample relaxed for several days in the dark.

The duration of each excitation and relaxation process is determined for this experiment by a stabilization parameter $c_{\rm stab, stop}$. The stabilization of the sample is automatically monitored by calculating after a fixed set of measurements a stabilization constant. This stabilization constant is given by the difference between the maximum and minimum external voltage $(V_{\rm ext,max}, V_{\rm ext,min})$ value within a set of measurements divided by the average voltage $V_{\rm ext,mean}$ of the same set

$$c_{\text{stab}} = \frac{V_{\text{ext,max}} - V_{\text{ext,min}}}{V_{\text{ext,mean}}}.$$
(4.4)

As soon as $c_{\rm stab}$ falls below a certain threshold value $c_{\rm stab,stop}$ the excitation/relaxation was stopped. By controlling the measurement duration in this way it is ensured that after each excitation or relaxation the sample reaches a well defined state. At different temperatures $c_{\rm stab,stop}$ had to be adjusted, as values that reach an acceptable experiment time at some temperatures lead to much longer experiment times at different temperatures. At 25°C $c_{\rm stab,stop}$ was set so that the excitation and relaxation was stopped when the rate of change dropped below 0.042 %/h in the last 20 minutes of the measurements. At 40°C $c_{\rm stab,stop}$ was set so that the excitation and relaxation was stopped when the rate of change dropped below 0.15 %/h in the last 20 minutes of the measurements and at 55°C and 70°C $c_{\rm stab,stop}$ was set so that the excitation and relaxation was stopped when the rate of change dropped below 0.15 %/h in the last 40 minutes of the measurements. The procedure ensures that the eminent metastable changes are measured without needing to define an excitation length beforehand.

Figure 4.2 and 4.3 show the results of the various excitation and following relaxation cycles, at different temperature and injected currents. Always, the change in the external voltage $\Delta V_{\rm ext}$, the change in the junction voltage $\Delta V_{\rm j}$, and resulting change in the series resistance $\Delta R_{\rm s}$ are shown. The moment when the sample is starting to relax is always recognized by the significant kink in the curves. In general we observe that under all conditions the series resistance of the solar cell decreases due to the excitation. The junction voltage increases in most cases due to excitation. Only at low currents and low temperatures we also observe a decrease of the junction voltage. An increase of the temperature leads at most currents to an increase of the metastable change. Furthermore, we observe at low temperatures the change of the series resistance dominates the behavior of external voltage, as it also decreases. At higher temperatures the change of the junction voltage dominates the behavior of the external voltage.

Depending on the conditions, the series resistance and junction voltage change happen on different timescales. At low temperatures the junction voltage relaxes much faster then the series resistance does, while during excitation at higher

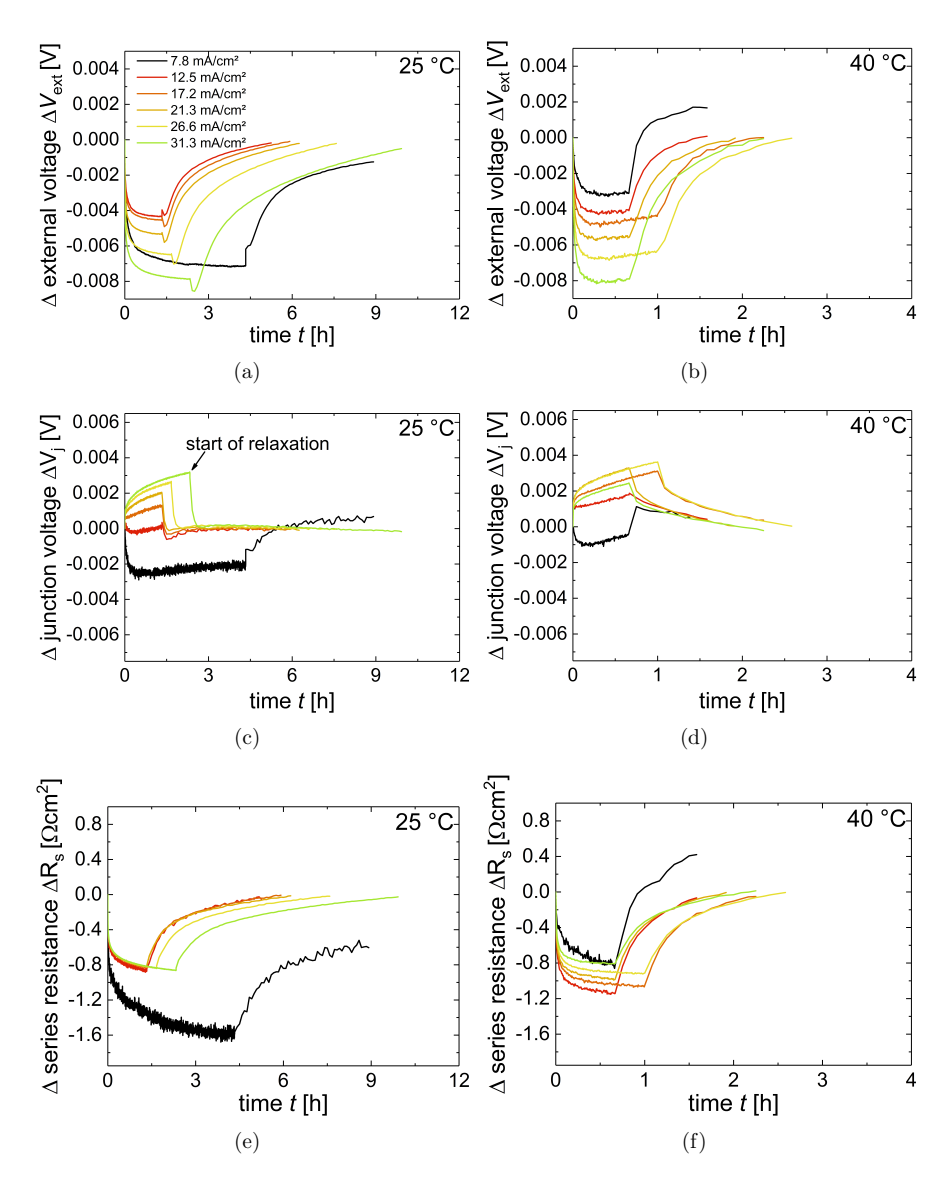


Figure 4.2.: Behavior of the external voltage, the junction voltage and the series resistance of CIGS solar cell during the excitation with different injected currents and the following relaxation at different temperatures: $25 \,^{\circ}\text{C}$ [(a),(c),(e)], $40 \,^{\circ}\text{C}$ [(b),(d),(f)]. The point in time where excitation stops and relaxations starts is always clearly visible at the kink in the curves [exemplarily marked in Figure (c)].

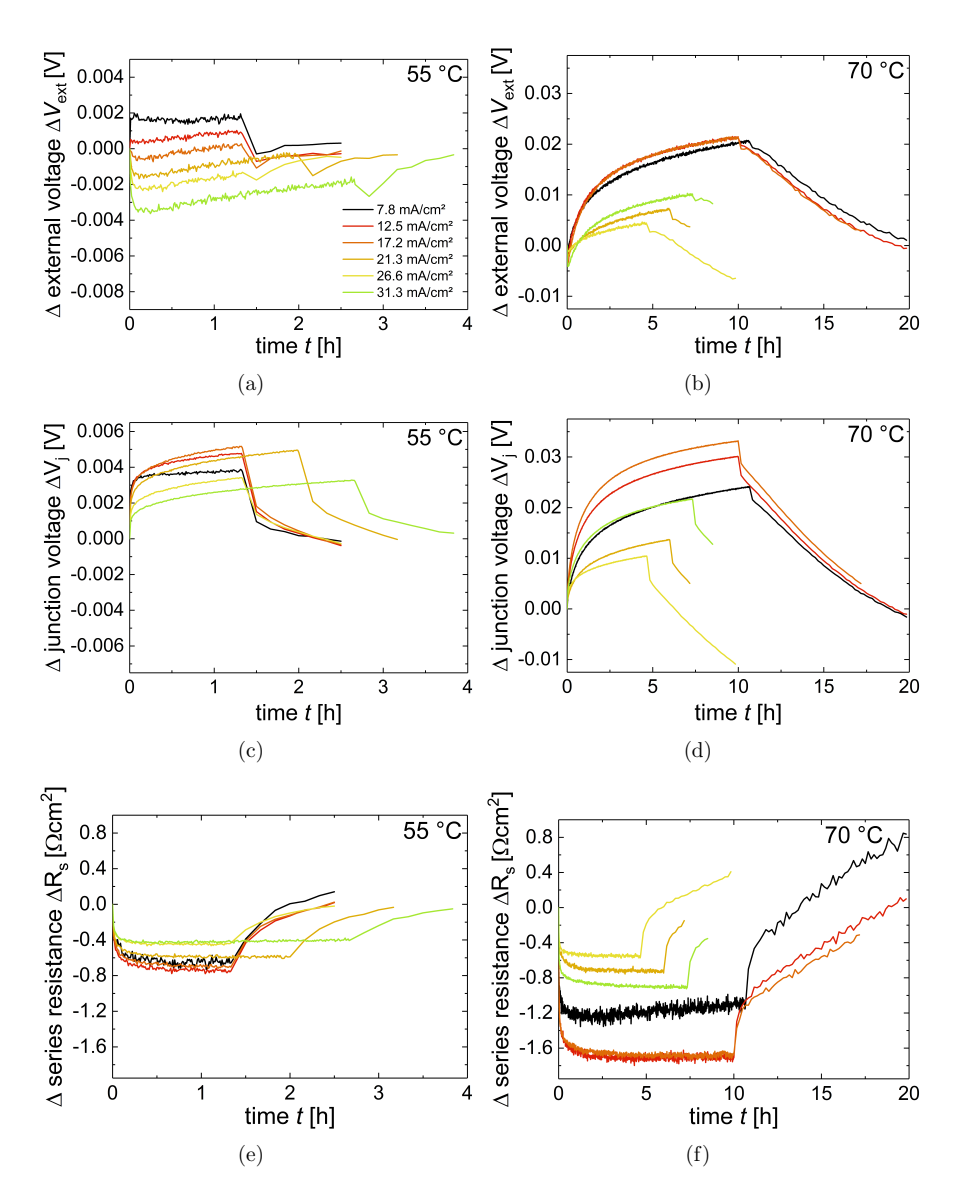


Figure 4.3.: Behavior of the external voltage, the junction voltage and the series resistance of CIGS solar cell during the excitation with different injected currents and the following relaxation at different temperatures: $55\,^{\circ}\text{C}$ [(a),(c),(e)], $70\,^{\circ}\text{C}$ [(b),(d),(f)]. The point in time where excitation stops and relaxations starts is always clearly visible at the kink in the curves.

temperatures the change in the junction voltage is still rising, when the series resistance has mostly stabilized (e.g. Figure 4.2 (c),(e) and Figure 4.3 (d),(f)). This tells us, that either at least two metastable changes happen within the sample that have different time constants, or that one metastable change exists in the sample that influences the two properties of the device (non-radiative recombination and series resistance) differently depending on the operating conditions.

The metastable changes often occur over timescales longer than hours, with no point of stabilization observable. Still, the initial change may be very fast (e.g. the external voltage changes at room temperature and an injected current of $31.3\,\mathrm{mA/cm^2}$ by 0.5~% in the first 30 seconds). This makes experiments that rely on a well defined metastable state extremely difficult, as they would need long preconditioning times (hours to days) and measurements that follow this preconditioning time immediately. It will be discussed in Section 4.2 how this issue is addressed in this work.

4.2. Simulations and Discussion

SCAPS Simulations

In the following it will be briefly discussed how the metastable changes observed are in alignment with current theories describing the metastable changes. The literature (cf. Section 2.3.2) states that light soaking or biasing leads to an increase of the doping concentration in the CIGS. This increase in doping leads to a decrease of the space charge region and in the following to a decrease of J_0 , which increases the open circuit voltage. The increase in open circuit voltage was also observed in our experiments.

SCAPS simulations are used to analyze such an increase in the doping concentration to see if it would also affect the series resistance. As parameter sets for an excited and relaxed state the sets given in Table 3.5 in Section 3.2.1 are used. The main difference between the two sets is the increased doping for the excited state.

Figure 4.4 (a) shows the dark current voltage characteristics simulated with SCAPS for the excited and relaxed state. From these characteristics the reduced J_0 in the excited state can be clearly seen, as the voltages increase at same currents. This reduced J_0 seen here is also responsible for an increase of the open circuit voltage under illumination.

The decrease in the J_0 is also seen in the experiment, as the junction voltage usually increases with the excitation. However, at room temperature this change was mostly overlapped by a decrease in the series resistance, which lead to an overall decrease of the external voltage with the excitation. The change in the series resistance between the two states was also determined in the simulations by using the method described in Section 3.2.1. For the light soaked and dark

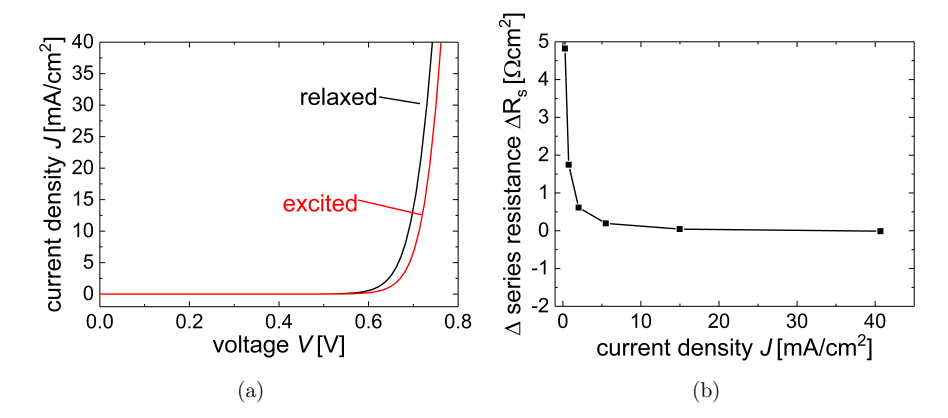


Figure 4.4.: (a) Dark current voltage characteristics for a relaxed and excited CIGS solar cell simulated with SCAPS. (b) Change in the series resistance of a CIGS solar cell resulting from an excitation modeled with SCAPS determined at different the current densities. The series resistance increases from the dark annealed to the light soaked state. The increase is larger at smaller currents and negligible at the currents for which the resistance was measured in the experiments. In the experiments a decrease of the series resistance was seen.

annealed state the total radiative recombination in the device is used to calculate a junction voltage of the device, which we use further in combination with the external voltage to determine the series resistance at various current densities. The difference of the series resistances at the two states is shown in Figure 4.4 (b). It is seen that the series resistance increases in contrast to the experiments. Either an additional metastable change happens to the solar cell (which is not considered in the simulation), or the fixed parameters between the two states are not set correctly, as the influence of the change in doping concentration on the cell behavior depends also on the magnitude of other parameters.

On the Handling of Metastabilities in Experiments

It was shown that metastable changes happen over long and short timescales and that they influence the series resistance of a sample as well as its recombination properties. Additionally, the amount of change depends on the injected current and the temperature. All these factors, make a definition of a fixed metastable state via a preconditioning method difficult. A valid preconditioning would need long times and immediate measurements after the precondition procedure. Thus, only one sample could be preconditioned at a time and any failure during the measurement procedure, or measurements after initial test measurements (e.g. to determine a correct integration time for a camera) would require an additional

preconditioning step. Furthermore, even if a certain metastable state could be reached in a reproducible manner, it would be expected that further changes appear during a measurement procedure.

In this work it was attempted to minimize the influence of metastable effects on the measurements without a preconditioning step. When luminescence measurements are used in combination with electrical measurements, the electrical measurements are taken simultaneously to the images to ensure that both measurements are performed when the sample is in the same metastable state. It is relevant that the sample is for both measurements in the same state and it was not important to know in which state the sample is. Sometimes a comparison between measurements is necessary that cannot be taken at the same time, for example measurement in the dark and under illumination (Chapter 5). In these cases it was ensured that the found results were not caused by metastable changes by changing the experiment order and repeating the measurements often. Additionally, most of the measurements were performed automated, to ensure fast and well defined measurement times. Thus, metastable changes are reduced or at least kept constant among all the measurements.

Still, metastable changes cannot always be avoided. When a result is suspected to be due to a metastable change in the sample it will be mentioned. However, most results of the further chapters could be reproduced via simulations which did not include any metastable changes showing that the avoidance of metastable changes with the mentioned measures works well (Chapter 7).

4.3. Conclusion

It was shown that an excitation of the analyzed CIGS solar cells with light or bias results in a decrease of non-radiative recombination and a decrease of the series resistance. These effects happen fast (in matter of seconds) as soon as a sample is excited but keep going over long timescales (in the range of hours to days), which makes a stabilization of the sample time-consuming.

Using SCAPS simulations the complexity of finding an appropriate model to described the metastabilities is briefly discussed. The effect of decreasing series resistance could not be reproduced with simulations where the doping density is increased (which is often stated as the dominated cause of metastable changes, cf. Section 2.3.2).

Finally, it was described how the experiments in the further parts of this work are designed to avoid the influence of metastabilities on the results. Here, automation and simultaneous measurements of the images and electrical data are the leading measures used.

Understanding the effects metastabilities have on the behavior of CIGS solar cell is not only important for laboratory measurements, but it is primarily important to estimate the performance of solar cells in the field. Thus, achieving an adequate

model describing the metastable changes in CIGS solar cells is an important aim to make CIGS solar cells a more successful technology. Still, it has to be kept in mind that any model found might only hold for one type of CIGS cell produced in a certain way. Thus, working with and understanding metastable changes is an ongoing task.

Reconstruction of Current/Voltage Characteristics of Cells in Modules

This chapter focuses on the reconstruction of the current/voltage characteristics of individual thin-film CIGS cells within a module using luminescence imaging. Current/voltage characteristics of an entire module do not easily show if a reduced performance results from a single defected cell or rather properties of more than one cell. In contrast, luminescence imaging makes it possible to locate individual defects in cells or modules. There exist several publications that focus on the use of luminescence imaging for the characterization of modules [92, 100, 101]. The work in [92] is extended in this Chapter to measurements under illumination that are especially interesting for possible outdoor measurement in daylight. Parts of the results were published in [102].

5.1. Experimental Procedure and Results

The experiments were performed using the CIGS mini-modules introduced in Section 3.1.4. Figure 5.1 shows an example of the different luminescence images taken at different external voltages and illumination conditions (in the dark and under illumination with the laser intensity set in a way that the short circuit current is similar to the short circuit current under standard test conditions) of a module with no significant defects (module (A)).

We observe in the images how the sheet resistance of the CIGS sample influences the images at different conditions. The front contact resistance in CIGS is higher than the back contact resistance, causing the different sides of a single CIGS cell to have different series resistances, as the current has to travel either a longer or shorter way through the higher resistive front contact. In the present case the left side of each cell has the lower series resistance. In the dark this leads to a larger luminescence intensity at this side especially at higher currents. At lower voltages the current flow through the resistance is too low to lead to a significant difference in the voltage drop. Under illumination the effect is reversed if the cell operates below its open circuit voltage. The luminescence intensity is increased at the high resistive side as the charge carriers generated there have more difficulties to travel to the terminals of the device. Under conditions close to open circuit (Figure 5.1

(d)) we do not see any side having a larger luminescence intensity as no current is flowing and therefore no voltage is lost at either side across series resistance.

Also due to series resistance, larger intensity variations are seen in the luminescence intensity in the cell on the left side of the module (Figure 5.1 (b) and (c)). These intensity variations result from the contacting scheme. The module is contacted with five pins on the outer most cells, which are not shown in the image. Four of the pins carry current and one pin measures the voltage to achieve a four-point measurement. The series resistance is smaller for the areas closer to the current carrying pins, which results in the luminescence intensity around the pins being larger in the dark, and less under illumination and small voltages below $V_{\rm oc}$.

Furthermore, a difference between the luminescence images taken under illumination and in the dark (compare Figure 5.1 (a) and (b)) is observed. The images taken under illumination show a higher luminescence intensity. Series resistance is also responsible for this observation. At negative currents, the voltage drop across the series resistance is negative. As the sum of the junction voltage and the series resistance voltage must be equal to the external voltage (cf. Equation 2.13), a negative voltage drop across the series resistance leads to a junction voltage that is higher than the external voltage. The opposite is the case, when a positive current flows and the voltage drop across the series resistance becomes positive.

When looking at the images of a module with defects [module (B), Figure 5.2], it is possible to locate several shunts in different cells, as around the shunt the luminescence intensity decreases. At low voltages the area influenced by the shunt is larger, as the resistance of the rest of cell, which shows a normal diode behavior, is much higher compared to the shunt resistance. Therefore, the whole current through the cell stripe flows through the shunt and not through the rest of the cell, which reduces the junction voltage across the rest of the cell so much that it does not lead to a significant luminescence signal. The effect is more prominent in the dark than under illumination. In Section 5.2 it is analyzed if this higher luminescence intensity under illumination results from simple series resistance effects, as discussed in the previous paragraph.

Junction voltage images are calculated from the luminescence images with the procedure described in Section 3.1.3 (cf. Equation 3.4 and 3.5). Both, the measurements in the dark and under illumination are calibrated with the help of the open circuit voltage measured simultaneously to the determination of the luminescence images under illumination. For the calibration the average non-calibrated junction voltage values have to be determined for each cell, while the sample is at open circuit. The sum over the junction voltage averages of each cell is then set equal to the measured open circuit voltage. It was assumed that the calibration constant is position independent across the module. Figure 5.3 shows an example of two junction voltage images that are calculated from the respective luminescence images for the module with the shunts. Especially Figure 5.3 (a) indicates that such images can be used to determine the properties of different defects in

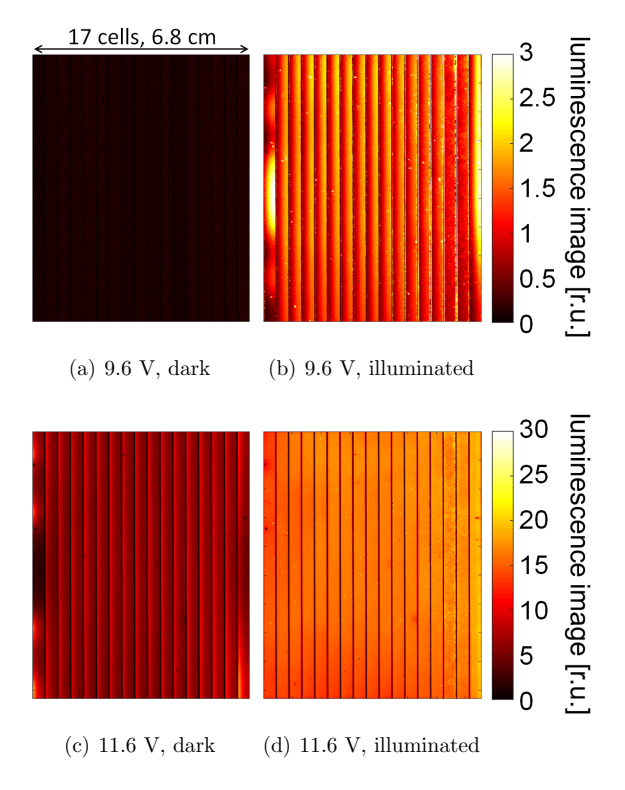


Figure 5.1.: Luminescence images of CIGS module (A) at different operating conditions. The samples $V_{\rm oc}$ is at approximately 11.6 V. Reprinted from [102], with the permission of AIP Publishing.

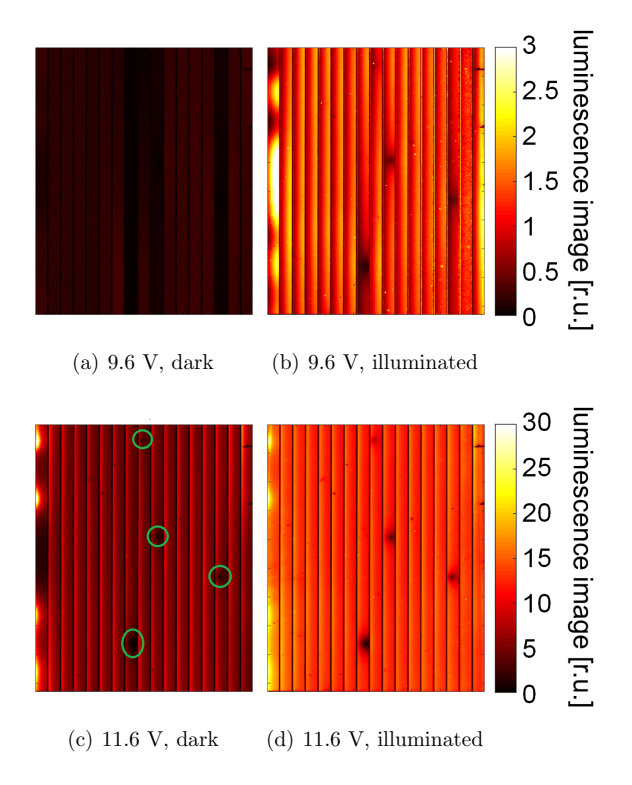


Figure 5.2.: Luminescence images of CIGS module (B) with several defects (shunts) at different operating conditions. The samples $V_{\rm oc}$ is at approximately 11.3 V. The shunts are marked with the green circles in Image (c). Reprinted from [102], with the permission of AIP Publishing.

a module as the shunts influence the junction voltages of the cells in which they occur differently.

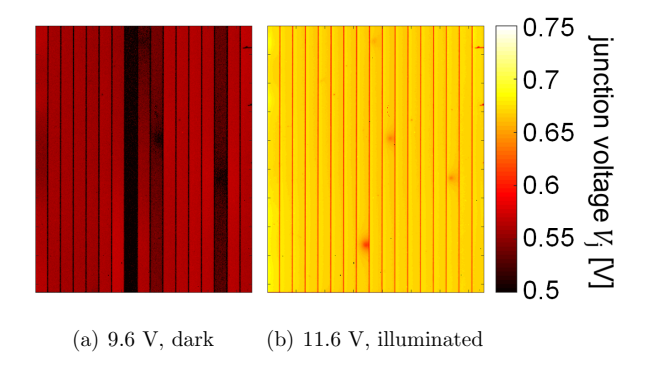


Figure 5.3.: Junction voltage images for CIGS module (B) with defects at two different operating conditions calculated from the respective luminescence images. Reprinted from [102], with the permission of AIP Publishing.

To obtain the current/voltage characteristics of individual cells, junction voltage images are measured at different operating points of the solar cell. A voltage ramp was applied while at the same time luminescence images are measured at each voltage step. Additionally, the current through the module was recorded. The process was performed with and without illumination. With this measurement procedure the J/V characteristic of the module is recorded simultaneously with the luminescence imaging.

For the J/V characteristic of a single cell in the module, the average of all the local junction voltages measured for a specific cell area is determined and plotted against the current density at which the image is taken (the current through each cell is the same as the current measured externally). From the images taken at different currents a complete characteristic can be determined. However, it is important to note, that the junction voltage images do not show the real voltages across each cell, as they do not include the voltages that drop across series resistance. Thus, the luminescence images provide us rather with a $J/V_{\rm j}$ characteristic of each cell. This characteristic excludes series resistance information and only provides information about the junction and resembles therefore more a $J_{\rm sc}/V_{\rm oc}$ characteristic. Like a $J_{\rm sc}/V_{\rm oc}$ -characteristic a $J/V_{\rm j}$ -characteristic includes information about possible shunt properties.

From the single cell $J/V_{\rm j}$ characteristics it is possible to calculate a $J/V_{\rm j}$ characteristic for the whole module simply by adding the cell junction voltages. Such a $J/V_{\rm j}$ characteristic for the whole module should in principle be very similar to the $J_{\rm sc}/V_{\rm oc}$ of the whole module, as the junction voltage images are calibrated with the help of the measured $V_{\rm oc}$. Note, that the $J_{\rm sc}/V_{\rm oc}$ characteristics can not be

easily measured for the individual cells in the module. In the following $J/V_{\rm j}$ characteristics determined under illumination will be denoted as electro-modulated photoluminescence (EM-PL) characteristics and $J/V_{\rm j}$ characteristics determined in the dark as electroluminescence (EL) characteristics.

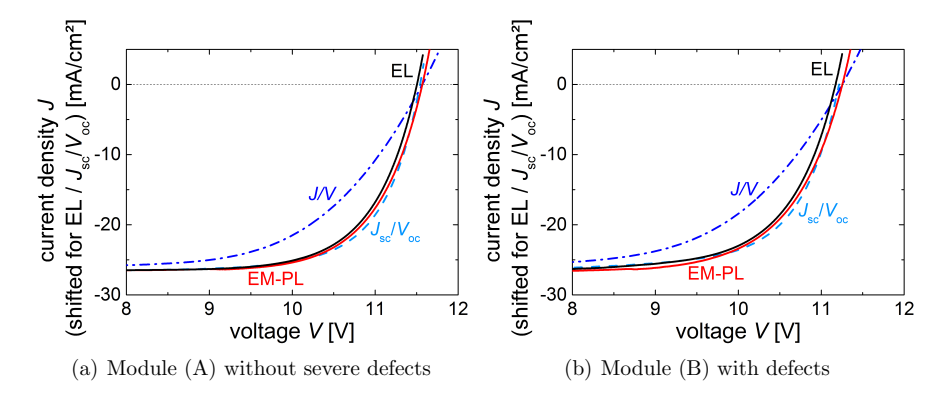


Figure 5.4.: Several current density/voltage characteristics determined for two different CIGS modules. The blue curves show J/V characteristics determined in the luminescence imaging setup using the laser as light-source and setting the illumination to one sun equivalent. The red curves show the EM-PL characteristics determined from imaging performed while the J/V characteristics were measured. The EL characteristics determined from imaging in the dark is shown in black. In light blue the $J_{\rm sc}/V_{\rm oc}$ characteristics are shown. The $J_{\rm sc}/V_{\rm oc}$ curves and EL curves are shifted by the short circuit current density. Reprinted from [102], with the permission of AIP Publishing.

Figure 5.4 shows the different current density/voltage characteristics determined for the module with defects and the module without any defects. As expected the EL and EM-PL characteristic differ from the actual J/V characteristic of the sample, as they do not include information of the series resistance. In principle both the EL and EM-PL characteristics are quite similar to the $J_{\rm sc}/V_{\rm oc}$ characteristic. However, a few minor differences are noticeable. First of all, the $V_{\rm oc}$ of the J/Vcharacteristic does not lie on $J_{\rm sc}/V_{\rm oc}$ characteristic. This is assumed to be a measurement error. Possible reasons for that are metastable changes of the sample between the measurements or temperature variations. Especially for the $J_{\rm sc}/V_{\rm oc}$ measurements temperature variations play an important role as the illumination changes during the measurement procedure. The EM-PL and EL measurements were calibrated with the $V_{\rm oc}$ of the J/V measurement performed simultaneously with the determination of the EM-PL characteristic to avoid any metastable or temperature variations between the measurements, at least for the EM-PL characteristic. For these reasons, it is not that surprising that there are slight differences between the $J/V_{\rm j}$ characteristics and the $J_{\rm sc}/V_{\rm oc}$ characteristics.

It is also seen in Figure 5.4 that the EL characteristic shows lower voltages than the EM-PL characteristic. This is surprising as for a single one-diode model both characteristics should be identical. The effect was seen in many measurements independently of what characteristic (EL or EM-PL) was measured first. Thus, it is not likely that the effect results from metastable or temperature variations.

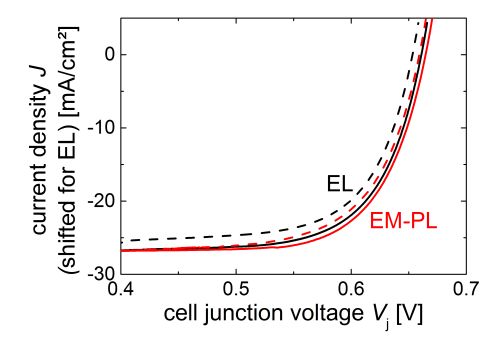


Figure 5.5.: Two example J/V_j characteristics of individual cells in the module determined via electroluminescence (EL) and electro-modulated photoluminescence (EM-PL) imaging. The characteristic determined via EL is shifted down by the short circuit current for better comparison. The dashed lines are the characteristics of a shunted cell in the module with defects (8th cell from the left). The solid lines show the characteristics of a cell without any defects in the same module (second cell from the left). Reprinted from [102], with the permission of AIP Publishing.

The actual aim of the measurement procedure is to obtain information about the individual cells in the module. Therefore, as an example, Figure 5.5 shows the $J/V_{\rm j}$ characteristics for a defected and non defected cell from the module (B), which exhibits the shunts. The shunted cell shows lower junctions voltages at all currents. Linear fits to the characteristics at low currents reveal the shunt strength in the individual cells if the shunt would be equally spatially distributed across the whole cell. The EL characteristics yield for the shunted and non-shunted cell values of $153\,\Omega{\rm cm}^2$ and $250\,\Omega{\rm cm}^2$, respectively, while the EM-PL characteristics yield for the shunted and non-shunted cell values of $140\,\Omega{\rm cm}^2$ and $452\,\Omega{\rm cm}^2$, respectively. Both, the EL and EM-PL characteristics, yield lower differential resistances for the cell with a defect. However, a quantitative difference is observed between the results obtained from EL and EM-PL. The difference is also seen in Figure 5.5, as the EL characteristics show lower junction voltages at the same injected currents. Additionally, the voltage difference between the shunted and non-shunted cell is larger for the EL characteristics.

These differences between the EL and EM-PL characteristics of the single cells and the whole module cannot be explained if the system is described with a one or two diode-model. Thus, the differences need to arise either from the laterally distributed nature of the solar module and cells or from cell/material properties

that are not included in a one or two diode-model.

5.2. Simulations and Discussion

With PVMOS it is possible to simulate a solar module including its distributed nature and in the following it is analyzed how much of the observed effects can be reproduced with simulations. For that it is first necessary to model the measured module with simulation. In PVMOS a module was defined which has the same geometric properties as the measured modules. It consists of 17 cells which are 8.57 cm long and 0.4114 cm wide including laser lines, making the active area width of a cell 0.38 cm. How the electrical parameters are determined is described in Section 3.2.2 and the parameters are given in Table 3.6.

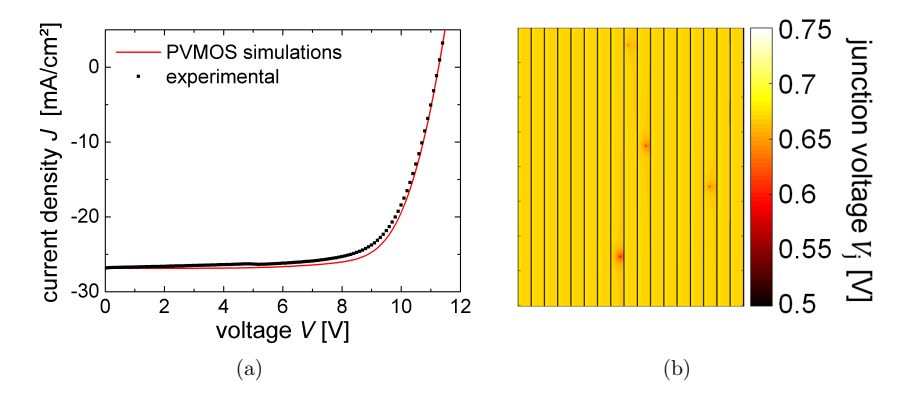


Figure 5.6.: (a) Comparison of the PVMOS modeled J/V characteristic and the experimentally measured J/V characteristic of the module including shunts. (b) Junction voltage image of the simulated module with defects at 11.6 V under illumination. The corresponding experimental junction voltage image can be seen in Figure 5.3 (b). Reprinted from [102], with the permission of AIP Publishing.

The shunts that were observed in the experimental measurements of one module were also added to the simulations. For that the position of the shunts in the module was taken from luminescence measurements. It is difficult to estimate the exact size and strength of the shunts as both influence their appearance in the luminescence and electrical measurements. Thus, both were adjusted so that values are reasonable and fit to the images and electrical measurements. The J/V characteristic of the simulated module is shown in Figure 5.6 (a), additionally to an example junction voltage image, showing the locations of the added shunts (Figure 5.6 (a)). Both results are close to the experimental results, which confirms that a module could be defined that mirrors the properties of the module analyzed

experimentally reasonably well [cf. also Figure 5.3 (b)].

With PVMOS and the obtained parameters we can now model the complete set of experiments performed in Section 5.1. The $J/V_{\rm j}$ characteristics are determined for the whole module and for the individual cells in the dark and under illumination from the local junction voltages. Figure 5.7 compares them to the J/V and $J_{\rm sc}/V_{\rm oc}$ characteristics of the whole module. It is obvious that the $J/V_{\rm j}$ characteristics follow more the $J_{\rm sc}/V_{\rm oc}$ characteristic as they do not include the series resistance like the J/V characteristic. At first glance it looks like the EL and EM-PL characteristics overlap a lot better with each other and the $J_{\rm sc}/V_{\rm oc}$ characteristic, which is not in agreement to the experimental measurements. However, when looking closer [Figure 5.7 (b)] it is noticeable that the junction voltages of the EL characteristics are lower at higher injected currents, which is also observed in the experiments. In the simulations the effect results from the spatially distributed nature of the solar module, which implies that this distributed nature is at least in part also responsible for the deviation observed between the EL and EM-PL characteristics in the experiments.

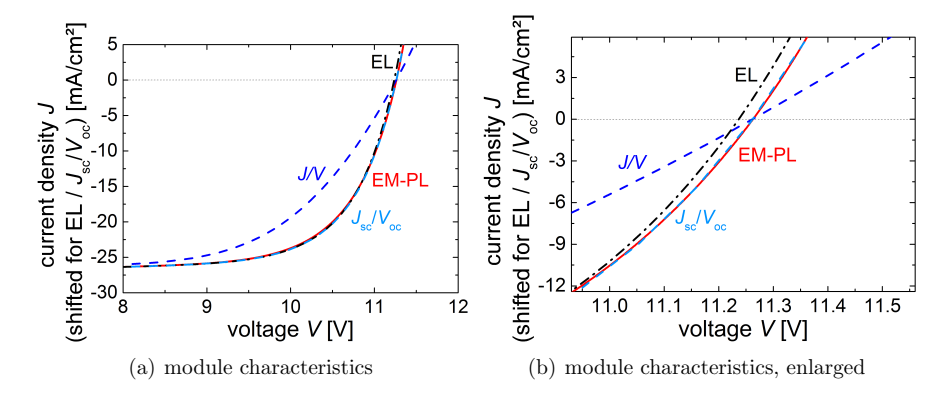


Figure 5.7.: Current density/voltage characteristics determined for a simulated CIGS module with shunts. The blue curve shows the J/V characteristics under illumination. The red curves show the EM-PL characteristics determined from the junction voltages under illumination. The EL characteristics determined from junction voltages in the dark are shown in black. In light blue the $J_{\rm sc}/V_{\rm oc}$ are shown. The $J_{\rm sc}/V_{\rm oc}$ curves and EL curves are shifted down by the short circuit current density. (b) shows the characteristics from part (a) enlarged around the open circuit voltage. Reprinted from [102], with the permission of AIP Publishing.

Considering the characteristics of the individual cells (Figure 5.8) we observe a behavior similar to the complete module. The $J/V_{\rm j}$ characteristics follow closely the $J_{\rm sc}/V_{\rm oc}$ characteristic. This also holds for the shunted cell. Note that $J_{\rm sc}/V_{\rm oc}$ characteristics of the individual cells in the module cannot be measured experi-

mentally without contacting individual cells. Also, the EL and EM-PL characteristic overlap in general well. In the experiments we observe significant differences between these two characteristics especially for the shunted cell also at low currents (cf. Figure 5.5). An enlargement of the characteristics [Figure 5.8 (b)] only reveals again differences between the EL and EM-PL characteristics at higher injected currents, which were already seen for the complete module. This is observed for the shunted and the non-shunted cells. Thus, it seems that the shunt influences the EL, EM-PL and $J_{\rm sc}/V_{\rm oc}$ characteristics in the simulation similarly. The effect responsible for the major differences in the EL and EM-PL characteristics at low injected current, which was seen in the experiments, was therefore not reproduced with the PVMOS modeling.

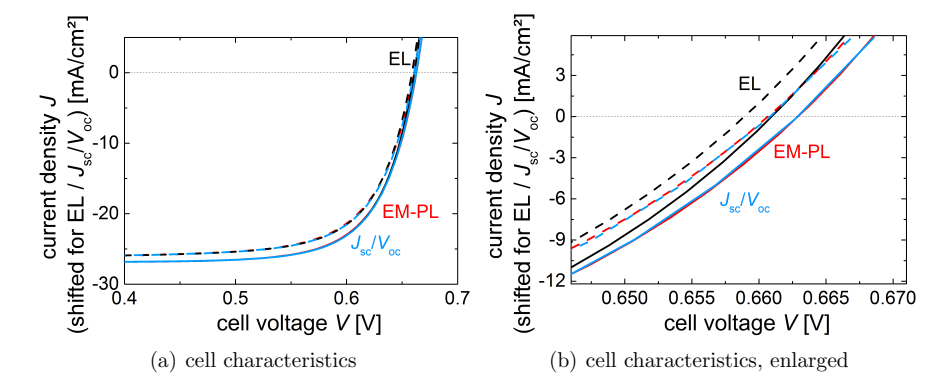


Figure 5.8.: Current density voltage characteristics determined for individual cells in a simulated CIGS module. The blue curve shows the J/V characteristics under illumination. The red curves show the EM-PL characteristics determined from the junction voltages under illumination. The EL characteristics determined from junction voltages in the dark are shown in black. In light blue the $J_{\rm sc}/V_{\rm oc}$ characteristics are shown. The $J_{\rm sc}/V_{\rm oc}$ curves and EL curves are shifted down by the short circuit current density. (b) shows the characteristics from part (a) enlarged around the open circuit voltage. Dashed lines are the characteristics of a shunted cell (8th from the left) and solid lines are characteristics of a non shunted cell (second from the left). Reprinted from [102], with the permission of AIP Publishing.

A possible explanation for the difference of experimental EL and EM-PL characteristics at low voltages could be imprecise shifting of the EL characteristic. The EL characteristic is shifted down to compare the EL and the EM-PL voltages at the same injected currents. As a shifting parameter the measured short circuit current under illumination is used. However, if the module is not able to collect all generated current under short circuit conditions it would mean that the amount of recombination under illumination is larger than expected, which would again lead to higher junction voltages. A possible reason for imperfect current

collection under short circuit conditions is a large series resistance. However, a series resistance so large is expected to influence the overall J/V characteristic, which is not the case. A possible solution would be in the form of an injection dependent series resistance as seen in thin-film silicon solar cells, which is large at low voltages but decreases with increasing voltage [103]. The idea of an injection dependent series resistance, its origin and effects, will be discussed in more detail in Chapter 7.

For now we focus on the differences of the EL and EM-PL characteristics seen at higher injected currents, which are seen in the experiments and in the PVMOS simulations. Thus, it is expected that the effect results from the spatially extended nature of the solar cell. The effect can be derived using a simplified solar cell model. The model is shown in Figure 5.9. It consist of two diodes, representing the pn-junction, two current sources, representing the generated photocurrent and a resistance $R_{\rm s}$. The two diodes are connected in parallel but diode Number 2 is also in series with the resistance. The two diodes represent the left and right area of a solar cell. One area has a higher series resistance than the other due to the higher front contact resistance compared to the back contact resistance.

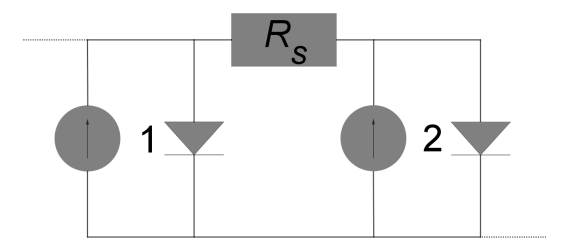


Figure 5.9.: Equivalent circuit model used to describe the origin of differences found between the EL and EM-PL characteristics at higher voltages.

With the simplified model it is possible to analyze the differences that arise for EL and EM-PL imaging. First the EM-PL case is analyzed under open circuit conditions (sample under illumination). No current flows at the contacts, and as the current sources and diodes (Number 1 and 2) are assumed to be equal also no current flows through the series resistance. When the short circuit current generated by the two current sources combined is $I_{\rm sc}$ than each current source generates a current of $I_{\rm sc}/2$, which flows through their respective diodes. The (junction) voltages across the diodes are consequently the same and equal to the $V_{\rm oc}$ of the entire equivalent circuit

$$V_{\rm j,1} = V_{\rm j,2} = V_{\rm oc} = \log\left(\frac{I_{\rm sc}}{2I_0} + 1\right) \frac{kT}{e}.$$
 (5.1)

Of course it follows that the average of $V_{j,1}$ and $V_{j,2}$ is equal to V_{oc} , which is used for the experiments and seen in the simulations.

The EM-PL junction voltage is compared to the EL junction voltage at the same amounts of injected current, i.e. current recombining in the solar cell. Thus, the situation under illumination at open circuit needs to be compared to a situation where the current sources generate no current and an external voltage is applied so that the total current through the model is equal to $I_{\rm sc}$. However, the currents through the two diodes (I_1,I_2) are not the same anymore. It holds for them

$$I_{\rm sc} = I_1 + I_2 \tag{5.2}$$

and

$$\frac{I_1}{I_2} = \frac{R_s + R_{j,2}}{R_{i,1}}. (5.3)$$

Here, $R_{\rm s}$ denotes the series resistance in series to diode 2 and $R_{\rm j,1,2}$ denotes the resistance of the diodes (junctions). From these conditions the current through the diodes can be defined in terms of the injected current $I_{\rm sc}$

$$I_{1} = \frac{\left(\frac{R_{s} + R_{j,2}}{R_{j,1}}\right) I_{sc}}{\left(\frac{R_{s} + R_{j,2}}{R_{j,1}} + 1\right)}$$
(5.4a)

$$I_2 = \frac{I_{\rm sc}}{\left(\frac{R_{\rm s} + R_{\rm j,2}}{R_{\rm j,1}} + 1\right)}.$$
 (5.4b)

The junction voltages across the diodes are given by

$$V_{\rm j,1,2} = \log\left(\frac{I_{1,2}}{I_0} + 1\right) \frac{kT}{e} \tag{5.5}$$

and consequently the average junction voltage of the cell $V_{i,\mathrm{EL}}$ is

$$V_{\rm j,EL} = \log \left(\frac{\left(\frac{R_{\rm s} + R_{\rm j,2}}{R_{\rm j,1}}\right) I_{\rm sc}^2}{\left(\frac{R_{\rm s} + R_{\rm j,2}}{R_{\rm j,1}} + 1\right)^2 I_0^2} \right) \frac{kT}{2e}$$
 (5.6)

For the last equation it was assumed that $I_{1,2}/I_0$ is so large that the +1 can be ignored in Equation 5.5. Due to the series resistance I_2 is smaller than I_1 , which also leads to $R_{j,2}$ being larger than $R_{j,1}$. Thus, by comparing Equation 5.6 to Equation 5.1 it can now be seen that the resistance $R_{\rm s}$ will cause $V_{\rm j,EL}$ to be lower than the $V_{\rm oc}$ of the sample for the same injected current. This is a simplified illustration of the effects seen in the measurements and the simulations. Equation 5.6 also explains why the effect is only visible at higher injected currents. At lower

injected currents the resistance of the diodes $R_{\rm j}$ is so large that it will decrease the influence $R_{\rm s}$ has on the measurement result.

That $V_{\rm j,EL}$ is lower than $V_{\rm oc}$ in the above calculation results from the fact that the local junction voltage depends logarithmic on the local current. By taking the simple average of all local junction voltages and therefore considering all to be equally important for the global junction voltage, we underestimate the influence higher voltages have on the current flow. These areas are more important for the voltage measured at the terminals of the cell as they carry more current. If the diodes in the model described by Figure 5.9 would be replaced by ohmic resistors $R_{\rm ohm}$, making the local junction voltage linearly dependent on the current flow, $V_{\rm j,EL}$ would become equal to $V_{\rm oc}$. This can be easily seen by calculating $V_{\rm j,EL}$ using $V_{\rm j,1,2} = I_{1,2}/R_{\rm ohm}$. Thus, an increase in the difference in local current densities (at large voltages in the dark or at low voltages under illumination), increases the role the non-linear dependence of the junction voltage on the current plays and increases the error resulting from the use of the average of the local junction voltages as the overall cell junction voltage.

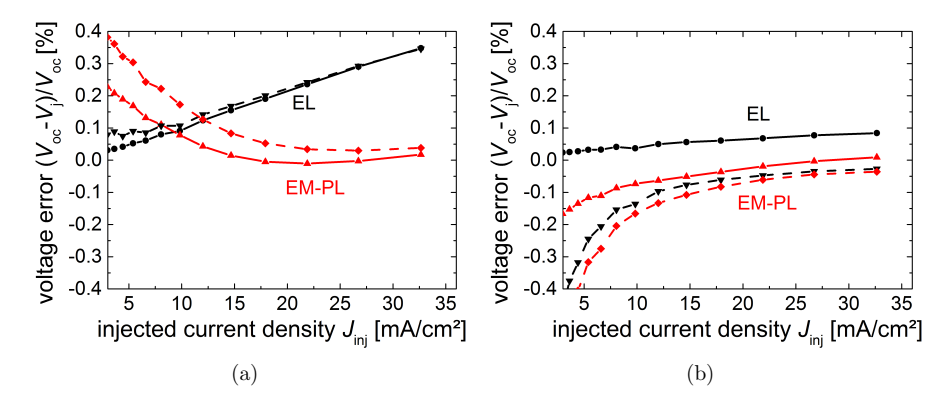


Figure 5.10.: (a) Difference of the cell junction voltage determined via the average of the simulated local cell junction voltages of a non-defected cell (second from the left, solid lines) and a defected cell (8th from the left, dashed lines) to the open circuit voltage of the corresponding cell at different injected current densities. (b) Difference of the cell junction voltage determined via the average of the simulated luminescence intensity of a non-defected cell (second from the left, solid lines) and a defected cell (8th from the left, dashed lines) to the open circuit voltage of the corresponding cell at different injected current densities.

Figure 5.10 (a) shows the relative difference of the junction voltage average determined for a non-defected cell (eg. Figure 5.2, second from the left) and a defected cell (8th from the left) to the open circuit voltage of the corresponding cell at the same amount of injected current. This difference increases for the EL

measurements for both cells continuously to higher injected currents as the series resistance leads continuously to larger differences in the local current flow. The difference of $V_{\rm oc}$ to the EM-PL $V_{\rm j}$ is zero for the non-defected cell when it is under open circuit conditions during the determination of the EM-PL characteristic but increases at different conditions, due to the increasing impact of the series resistance and the resulting differences in the local current flow. For the shunted cell there is also difference between the EM-PL junction voltage and $V_{\rm oc}$ when the sample is under open circuit conditions, as the shunt leads to varying currents across the diodes in the cell, although the net current through the cell is zero.

An idea to reduce the error seen in Figure 5.10 (a) would be to calculate first the average of the luminescence intensity for each cell and calculate from that value the cell junction voltage. As long as the luminescence intensity relates closer to the dependence of the local current to the junction voltage, this should reduce the error between the cell $J/V_{\rm j}$ characteristic and its $J_{\rm sc}/V_{\rm oc}$ characteristic. In Figure 5.10 (b) the difference between the $J/V_{\rm j}$ of the cells determined in such a way to the $J_{\rm sc}/V_{\rm oc}$ is shown. The error for the EL characteristic could be significantly reduced for the non-defected cell. However, the EM-PL characteristics of both cells and the EL characteristic of the shunted cell show now a larger error. In these cases the error is not reduced to zero, as the local current depends via a two diode model on the junction voltage, while for the calculation of the luminescence intensity from the junction voltage a simple exponential function with ideality factor of 1 was assumed (Equation 3.3). Furthermore, the shunt shows ohmic behavior, and therefore the dependence of the local current on the junction voltage is linear and not exponential as in the rest of the cell.

5.3. Conclusion

In this section it was demonstrated how $J/V_{\rm j}$ characteristics of individual cells already connected to a CIGS solar module can be determined. These characteristics are equal to the $J_{\rm sc}/V_{\rm oc}$ characteristics of the individual cell, when determined for simplified models using the one- or two-diode model. Therefore, they can be used to determine the dark saturation current of a cell as well as possible shunt strengths.

However, in contrast to the simplified models, it was found that the measured $J/V_{\rm j}$ characteristics can differ slightly from $J_{\rm sc}/V_{\rm oc}$ characteristics. Especially the EL characteristics show lower voltages at higher injected currents than the $J_{\rm sc}/V_{\rm oc}$ characteristics. Simulations showed that such deviations arise from the determination procedure of the $J/V_{\rm j}$ characteristics. Using the average of the local junction voltages of each cells as the overall cell junction voltage is not completely correct as it does not consider the exponential dependence of the local current on the junction voltage. A possible correction for the error can be achieved by taking the average of the luminescence intensity when calculating the cell junction

voltage. This worked well for the EL characteristics of cells without a shunt, but the procedure will also exhibit an error when shunts exists in a cell, where the local current depends linearly on the local junction voltage. Thus, the best evaluation method depends on the available data (if EL or EM-PL are used and the voltage region) as well as the sample properties itself (if the current dependence on the local junction voltage can be estimated).

Additionally, the experimentally determined EL and EM-PL characteristics differ from each other at low injected currents. The effect is larger for shunted cells. This effect could not be reproduced to its visible extent in the PVMOS simulations. Therefore the effect cannot be described in an one or two diode equivalent circuit network but rather results from an injection dependent series resistance. At the origin and influence of a possible injection dependent series resistance is taken a closer look in Chapter 7.

6. Photocurrent Collection Efficiency Imaging

A large portion of this work focuses on the use of the local photocurrent collection efficiency as a characterization quantity for solar cells. The method makes the influence of defects and local properties quantifiable with a simple set of luminescence measurements. The chapter begins by introducing the local differential photocurrent collection as it was defined by Wong et al. [29] and its interpretation and behavior is extensively discussed. Subsequently, the method is further developed to yield the local total photocurrent collection and its potential to provide spatially resolved information about the net power provided is discussed. The imaging methods are demonstrated experimentally and via PVMOS simulations on c-Si solar cells and CIGS solar cells and modules. The respective applicability to each sample system is discussed in detail. Parts of the results in this chapter were published in [102] and [104].

6.1. Theory

This section discusses in detail the theoretical concepts behind photocurrent collection efficiency measurements. The meaning of the differential photocurrent collection efficiency on a local (e.g. for a pixel) and global (e.g. for a complete sample) scale is discussed. Additionally, it will be shown how the size of the photocurrent collection efficiency is linked to physical properties of a solar cell and how it depends on the operating point for which it is measured. Furthermore, the differential photocurrent collection efficiency is extended to provide information about the total collected photocurrent and even net local power output.

6.1.1. The Differential Photocurrent Collection Efficiency

Definitions

The local differential photocurrent collection efficiency was first introduced by Wong et al. [29, 30] who refers to it with the term current transport efficiency. In later work Rau et al. [105] used the term photocurrent collection efficiency. It is important to note that the photocurrent collection efficiency can be defined on a local, as well on a global scale, which makes further differentiation necessary.

Additionally, the original photocurrent collection efficiency is a differential value, but in this work it is shown that the differential value can also be integrated. For clarity the original current transport efficiency defined by Wong is called from now on *local differential* photocurrent collection efficiency $f_{\rm pc,loc}$. Whether a property is meant to be global or local will be designated by the subscript *loc* or *glob*.

The local differential photocurrent collection efficiency $f_{pc,loc}$ is defined as

$$f_{\text{pc,loc}}(\boldsymbol{r}, j_{\text{ph}}(\boldsymbol{r}), V_{\text{ext}}) = \left. \frac{dj_{\text{coll,loc}}(\boldsymbol{r}, j_{\text{ph}}(\boldsymbol{r}), V_{\text{ext}})}{dj_{\text{ph}}(\boldsymbol{r})} \right|_{dV_{\text{ext}} = 0}.$$
 (6.1)

The quantity $f_{\rm pc,loc}$ describes the locally collected current density $j_{\rm coll,loc}$, i.e. the current density that flows from a specific region r to the terminals of the device, differentiated with respect to the photocurrent density $j_{\rm ph}$ generated at position r while the external voltage $V_{\rm ext}$ is constant. Figure 6.1 visualizes the concept, showing how the photocurrent density $j_{\rm ph}$ generated at one point in a solar cell is not completely collected at the terminals as current is lost due to recombination current $dj_{\rm rec}$ within the solar cell.

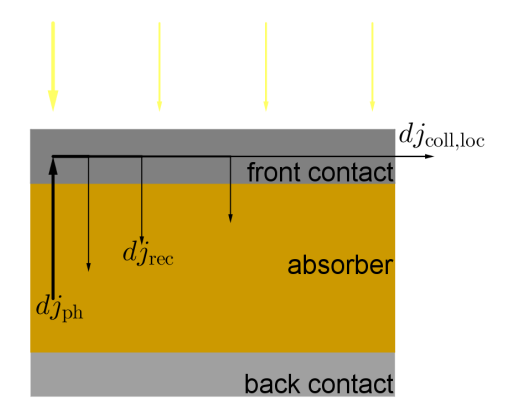


Figure 6.1.: Sketch visualizing the current densities relevant for the local differential photocurrent collection efficiency. A small local illumination change results in a local photocurrent density change $dj_{\rm ph}$. Only parts of this current density are collected at the terminals of the device as other parts recombine within the solar cell $(dj_{\rm rec})$. The ratio of the collected current density $dj_{\rm coll,loc}$ to the original photocurrent change is given by $f_{\rm pc,loc}$.

Figure 6.2 sketches the variables relevant for the global photocurrent collection efficiency. The global photocurrent collection efficiency is given by the global total collected photocurrent $I_{\rm coll,glob}$ differentiated with respect to the short circuit current. The global total collected photocurrent is linked to the electrical characteristics of solar devices via the difference of its dark and illuminated I/V-characteristic

$$I_{\text{coll,glob}}(V_{\text{ext}}, I_{\text{sc}}) = I(V_{\text{ext}}, I'_{\text{sc}} = 0) - I(V_{\text{ext}}, I_{\text{sc}}).$$
 (6.2)

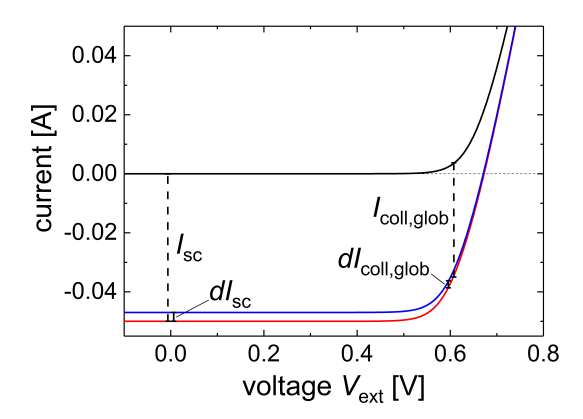


Figure 6.2.: Sketch showing the definition of the differential and total global collected photocurrent. The total global collected photocurrent $I_{\rm coll,glob}$ is given by the difference of the light and dark I/V-characteristic of a solar device and the differential global collected photocurrent $dI_{\rm coll,glob}$ is given by the infinitesimal change of the current at a certain forward voltage resulting from a infinitesimal change of the short circuit current $I_{\rm sc}$.

The quantity $dj_{\text{coll,loc}}$ integrated across the whole sample area yields the global differential collected photocurrent $dI_{\text{coll,glob}}$. By assuming furthermore that $f_{\text{pc,loc}} = 1$ everywhere at $V_{\text{ext}} = 0 \, \text{V}$ and that dj_{ph} is also position independent (position independent quantum efficiency), it follows that $dj_{\text{ph}} = dI_{\text{sc}}/A$ at every position of the sample and we obtain the global differential photocurrent collection efficiency $f_{\text{pc,glob}}$ by averaging $f_{\text{pc,loc}}$ over the entire sample area

$$f_{\rm pc,glob}(V_{\rm ext}, I_{\rm sc}) = \frac{dI_{\rm coll,glob}(V_{\rm ext}, I_{\rm sc})}{dI_{\rm sc}} = \frac{1}{A} \int \int f_{\rm pc,loc}(\boldsymbol{r}, V_{\rm ext}, I_{\rm sc}) dA. \tag{6.3}$$

Measurement Procedure

It was shown by Wong et al. [29] with the help of the Lorentz reciprocity theorem [106] that the local differential photocurrent collection efficiency in an interconnected linearized equivalent circuit is equal to the local junction voltage differentiated with respect to the external voltage when the generated photocurrent is held constant

$$f_{\text{pc,loc}}(\boldsymbol{r}, j_{\text{ph}}(\boldsymbol{r}), V_{\text{ext}}) = \frac{dj_{\text{coll,loc}}(\boldsymbol{r}, j_{\text{ph}}(\boldsymbol{r}), V_{\text{ext}})}{dj_{\text{ph}}(\boldsymbol{r})} \bigg|_{dV_{\text{ext}} = 0}$$

$$= \frac{dV_{\text{j}}(\boldsymbol{r}, j_{\text{ph}}(\boldsymbol{r}), V_{\text{ext}})}{dV_{\text{ext}}} \bigg|_{dj_{\text{ph}} = 0}.$$
(6.4)

This relation is useful as the local junction voltage is measurable from the luminescence signal of solar cells, which enables the imaging of $f_{\rm pc,loc}$. For that two images $(S_{\rm cam,1} \text{ and } S_{\rm cam,2})$ are needed that are taken at small voltage values $(\delta V_{\rm ext}/2)$ above and below a chosen operating point $V_{\rm ext}$. From these images and an additional background image $S_{\rm cam,bg}$, $f_{\rm pc,loc}$ can be calculated using the following formula (cf. Equation 3.4 and 6.4)

$$f_{\text{pc,loc}}(\boldsymbol{r}, j_{\text{ph}}(\boldsymbol{r}), V_{\text{ext}}) = \ln \left(\frac{S_{\text{cam},1} - S_{\text{cam},\text{bg}}}{S_{\text{cam},2} - S_{\text{cam},\text{bg}}} \right) \frac{V_{\text{th}}}{\delta V_{\text{ext}}}.$$
 (6.5)

Note, that no open circuit voltage measurement is needed to calibrate the images as the calibrations constant in Equation 3.4 is eliminated in the $f_{\rm pc,loc}$ calculations.

In [105] it was shown that it is also possible to calculate $f_{pc,loc}$ from luminescence images directly instead of determining a junction voltage image from the luminescence images and then using these to determine the $f_{pc,loc}$ image (which is essentially done in Equation 6.5). The equation for the direct calculation reads

$$f'_{\text{pc,loc}}(\boldsymbol{r}, j_{\text{ph}}(\boldsymbol{r}), V_{\text{ext}}) = \frac{\delta S_{\text{cam}}(\boldsymbol{r}, j_{\text{ph}}(\boldsymbol{r}), V_{\text{ext}})}{\Delta S_{\text{cam}}(\boldsymbol{r}, j_{\text{ph}}(\boldsymbol{r}), V_{\text{ext}})} \frac{V_{\text{th}}}{\delta V_{\text{ext}}}.$$
 (6.6)

Here, $\delta S_{\rm cam}$ is the difference between two luminescence images taken at $\delta V_{\rm ext}/2$ above and below $V_{\rm ext}$ and $\Delta S_{\rm cam}$ is the difference between a luminescence image determined at a voltage equal to $V_{\rm ext}$ and the sample at short circuit conditions. This calculation procedure seems to be slightly more straight forward than the original one (cf. Equation 6.5), as it does not need a logarithm calculation of the luminescence images. However, it should be remembered that Equation 6.6 is based on a linear approximation and therefore only holds if $\delta V_{\rm ext}$ is sufficiently small. We can derive how small $\delta V_{\rm ext}$ should be chosen. With Equation 3.3 we obtain for $\delta S_{\rm cam}$

$$\begin{split} \delta S_{\text{cam}} &= S_{\text{cam}} \left(V_{\text{j}} \left(V_{\text{ext}}' = V_{\text{ext}} + 1/2 \ \delta V_{\text{ext}} \right) \right) - S_{\text{cam}} \left(V_{\text{j}} \left(V_{\text{ext}}' = V_{\text{ext}} - 1/2 \ \delta V_{\text{ext}} \right) \right) \\ &= \Delta S_{\text{cam}} \left(V_{\text{j}} \left(V_{\text{ext}} \right) \right) \times 2 \sinh \left(\frac{\delta V_{\text{j}} (\delta V_{\text{ext}})}{2 \ V_{\text{th}}} \right) \\ &\approx \Delta S_{\text{cam}} \left(V_{\text{j}} \left(V_{\text{ext}} \right) \right) \left(\frac{\delta V_{\text{j}}}{V_{\text{th}}} + \frac{\delta V_{\text{j}}^{3}}{24 \ V_{\text{th}}^{3}} \right). \end{split} \tag{6.7}$$

In the third step of Equation 6.7 the first and second order of the taylor expansion of the hyperbolic sine was used. By ignoring the second order, Equation 6.6 can be derived. However, if we include the second order we will find that

$$f'_{\rm pc,loc} = f_{\rm pc,loc} \left(1 + \frac{f_{\rm pc,loc}^2 \delta V_{\rm ext}^2}{24 V_{\rm th}^2} \right).$$
 (6.8)

Thus, the approximation only holds if $f_{\rm pc,loc}^2 \delta V_{\rm ext}^2/24 \ V_{\rm th}^2$ is much smaller than 1. For example, leads a $\delta V_{\rm ext}$ of 0.02 V to an error of less than 2.5 %, if $f_{\rm pc,loc}$ is about one.

For further discussion it is referred to the determination method via Equation 6.6 as the lin-method, due to the linear approximation used and the determination method based on Equation 6.4 and 6.5 will be called the log-method, as a logarithm is used to determine the junction voltage images.

To verify the obtained $f_{\rm pc,loc}$ images we make use of Equation 6.3, as it allows the comparison of $f_{\rm pc,loc}$ values obtained from luminescence images using Equation 6.4 with results that can be determined independently via electrical measurements: The second term in Equation 6.3 is determined by slightly altering the illumination of a sample and measuring the respective responses in short circuit and global collected photocurrent at a desired forward voltage. The third term of Equation 6.3 is calculated from the $f_{\rm pc,loc}$ image. When both results are equal, the $f_{\rm pc,loc}$ imaging works as expected. This procedure to verify $f_{\rm pc,loc}$ images was developed simultaneously to this work in [107] and used for the verification of $f_{\rm pc,loc}$ images of p-i-n GaAs solar cells.

Influence of Solar Cell Parameters

The magnitude of $f_{\rm pc,loc}$ is influenced by the different differential resistances within the solar cell, which govern recombination and transport to the terminals of the device. This property of $f_{\rm pc,loc}$ is explained with the help of a linearized one-diode equivalent circuit depicted in Figure 6.3. In this circuit the diode and the shunt are combined into one linear junction resistance $r_{\rm j}$, the series resistance is denoted with $r_{\rm s}$ and a constant external voltage acts as a short circuit at the contacts

The photocurrent generated in parallel to the junction resistance has two possible options. The photocurrent will either flow across the terminals of the device across the differential series resistance $r_{\rm s}$ and contribute to the external current or it stays within the solar cell and flows there across the differential junction resistance $r_{\rm i}$.

The relation between the two currents $I_{\rm rs}$ across $r_{\rm s}$ and $I_{\rm rj}$ across $r_{\rm j}$ is given by Kirchhoff's circuit laws and therefore depends on the resistances of the two possible paths

$$\frac{I_{\rm rs}}{I_{\rm ri}} = \frac{r_{\rm j}}{r_{\rm s}} \tag{6.9}$$

and it follows for the $f_{pc,loc}$

$$f_{\rm pc,loc} = \frac{I_{\rm rs}}{I_{\rm rj} + I_{\rm rs}} = \frac{r_{\rm j}}{r_{\rm j} + r_{\rm s}}.$$
 (6.10)

The quantity $r_{\rm s}$ includes the different contact and transport resistances and is in the one diode equivalent circuit assumed to be voltage independent. The quantity

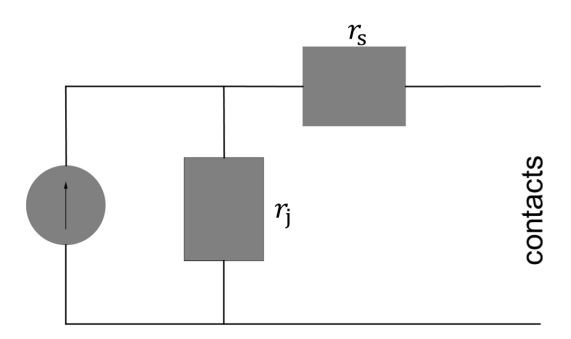


Figure 6.3.: Simplified equivalent circuit used to describes the important properties of a solar cell that influence $f_{\rm pc,loc}$. The photocurrent will either flow through the contacts across the series resistance $r_{\rm s}$ or recombine within the solar cell across the junction resistance $r_{\rm j}$.

 $r_{\rm j}$ is the resistance of the diode and a shunt in parallel. The differential resistance $r_{\rm j}$ is strongly voltage dependent, as it includes properties of a diode, and therefore, $f_{\rm pc,loc}$ is also voltage dependent. As the junction resistance $r_{\rm j}$ is usually very large at low voltages, $f_{\rm pc,loc}$ typically starts at low voltages with a value of 1 and decreases as soon as the junction resistance decreases to the order of magnitude of the series resistance, due to an increasing voltage.

Figure 6.4 shows the influence of different parameters on $f_{\rm pc,loc}$ in detail, where $f_{\rm pc,loc}$ was calculated for a simple one diode model with varying parameters (the corresponding J/V-characteristics are shown in Figure 2.6). An increase of the series resistance $R_{\rm s}$ and the dark saturation current J_0 always leads to a decrease of $f_{\rm pc,loc}$. This is expected from Equation 6.10. An increase of the short circuit current density $J_{\rm sc}$ also leads to a decrease of $f_{\rm pc,loc}$. Due to the series resistance, a higher $J_{\rm sc}$ increases the voltage drop across the junction (at a constant external voltage) and decreases therefore also the junction resistance $r_{\rm j}$. A decrease of the shunt resistance $R_{\rm p}$ on the other hand only decreases $f_{\rm pc,loc}$ at low voltages and increases it at higher voltages. A shunt may increase $r_{\rm j}$ at certain external voltages due to a lower voltage drop across $r_{\rm j}$ and a resulting higher resistance of the diode. This happens as $r_{\rm j}$ is also in series with $r_{\rm s}$ and the external voltage is divided up between them. However, at lower external voltages a shunt usually lowers the $r_{\rm j}$ and therefore decreases $f_{\rm pc,loc}$ in this regime.

Additionally, it is important to note that at the open circuit voltage the photocurrent collection efficiency is not zero. Even if the net current flow through a sample is zero at a fixed voltage $V_{\rm ext}=V_{\rm oc}$, the current still changes if the illumination of the solar cell is changed and the voltage stays fixed.

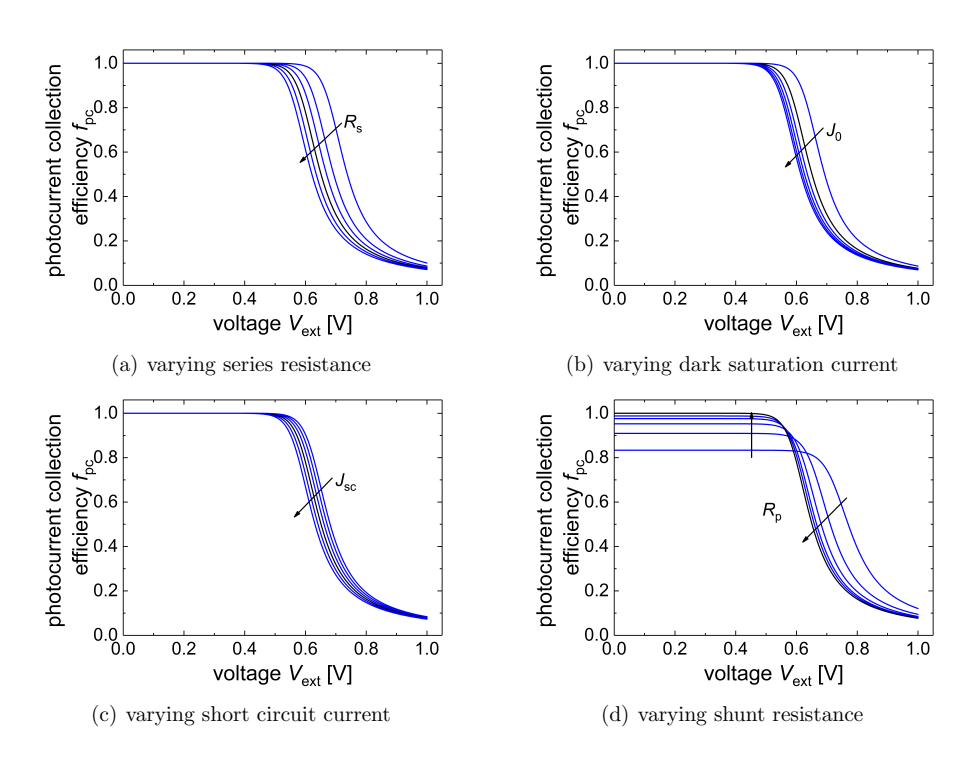


Figure 6.4.: Influence of various parameters on the voltage dependence of $f_{\rm pc,loc}.$ The arrows show in the direction of increasing parameters (a) $R_{\rm s}=0.1-1.6\,\Omega{\rm cm}^2$ in $0.3\,\Omega{\rm cm}^2$ steps. (b) $J_0=0.5-10.5\times10^{-13}\,{\rm A/cm}^2$ in $2\times10^{-13}\,{\rm A/cm}^2$ steps. (c) $J_{\rm sc}=0-0.05\,{\rm A/cm}^2$ in $0.05\,{\rm A/cm}^2$ steps. (d) $R_{\rm p}=5,10,20,40,80,10^{10}\,\Omega{\rm cm}^2.$ Baseline shown in black. Parameters: $R_{\rm s}=1\,\Omega{\rm cm}^2,\ J_0=2.5\times10^{-13}\,{\rm A/cm}^2,\ J_{\rm sc}=0.03\,{\rm A/cm}^2,\ R_{\rm p}=10^{10}\,\Omega{\rm cm}^2.$ The corresponding J/V-characteristics are shown in Figure 2.6.

Noise

The images of the luminescence radiation taken by the camera are subject to noise. An image contains a discrete number of counts X for every pixel and this number of counts is assumed to be Poisson-distributed, which converges for large X to normal distributed. This means that the error or noise, σ_X , is equal to \sqrt{X} [108]. Thus, the relative error, σ_X/X , decreases with X. As X increases with the integration time of the camera, longer integration times yields images less affected by noise. However, an arbitrary increase of the integration time is not always possible. Thus, especially at low voltages where the luminescence signal is low, noise has a significant influence on the measurement results. Furthermore, due to the calculation procedure used to determine $f_{\rm pc,loc}$ from luminescence images (cf. Equation 6.5 or 6.6) the relative noise will increase. Therefore, it might be that individual luminescence images are not very noisy, but the resulting $f_{\rm pc,loc}$ image is noisy.

In the following it is discussed how noise alters $f_{\rm pc,loc}$ imaging results. With increasing noise the image subtractions result more often in negative values and zeros (when they should be positive if no noise is present) that leads to nonphysical or non-defined $f_{\rm pc,loc}$ values. When that happens $f_{\rm pc,loc}$ was set to zero to be able to calculate an image average value. Therefore, the $f_{\rm pc,glob}$ for a complete cell determined from the images is biased towards zero at low voltages, where noise is unavoidable. The effect is reproduced in Section 6.4.2, where noise is added to simulation results.

To quantify the influence of noise on the measurement result, the error on the original luminescence images (estimated by assuming a normal distribution) is propagated to the final $f_{\rm pc,loc}$ value via the Gaussian error propagation law [109]. With Equation 6.5 we obtain for the error of $f_{\rm pc,loc}$ (cf. Appendix A)

$$\sigma f_{\text{pc,loc}} = \sqrt{\left(\frac{\sqrt{S_{\text{cam},1} + S_{\text{cam},\text{bg}}}}{S_{\text{cam},1} - S_{\text{cam},\text{bg}}}\right)^2 + \left(\frac{\sqrt{S_{\text{cam},2} + S_{\text{cam},\text{bg}}}}{S_{\text{cam},2} - S_{\text{cam},\text{bg}}}\right)^2} \frac{V_{\text{th}}}{\delta V_{\text{ext}}}$$
(6.11)

To estimate the error on $f_{\text{pc,glob}}$ the average of every error value $\sigma f_{\text{pc,loc}}$ for each pixel included in $f_{\text{pc,glob}}$ is taken.

6.1.2. The Total Photocurrent Collection Efficiency

Under real operating conditions the whole solar cell turns from an operating point where it is complete in the dark to an operating where the whole cell area is illuminated, meaning that not only a local photocurrent density is changed by a large amount, but additionally the local photocurrent density is changed across the whole sample. To know how much of the locally generated photocurrent is actually collected at the terminals of the device under these conditions, the differential

photocurrent collection efficiency is not sufficient. Therefore, we define the total local photocurrent collection efficiency $F_{\rm pc,loc}$ as the photocurrent density collected from a certain area $j_{\rm coll,loc}$ divided by the locally generated photocurrent

$$F_{\text{pc,loc}}(V_{\text{ext}}, j_{\text{ph}}, \mathbf{r}) = \frac{j_{\text{coll,loc}}(V_{\text{ext}}, j_{\text{ph}}, \mathbf{r})}{j_{\text{ph}}(\mathbf{r})}.$$
(6.12)

To determine $F_{\rm pc,loc}$ we need to know the total current density change $j_{\rm coll,loc}$ originating from a region r due to the generated photocurrent changing on the whole sample. We obtain $j_{\rm coll,loc}$ by integrating Equation 6.4 from 0 to $j_{\rm ph}$

$$j_{\text{coll,loc}}\left(V_{\text{ext}}, j_{\text{ph}}, \boldsymbol{r}\right) = \int_{0}^{j_{\text{ph}}} f_{\text{pc,loc}}\left(V_{\text{ext}}, j'_{\text{ph}}, \boldsymbol{r}\right) dj'_{\text{ph}}.$$
 (6.13)

By using again the assumption that the differential photocurrent collection efficiency is one at zero $V_{\rm ext}$ and that the quantum efficiency of the device is position independent it follows that the short circuit current density is equal to locally generated photocurrent density. Thus, by using $j_{\rm ph}=J_{\rm sc}$ we obtain the following calculation principle for $F_{\rm pc,loc}$

$$F_{\rm pc,loc}(V_{\rm ext}, J_{\rm sc}, \mathbf{r}) = \frac{1}{J_{\rm sc}} \int_0^{J_{\rm sc}} f_{\rm pc,loc}(V_{\rm ext}, J'_{\rm sc}, \mathbf{r}) \, dJ'_{\rm sc}. \tag{6.14}$$

In words the equation means that for an experimental determination of $F_{\rm pc,loc}$, we have to determine $f_{\rm pc,loc}$ at several illumination steps, then multiply the images with their respective short circuit current density changes between the steps and finally divide by the total short circuit current density measured at the illumination condition that we are interested in. It is also for the total photocurrent collection efficiency possible to determine from the local values a global value (cf. Equation 6.3)

$$F_{\rm pc,glob}\left(V_{\rm ext},I_{\rm sc}\right) = \frac{I_{\rm coll,glob}\left(V_{\rm ext},I_{\rm sc}\right)}{I_{\rm sc}} = \frac{1}{A} \int \int F_{\rm pc,loc}\left(V_{\rm ext},I_{\rm sc},\boldsymbol{r}\right) dA. \quad (6.15)$$

As discussed $I_{\text{coll,glob}}$ is the difference between an illuminated and a dark I/V characteristic at a certain voltage (cf. Equation 6.2). Thus, in contrast to the differential photocurrent collection efficiency the total photocurrent collection is closely connected to the actual electrical characteristics of a solar cell and an image of it allows to establish a quantitative relation between photocurrent collection losses and their local origin on the sample.

6.1.3. From Collected Photocurrent to Collected Power and Net Power

In this Section we explore how the photocurrent collection efficiency image is connected to an image showing the power provided by solar cells. To this end we divide the net power output of a sample into two parts (cf. Figure 6.5). The first part, the 'collected power' CP would be given by the amount of collected photocurrent at a certain voltage. The second part, the 'dissipated power' DP of a solar cell is determined by the current flow through a solar cell in the dark.

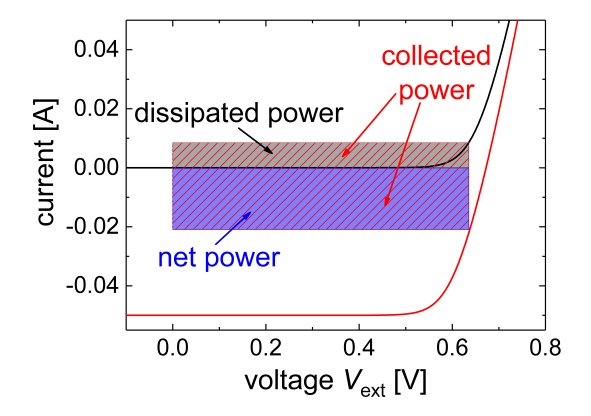


Figure 6.5.: Sketch demonstrating how the net power output of a solar cell is defined by its dissipated power (grey square) and its collected power (red patterned square). By subtracting the dissipated power from the collected power the net power provided by a solar cell is obtained (blue square).

As discussed in Section 6.1.2 a $F_{\rm pc,loc}$ image is linked via Equation 6.15 to the difference between the dark and illuminated I/V characteristic of a sample at a certain voltage, the collected photocurrent $I_{\rm coll,glob}$. A collected power image CP, which shows the power collected from each region of the solar cell, is obtained by multiplying an $j_{\rm coll,loc}$ image with the external voltage for which it was taken. It follows

$$CP = j_{\text{coll,loc}} \times V_{\text{ext}} = F_{\text{pc,loc}} \times J_{\text{sc}} \times V_{\text{ext}}.$$
 (6.16)

A CP image does not describe the perfomance of a region, because the power dissipated in the region is not yet taken into account. For example, if we consider a severe shunt where no charge carrier are generated or collected from, the region yields a $F_{\rm pc,loc}$ value of zero, but for the local performance it is important that we also consider that current is driven through the shunt by the external voltage actually resulting in not only no power gained from the region but also power lost. Thus, an additional image is needed which corresponds in its sum to the external current at a certain voltage in the dark, so that we can obtain an image of the dissipated power DP from it.

In experiments it is not possible to determine a DP image without further assumptions. Thermography images are only suitable to a limited extent [110]. The power image obtained from thermography imaging includes the power dissipated in the contacts of a solar cell and in the junction, while the DP image is defined so

that the locally dissipated power is only given by the current through the junction and the external voltage. Thus, it is only possible to use thermography images to determine a dissipated power image if it can be assumed that most of the external voltage drops across the z-direction of the solar cell and not other series resistances. However, with simulations it is possible to determine a DP image by multiplying an image of the current flow in the dark in the z-direction through the cell with the respective voltage for which it was calculated. The sum over this current flow everywhere in the sample results in the total current flow through the sample at a certain voltage, because there is no current generated in the solar cell in the dark and therefore no current is able to flow in circles in the solar cell. Therefore, multiplying the image of the current flow with the external voltage results in an image that corresponds with its sum to the total power dissipated by the solar cell.

If determined correctly, the 'dissipated power' image subtracted from the 'collected power' image yields a 'net power' image describing the actual performance of a certain region (cf. Figure 6.5)

$$NP = CP - DP. (6.17)$$

The integral across the net power image is then by definition equal to the power output of a solar cell also given by its I/V characteristic

$$P(V_{\text{ext}}, I_{\text{sc}}) = I_{\text{ext}}(V_{\text{ext}}, I_{\text{sc}}) \times V_{\text{ext}} = \int \int NP(V_{\text{ext}}, I_{\text{sc}}, \boldsymbol{r}) dA.$$
 (6.18)

6.2. Crystalline Silicon Solar Cells

The experimental demonstration of the differential and total photocurrent collection efficiency imaging methods are begun by looking at mono-crystalline silicon solar cells. As luminescence imaging is a well established method for mono-crystalline cells such a solar cell is used to verify the photocurrent collection efficiency imaging methods on a global scale, experimentally. Furthermore, this section includes PVMOS simulations of crystalline silicon solar cells that verify differential photocurrent collection efficiency images on a local scale and demonstrate the influence of several local properties on the total photocurrent collection efficiency and net power images.

6.2.1. Experimental Results

The Differential Photocurrent Collection Efficiency

The crystalline silicon solar cell described in Section 3.1.4 was used for the first photocurrent collection efficiency measurements. The sample exhibits several

cracks. Therefore, it is expected to see local features. An electro-modulated photoluminescence image for $V_{\rm ext}$ =0.45 V close to the maximum power point of the sample is shown in Figure 6.6. The EM-PL image shows several regions where the luminescence intensity is higher than in other areas and therefore the local junction voltage is increased. These effects mainly arise from the cracks in the sample which lead to broken fingers and high transport resistance towards the bus-bars.

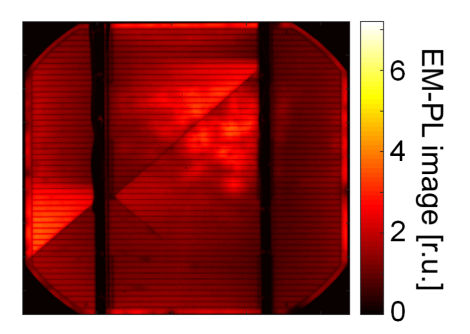


Figure 6.6.: EM-PL Image of a $12.5 \times 12.5 \,\mathrm{cm}^2$ c-Si Cell determined at $V_{\mathrm{ext}} = 0.45 \,\mathrm{V}$. For the laser intensity at which the image was taken the samples V_{oc} was approximately $0.6 \,\mathrm{V}$ and J_{sc} approximately $32 \,\mathrm{mA/cm}^2$, which is close the respective values under standard test conditions ($V_{\mathrm{oc}} = 0.6 \,\mathrm{V}, J_{\mathrm{sc}} = 32.7 \,\mathrm{mA/cm}^2$).

Figure 6.7 shows the $f_{\rm pc,loc}$ images, determined with $\delta V_{\rm ext}$ =0.02 V at $V_{\rm ext}$ =0.45 V for different illumination intensities. Thus, the luminescence images used to calculate $f_{\rm pc,loc}$ were taken at an applied voltage of 0.44 V and 0.46 V. The cracks and defects seen in the EM-PL image are visible again and additionally the image quantifies their influence on the photocurrent collection. Furthermore, we see how an increase of illumination leads to reduction in the photocurrent collection efficiency, as expected (cf. Section 6.1.1).

To verify the measurement results Equation 6.3 is used. Thus, $f_{\rm pc,glob}$ was determined in two ways: First electrically by varying the illumination slightly and measuring for both illumination states $I_{\rm coll,glob}$ and $I_{\rm sc}$ and second via imaging of $f_{\rm pc,loc}$ and taking the average over the samples active area. Figure 6.8 shows the results for four different voltage points and three different illumination intensities. Both measurement overlap well proving that the Wong-Green Theorem [29] for the determination of the local differential photocurrent collection efficiency is working well.

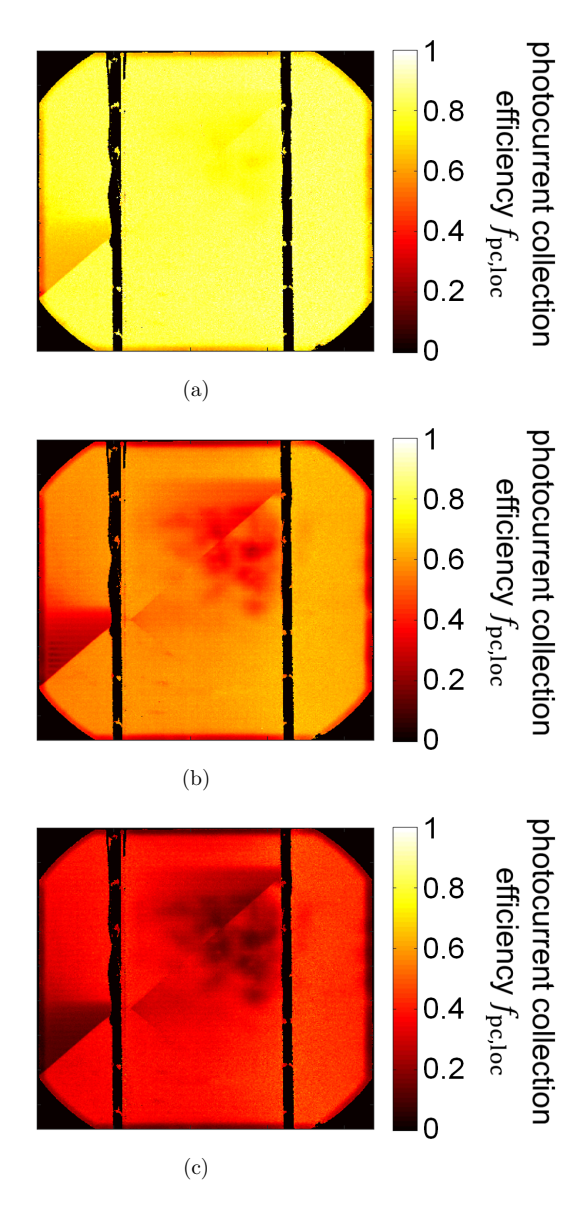


Figure 6.7.: Differential photocurrent collection efficiecy images of a c-Si solar cell taken under different illumination conditions with $V_{\rm ext}$ =0.45 V. (a) $J_{\rm sc}$ =11.8 mA/cm²; (b) $J_{\rm sc}$ =21.9 mA/cm²; (c) $J_{\rm sc}$ =32 mA/cm². Reprinted from [104], with the permission of AIP Publishing.

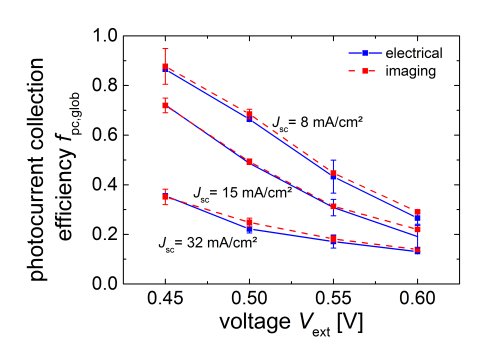


Figure 6.8.: The global differential photocurrent collection efficiency of a c-Si solar cell determined at different illumination conditions (given by the respective short circuit currents) plotted against the external voltage. The results in blue are determined from external electrical measurements and the results in red are determined via the average of the $f_{\rm pc,loc}$ images. The overlap of the curves shows that the photocurrent collection efficiency imaging method provides quantitatively correct results.

The Total Photocurrent Collection Efficiency

The total photocurrent collection efficiency was measured for the same c-Si solar cell that was used in the previous section. For that $f_{\rm pc,loc}$ images were measured at several more different illumination intensity. The laser intensity was increased in 12 steps from zero to $0.115\,\rm W/cm^2$. The maximum illumination intensity corresponded to a short circuit current density of $32\,\rm mA/cm^2$ of the solar cell, which is close to the short circuit current density of the solar cell under standard AM 1.5 spectrum (32.7 mA/cm², cf. Section 3.1.4). Simultaneous to the measuring of the $f_{\rm pc,loc}$ images also the external current changes due to the illumination changes were recorded. From these measurements an $F_{\rm pc,loc}$ image is calculated using Equation 6.14.

On a global scale the calculation process is visualized in Figure 6.9. When plotting the global differential photocurrent collection efficiency versus the short circuit current density at which it was measured, the area below the curve corresponds to the global collected photocurrent density $J_{\rm coll,glob}$. Dividing $J_{\rm coll,glob}$ by the short circuit current density yields the total global photocurrent collection efficiency.

Figure 6.10 shows the actual $F_{\rm pc,loc}$ image. The image looks in principle quite similar to the $f_{\rm pc,loc}$ images (Figure 6.7). However, due to the fact that the photocurrent collection is more efficient at lower illumination intensities the total photocurrent collection efficiency image yields always higher values than the differential one (for the same operating point). Thus, the differential photocurrent collection efficiency measurements overestimates the influence of defects on the photocurrent collection properties of the solar cell.

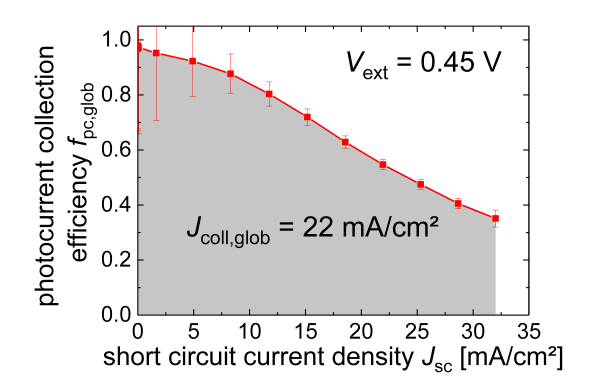


Figure 6.9.: Demonstration of the calculation of the total photocurrent collection efficiency from the differential photocurrent collection efficiency. When plotting the differential photocurrent collection efficiency versus the short circuit current density the area under the graph yields the collected photocurrent density. Dividing the collected photocurrent density by the maximum short circuit current density leads to the total photocurrent collection efficiency.

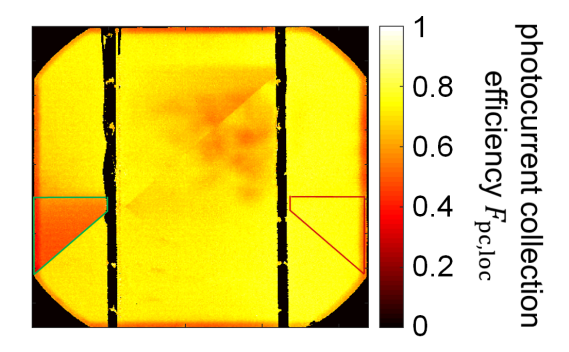


Figure 6.10.: Total photocurrent collection efficiency image of a c-Si solar cell taken for $V_{\rm ext}=0.45\,\rm V$ and $J_{\rm sc}=32\,\rm mA/cm^2$. The image was used to estimate the current loss in the green framed area that results from a crack. More details in the text. Reprinted from [104], with the permission of AIP Publishing.

As an example what can be learned from the $F_{\rm pc,loc}$ image, the green framed region in Figure 6.10 is analyzed in more detail. In this region the photocurrent collection efficiency is reduced due to a crack in the solar cell. The fingers are no longer connected to the bus-bar and the area therefore has a higher series resistance. The area has an average $F_{\rm pc}$ of 0.52. Using the area size (5.3 cm²) and the short circuit current density of $32\,{\rm mA/cm^2}$ we can calculate that at 0.45 V 88 mA of the total collected photocurrent originate from the green framed region. In contrast to that has the red framed region (which is of the same size and at a similar position, but not influenced by the crack) an average $F_{\rm pc}$ of 0.74 and therefore 126 mA originate from this region. Thus, due to the crack in the green framed region the sample loses around 38 mA of its generated photocurrent. As the solar cell collects in total at 0.45 V 3.01 A the crack results in a photocurrent loss of about 1.3 %.

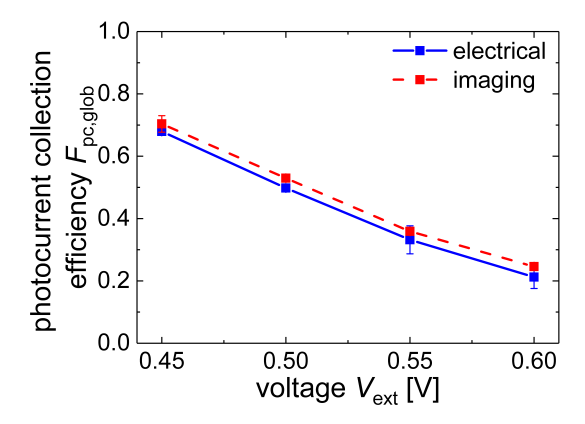


Figure 6.11.: The global total photocurrent collection efficiency of a c-Si solar cell determined for a short circuit current density of $32\,\mathrm{mA/cm^2}$ plotted against the external voltage. The results in blue are determined from external electrical measurements and the results in red are determined via the average of the $F_{\mathrm{pc,loc}}$ images. The closeness of the two curves underlines the validity of the total photocurrent collection efficiency imaging method.

As for c-Si solar cells the theory of the differential photocurrent collection efficiency was already verified (cf. Section 6.2) and only mathematical transformation of these values were used to determine the total photocurrent collection efficiency there should be no reason why Equation 6.15 should not hold. However, to emphasize that, Figure 6.11 shows the global total photocurrent collection efficiency values determined directly from electrical measurement and determined from the averages of $F_{\rm pc,loc}$ images at different voltages for the maximum illumination intensity. The results are close together and show the same dependence on $V_{\rm ext}$. The slight offset might result from imperfect active area determination, which adds a

systematic error.

6.2.2. Simulation and Discussion

In this section PVMOS simulations of a small crystalline silicon solar cell with and without a shunt will be used to verify the differential photocurrent collection efficiency method on a local scale. Furthermore, a full scale crystalline silicon solar cell will be modeled with an without defects. The newly developed total photocurrent collection efficiency and net power imaging methods will be demonstrated and verified using these silicon solar cell models. Additionally, the simulations will show how various types of defects affect the imaging results.

Verification on a Local Scale

The differential photocurrent collection efficiency $f_{\rm pc,loc}$ is defined as the change of the current at the terminals of a device when the locally generated photocurrent changes (cf. Section 6.1.1). In the experiments relation 6.4 was used to determine $f_{\rm pc,loc}$ and the relation was verified by calculating from $f_{\rm pc,loc}$ the global photocurrent collection efficiency $f_{\rm pc,glob}$ (cf. Equation 6.3), which is measurable independent of the imaging procedure. To test the relationship on a local scale experimentally is a lot more challenging, as a setup would be needed that can locally vary the illumination of a sample while the sample is under a bias illumination under normal operating conditions. For this reason PVMOS simulations are used to calculate $f_{\rm pc,loc}$ directly from varying the local illumination intensity. The program allows the fast determination of the change of the current at the terminals of a device resulting from a small change in the local photocurrent.

For the first PVMOS cell simulations, a small silicon solar cell was modeled. The cell was 2 x 2 cm² large and had a grid with one bus-bar and five fingers. The used diode and resistance parameters are given in Section 3.1.4 (Table 3.7). The smaller cell structure (compared to the measured crystalline silicon solar cell) was chosen to avoid extensive calculations that arise with the direct determination of $f_{\rm pc,loc}$ in PVMOS. The results of the $f_{\rm pc,loc}$ simulations for this cell and the same cell including a circular shunt with a resistance of $1.5 \times 10^{-4} \,\Omega {\rm cm}^2$ and a diameter of 0.4 mm are seen in Figure 6.12. It is seen, that the $f_{\rm pc,loc}$ images calculated from the local junction voltage changes using $dV_{\rm j}/dV_{\rm ext}$ is equal to the directly calculated image using $dj_{\rm coll,loc}/dj_{\rm ph}$. Additionally, the $f_{\rm pc,glob}$ values calculated from the different images align well. Thus, Equation 6.4 holds. The resolution differences result from a missing interpolation step, which was not performed for the direct $f_{\rm pc,loc}$ calculations.

The following idea is added to the differential photocurrent collection efficiency: Equation 6.4 was derived for an infinitesimal change in the locally generated photocurrent [29]. There are two ways to obtain a small photocurrent change. The first one is to change the illumination of the area, for which we want to know the

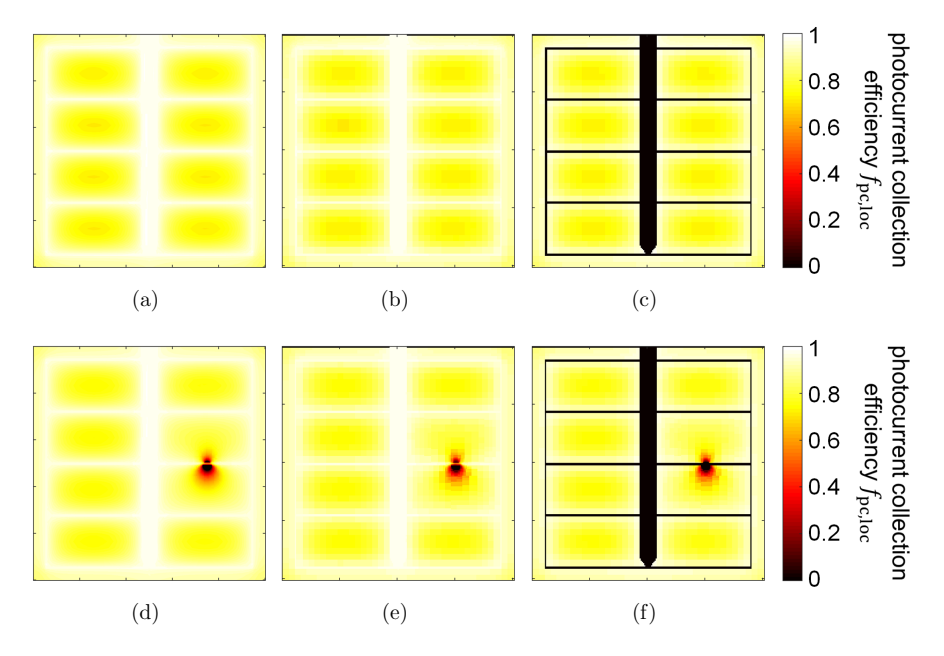


Figure 6.12.: Differential photocurrent collection efficiency images simulated for two $2 \times 2 \,\mathrm{cm}^2$ c-Si solar cells under illumination at $V_{\mathrm{ext}} = 0.56 \,\mathrm{V}$. (a),(d) was calculated using the differences of junction voltage images as used in the experiments; (b),(e) was determined by observing the external current changes resulting from infinitesimal local photocurrent changes; (c),(f) was calculated by observing the external current changes resulting from local photocurrent density change equal to the total locally generated photocurrent density. The cell simulated at the bottom has a shunt, while the top cell has no defect.

photocurrent collection efficiency, slightly. In fact that was done in the experiments when the global photocurrent collection efficiency was determined. However, another way to achieve an infinitesimal change of the photocurrent would be to make the area where we change the photocurrent infinitesimal small. In such a way, even if the photocurrent density change is equal to the photocurrent density of the solar cell, the actual photocurrent change is very small. Thus, the change of the current at the terminals of a sample resulting from a certain small area being completely shadowed, is expected to be given by the $f_{\rm pc,loc}$ of that area.

The idea was tested by calculating in the simulations $f_{\rm pc,loc}$ images that result from setting the photocurrent completely to zero once for every node and observing the resulting external current change. As seen in Figure 6.12 the results are identical to the $f_{\rm pc,loc}$ images determined from junction voltage changes or infinitesimal small photocurrent changes (not under the grid as the PVMOS algo-

rithm does not induce a photocurrent change there as the original photocurrent under the grid is already zero). This shows that $f_{\rm pc,loc}$ not only gives information about how much a small photocurrent change influences the current at the terminals of the device, but also how a larger local photocurrent density change even equal to the one resulting from 1 sun illumination or complete shadowing influences the current at the terminals of the device.

However, it should not be misunderstood: It does not follow that we obtain the current loss that would result from a complete shadowing of the cell by adding up the losses from the different partial shadowing. The $f_{\rm pc,loc}$ value of a certain area still only holds if the rest of the sample is under the condition for which it was determined. Meaning that if a complete cell is shadowed the $f_{\rm pc,loc}$ image determined beforehand for a condition where the sample was completely illuminated does not hold anymore. It will not describe the current loss resulting from the shadowing, as the operating condition of the complete cell changed.

Shunt Simulations

In the experiments it is difficult to estimate the effect of a shunt on $f_{\rm pc,loc}$, especially if we want to compare a situation with a shunt to the same situation without a shunt. Different cells vary slightly and introducing a realistic shunt into a solar cell is difficult. However, in simulations it is possible to introduce a shunt into a solar cell while all other properties stay constant. In this section further simulations results for the cells used in the previous section are discussed and we take a look at the role of the shunt in more detail.

The calculated $f_{\rm pc,loc}$ images for the cell with the shunt are compared in Figure 6.13 to the $f_{\rm pc,loc}$ images of the cell without the shunt at different voltages. At both operating points the shunt decreases $f_{\rm pc,loc}$ close to it. However while at 0.46 V the shunt reduces the $f_{\rm pc,loc}$ in the adjacent area framed by the grid compared to the non-shunted cell, at 0.71 V the $f_{\rm pc,loc}$ is larger in in the adjacent area framed by the grid of the shunted cell than the non-shunted cells (except close to the shunt).

When looking at the $f_{\rm pc,glob}$ determined from the averages of the images in Figure 6.14 it is also seen that the shunt reduces $f_{\rm pc,glob}$ at low voltages while it is larger at high voltages. As the result is very similar to the one predicted by a one diode model (cf. Figure 6.4) the same argument is used to explain the effect. The shunt reduces the local junction voltages at a given external voltage. This leads to a less conductive diode counteracting the increased conduction resulting from the shunt. This increased diode resistance leads to an increase of the photocurrent collection efficiency especially at operating points where the conduction of the diode limits photocurrent collection. A shunt is the easiest example to show that a differential photocurrent collection efficiency image cannot be easily used to describe the local performance of a solar cell.

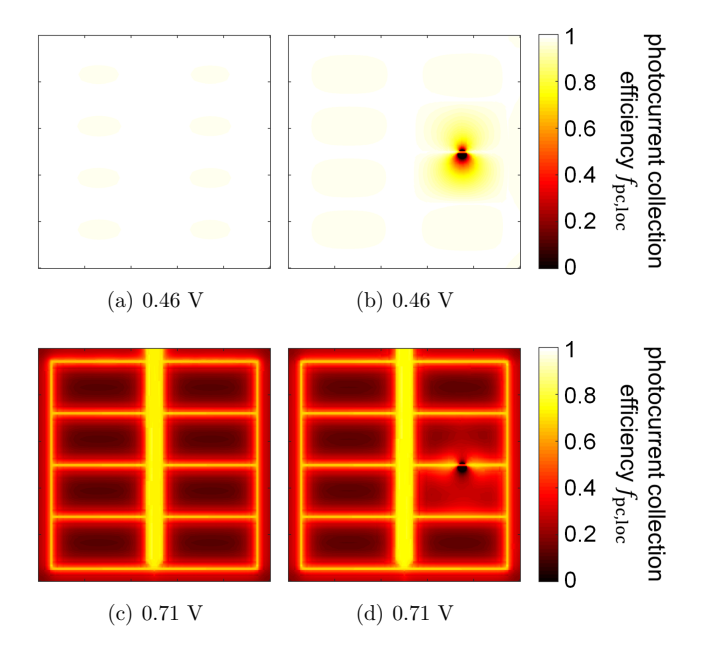


Figure 6.13.: Simulated $f_{pc,loc}$ images of a shunted (b,d) and a non shunted (a,c) cell at different operating voltages under illumination. Depending on the operating point the shunt may decrease or increase the photocurrent collection efficiency of certain cell areas.

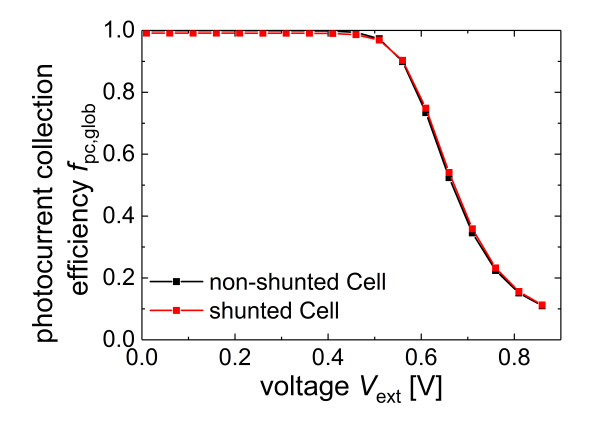


Figure 6.14.: The quantity $f_{\rm pc,glob}$ calculated from $f_{\rm pc,loc}$ images at different voltages for a shunted and a non-shunted simulated solar cell. Depending on the operating voltage the shunt may increase or decrease the photocurrent collection efficiency.

The Total Photocurrent Collection Efficiency

To demonstrate that total photocurrent collection efficiency imaging can be applied to any kind of solar cell that can be modeled with a standard equivalent circuit network, a realistic larger c-Si solar cells is simulated using PVMOS. The total photocurrent collection efficiency is determined and verified using a comparison to the electrically determined global total photocurrent collection efficiency (cf. Equation 6.15). The cell is $12.5 \times 12.5 \, \mathrm{cm^2}$ large and is contacted via a grid consisting of three bus-bars and 63 fingers. Again, the parameters introduced in Section 3.2.2 (Table 3.7) are used to describe the electric properties. The cell was simulated with and without additionally introduced defects. The defects were a circular shunt with a diameter of 0.4 cm and a resistance of $0.15 \, \Omega \mathrm{cm^2}$, as well as a region where the emitter sheet resitance was increase to $1000 \, \Omega$ and a region where the dark saturation current was increased to $7 \cdot 10^{-7} \, \mathrm{mA/cm^2}$. The defects may seem quite drastic and are unlikely to appear like that in a real solar cell. However, verifying that $F_{\mathrm{pc,loc}}$ imaging even works under such conditions shows the robustness of the method.

Figure 6.15 shows the $F_{\rm pc,loc}$ images for different voltages under illumination. For the determination of $F_{\rm pc,loc}$ the locally generated short circuit current density was changed in 8 steps from 0 to 35 mA/cm² and $f_{\rm pc,loc}$ images are determined at each step using $\delta V_{\rm ext}$ =0.02 V. For the defected and the non-defected cell again the typical decrease of the photocurrent collection with increasing voltage is seen. We also see in the defected cell how all the introduced defects reduce the photocurrent collection. The shunt is visible at all applied voltages while the areas where the series resistance or dark saturation current are increased only lead to a higher loss of photocurrent at higher voltages.

It is visible here [especially by comparing Figure 6.15 (a) and (b)] that defects will also influence the photocurrent collection properties of the surrounding area, which is not defected. The $F_{\rm pc,loc}$ of non-defected regions in a defected cell will always be influenced by the defected region. Therefore, we have to be careful when making a photocurrent collection loss analysis using different areas in the same solar cell as was done in Section 6.2.1. The photocurrent loss analysis discussed in the previous experimental section (Section 6.2) was correct as the defect was a series resistance problem and it is unlikely that the increased series resistance on one side of a solar cell influenced the series resistance of the other side of the solar cell much, especially with the fingers and the bus-bar present. However, to be more sure, comparisons via simulations or measurements to similar cells, which are non-defected are necessary.

Figure 6.16 shows again a comparison of the $F_{\rm pc,glob}$ values determined via the imaging technique and determined from the electrical characteristic of the cell (cf. Equation 6.15). That the results overlap so well even for the defected cell, shows again the applicability of the total photocurrent collection efficiency imaging method and also its accuracy as long as the sample can be described by the

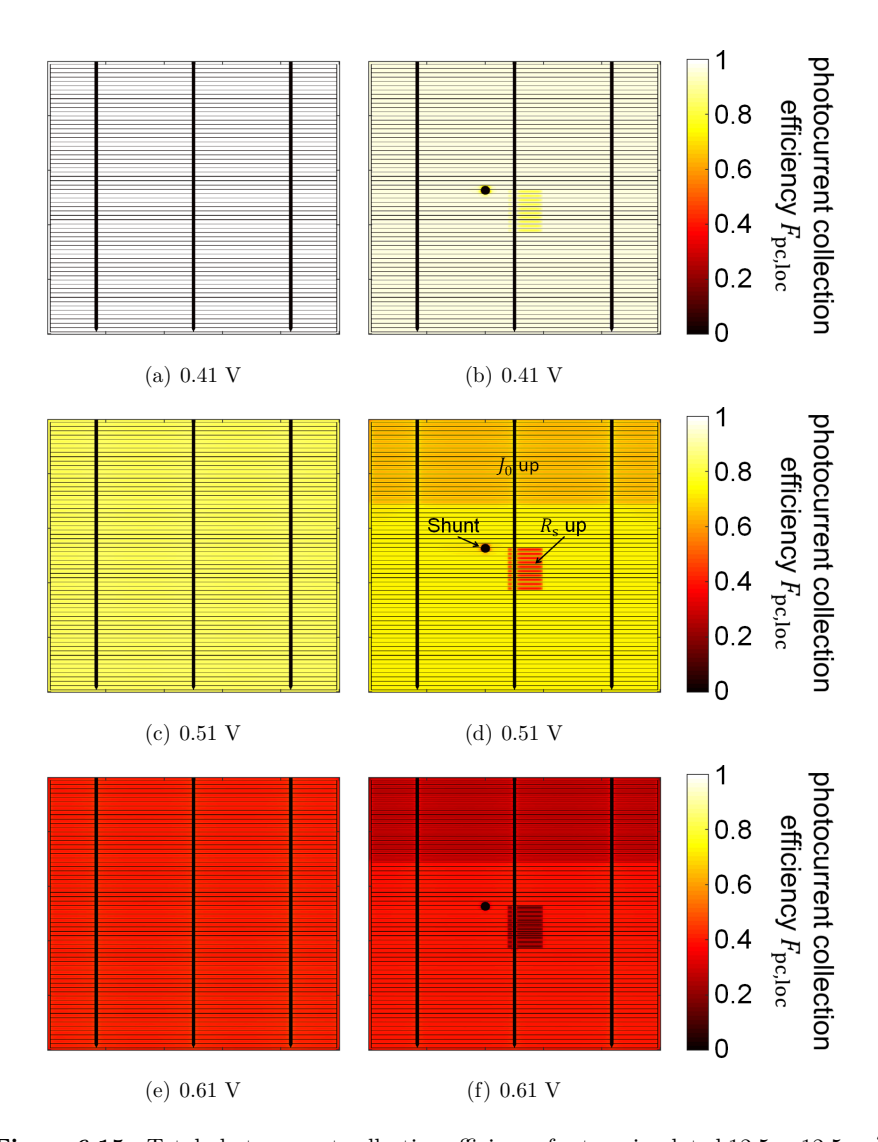


Figure 6.15.: Total photocurrent collection efficiency for two simulated $12.5 \times 12.5 \,\mathrm{cm}^2$ c-Si solar cells at different voltages under illumination. (a), (c) and (e) belong to the same non-defected cell; (b), (d) and (f) belong to the same defected cell. To show the influence of different defects the defected cell contains a shunt, a region where the front contact resistance was increased, and a region where the dark saturation current was increased.

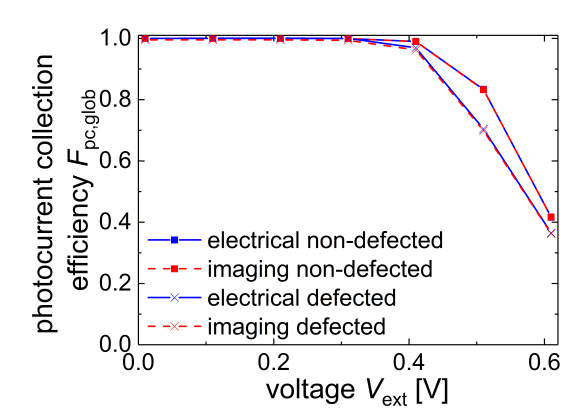


Figure 6.16.: The global total photocurrent collection efficiency of a defected and non-defected simulated c-Si solar cell determined for a short circuit current density of $35\,\mathrm{mA/cm^2}$ plotted versus the external voltage. The results in blue are determined from external electrical characteristics and the results in red are determined via the averages of the $F_{\mathrm{pc,loc}}$ images. The excellent overlap of the curves shows the validity of total photocurrent collection efficiency imaging for solar cells.

equivalent circuit network used in [29] and homogeneous photocurrent generation can be expected. The method does not need any additional assumptions or approximation and it exactly relates electrical properties of the sample to its local origin within the cell. Note, that there is no way to measure or simulate an $F_{\rm pc,loc}$ image without the use of $f_{\rm pc,loc}$ images.

Net Power Imaging

In the following it will be demonstrated for a c-Si solar cell, how to calculate a net power image using simulations. For that the same defected c-Si solar cell is used, which was already used in the previous section. As discussed for a net power image, a collected and dissipated power image are needed. The CP image is calculated from a $F_{\rm pc,loc}$ image using Equation 6.16. The results are seen in Figure 6.17 (a),(b) and (c). Collected power images look very similar to $F_{\rm pc,loc}$ images except that their values decline towards high and low external voltages (cf. Equation 6.16, not visible in the figure). The DP images for the same voltages are shown in Figure 6.17 (d),(e) and (f) and were determined from the current flow through the z-direction of the solar cell multiplied with the external voltage. These images only increase with increasing voltage. We see that the dissipated power is higher through the shunt of the cell at all voltages. The power loss due to the region where J_0 is increased only starts at higher voltages. What is also interesting, is that the region of enhanced series resistance shows a lower dissipated

power as the current flowing there is limited by the resistance.

By subtracting the DP image from the CP image, the NP image is obtained (Figure 6.17 (g),(h) and (i)). These images are directly related to the power output of the cell at the different voltages. At low voltages it is more influenced by the photocurrent collection properties of the solar cell as not much power is dissipated in most of the cell (except for the shunted region). As the voltage increases, the loss of power due to the recombination and shunts increases and heavily influences the performance of the different regions. Note, that the power output of regions can also be negative. The scale only does not go below zero for a better visibility of differences.

In Figure 6.18 it is shown that Equation 6.18 holds in our simulation. The net power output (positive values mean the solar cell is producing energy) is determined from the simulated I/V characteristic of the defected and a non-defected solar cell and calculated from the integral across the respective NP images. As the results overlap well, with NP imaging a method is obtained that quantifies the performance of a region in a solar cell. Its overall intensity is highest at the maximum power of the solar cell. The image yields exactly how much each individual area of a solar cell contributes to the overall power output of the cell.

However, it is important to note, that the net power output of a region is not only related to the materials properties in this region. For example, the material close to the shunt is not better or worse than the material further away from it, but we see especially in Figure 6.17 (i) that the power output from that area seems to be higher than from areas further away from the shunt that are not influenced by other defects. The reason for that is that the shunt pulls current away from the surrounding area, meaning that less power is dissipated there (but more power is dissipated in the shunt). As the photocurrent collection from the area around the shunt is not affected by the shunt in the same scale, the area around the shunt provides more output power to the solar cell than other areas although its local material properties are actually the same.

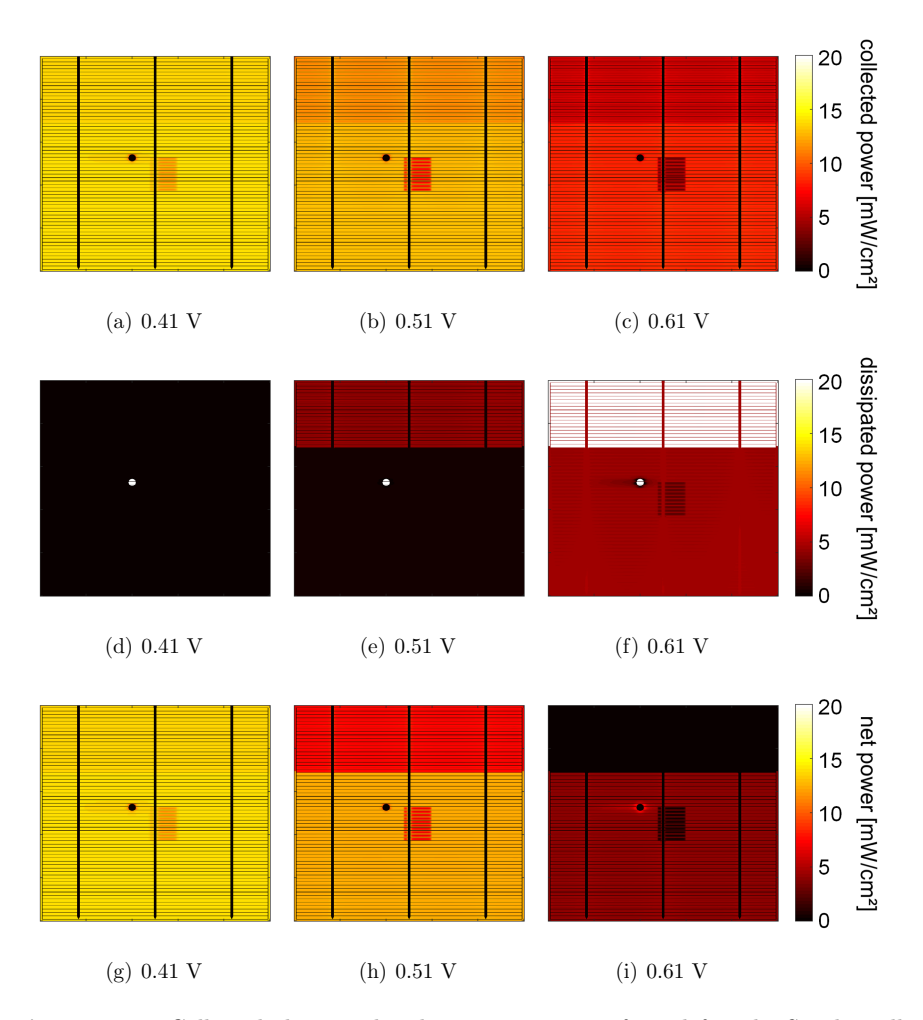


Figure 6.17.: Collected, dissipated and net power images for a defected c-Si solar cell at different voltages. The net power image result from a subtraction of the dissipated power image from the collected power image.

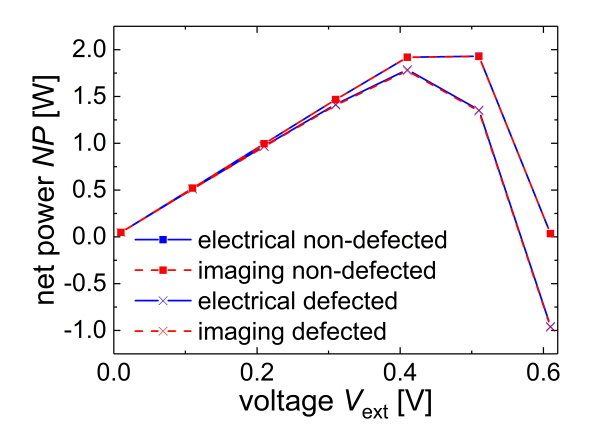


Figure 6.18.: The total power output of a defected and non-defected simulated c-Si solar cell, determined simply from I/V characteristics (blue) and from net power images (red). The overlap shows that the integral over the net power images yields exactly the total power output of the solar cell.

6.3. Solar Modules

In the following it will be discussed and demonstrated how photocurrent collection efficiency imaging works for solar modules and what can be learned from the results. As solar modules consist of series connected solar cells, it needs to be understood how the series connection influences $f_{\rm pc,loc}$. In [111] it was shown that Equation 6.4 also holds for the case of series connection of cells, which makes imaging of $f_{\rm pc,loc}$ for modules possible. However, the properties and size of $f_{\rm pc,loc}$ will change due to the series connection of several cells.

Again, a simplified linearized equivalent circuit describing a solar module is used to analyze the changes to $f_{\rm pc,loc}$ we are expecting from experiments on solar modules. Figure 6.19 shows such a linearized equivalent circuit of a module with four cells. The resistors r_i stand for solar cells which are connected in series. The photocurrent collection efficiency for one cell i in the shown circuit can be derived similar to the photocurrent collection in a one diode model (cf. Equation 6.9 and 6.9). It reads

$$f_{\text{pc},i} = \frac{\delta I_{\text{coll}}}{\delta I_{\text{ph},i}} = \frac{r_i}{\sum_{i=1}^{n_{\text{cell}}} r_i},$$
(6.19)

where $n_{\rm cell}$ is the number of cells in the module. Thus, if all the cells are equal in a module the photocurrent collection efficiency of the individual cells is smaller by the factor of $1/n_{\rm cell}$ compared to the $f_{\rm pc}$ of single cell.

This behavior of $f_{\rm pc}$ for modules also holds when $f_{\rm pc}$ is determined from local junction voltage images. An external voltage change is divided up between all the

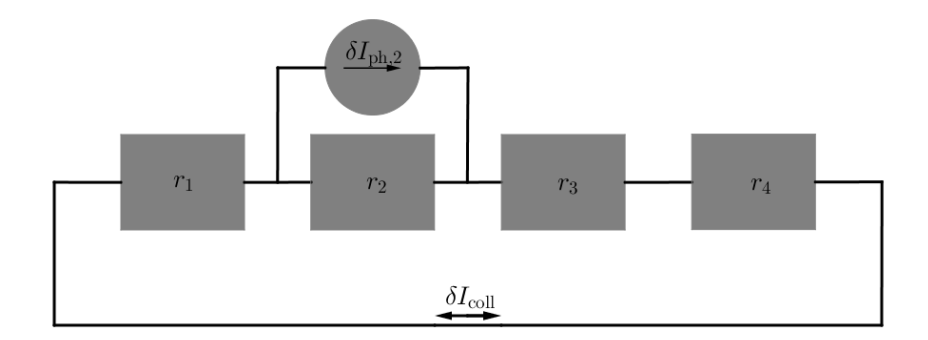


Figure 6.19.: Linearized equivalent circuit that describes a solar module. The resistors r_{1-4} describe the individual cells in the module. A photocurrent induced in one cell has to flow through all others cells to be collected.

individual cells in the module and the local junction voltage is therefore depending on all the individual cells in the module

$$f_{\text{pc},i} = \frac{\delta V_{\text{j},i}}{\delta V_{\text{ext}}} = \frac{r_i}{\sum_{i=1}^{n_{\text{cell}}} r_i}.$$
(6.20)

Note, that Equation 6.19 and 6.20 are derived for the shown simplified circuit in Figure 6.19, which does not include any series resistances in cell i.

6.3.1. Experimental Results

For the analysis of modules the two CIGS mini-modules that were already analyzed in Chapter 5 are used. Note, that the influence of the series connection on the photocurrent collection efficiency seen and discussed in this section are also relevant for crystalline silicon solar modules. The results discussed here were confirmed with outdoor photocurrent collection efficiency measurements performed on crystalline silicon solar modules in parallel to this work [9].

The same procedure that is used for solar cells to measure differential photocurrent collection efficiency images is applied to solar modules. Using the log-method photocurrent collection efficiency images were determined for the two mini-modules at different voltages using $\delta V_{\rm ext} = 0.2\,\rm V$. The results are shown in Figure 6.20. As expected the $f_{\rm pc,loc}$ values are significantly lower than the one measured for solar cells. Note that the scale in the images goes to 0.059 which is approximately 1 divided by the number of cells of the module. Except that its magnitude is decreased, $f_{\rm pc,loc}$ behaves for the module without the defects very similar to the $f_{\rm pc,loc}$ of a single cell. At low voltages $f_{\rm pc,loc}$ of the individual cells is homogeneous while at higher voltages we see the increased influence of the front contact resistance, which decreases $f_{\rm pc,loc}$ on the right side of the cells.

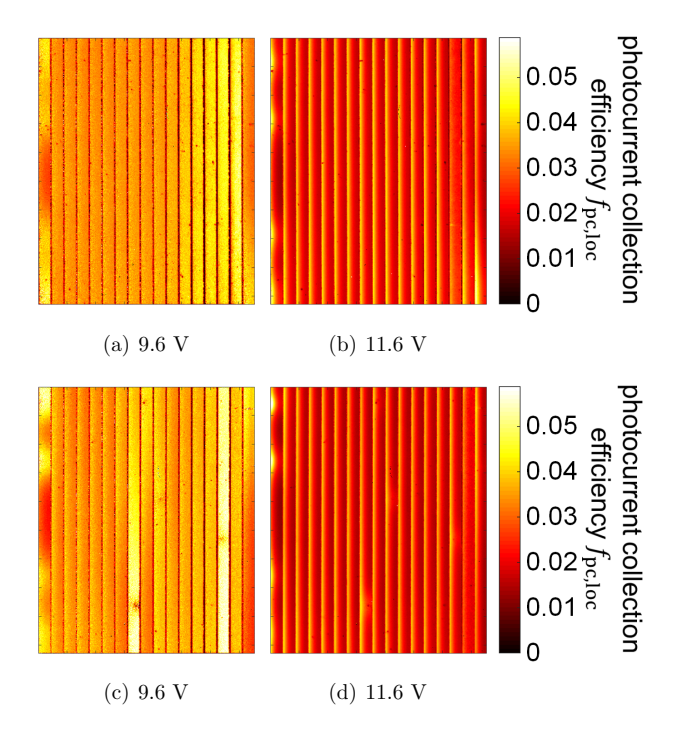


Figure 6.20.: Differential photocurrent collection efficiency images of two CIGS solar modules $(8.6 \times 6.8 \, \text{cm}^2)$ at different voltages under illumination. (a) and (b) a module with no severe defects.(c) and (d) a module with shunts. Reprinted from [102], with the permission of AIP Publishing.

More surprising is the behavior of $f_{\rm pc,loc}$ of the shunted cells in the defected module [Figure 6.20 (c)]. At the lower voltage the shunted cells (cell 8,9,10 and 15 counted from the left) show an overall larger $f_{\rm pc,loc}$ than the non shunted cells. Although, it was already discussed that this increase can occur in single cells due to shunts, the effect is usually expected at higher voltages (cf. Figure 6.13 and 6.14). In contrast, the $f_{\rm pc,loc}$ images at at higher voltages ($V_{\rm ext}=0.56\,{\rm V/cell}$) look very similar and the shunts have nearly no influence. Thus, it is concluded that the effect results from the series connection of cells.

6.3.2. Simulations and Discussion

Differential Photocurrent Collection Efficiency

To prove that the increased $f_{\rm pc,loc}$ of the shunted cell is indeed a result of the series connection PVMOS simulations were used. Simulations provide the opportunity to analyze the single cell properties without the influence of the series connection, making it possible to differentiate between effects resulting from the defects in the cell and effects resulting from series connection. In the following the $f_{\rm pc,loc}$ images at different voltages under illumination are determined for the in Section 5.1 and 5.2 studied and simulated module with defects. Additionally, an $f_{\rm pc,loc}$ image is determined from the simulations, where the photocurrent collection efficiency for the individual cell is determined without the influence of the series connection. This image is obtained by dividing the $\delta V_{\rm j}$ image of each individual cell by their respective local cell voltage change that is induced by an external voltage change. This quantity is not easily determinable in an experiment but in the simulations it is possible to obtain the exact voltage drop across each cell.

Figure 6.21 shows the calculated images. At 9.6 V the shunted cells show a larger photocurrent collection efficiency than the other cells, while the effect is reduced at higher voltage. This behavior was also seen in the experiment. Additionally, the simulations provide images at lower voltages where the signal-to-noise ratio inhibits the acquisition of experimental results. Here, we see that at 4 V the photocurrent collection efficiency of the shunted cells decreases again below the $f_{\rm pc,loc}$ of the other cells.

When looking at the $f_{\rm pc,loc}$ determined as if the cells were not connected in series [Figure 6.21 (d),(e),(f)], we see the typical behavior for a shunted cell, which was already discussed in Section 6.1.1 and 6.2.2. Thus, the low photocurrent collection efficiency of the shunted cell at low voltages and its increase above the $f_{\rm pc,loc}$ of the other cells towards higher voltages is a result of the series connection of several cells. The behavior is again illustrated in Figure 6.22. In part (a) it shows the behavior of the average the $f_{\rm pc,loc}$ values of a shunted and a non shunted cell, as it was determined for the whole module. The $f_{\rm pc,loc}$ of the shunted cell exhibits a maximum around 8 V. We also see that around the same voltages the $f_{\rm pc,loc}$ of the non-shunted cells obtains a local minimum, which is also not expected for $f_{\rm pc,loc}$ values of single cells. The behavior of $f_{\rm pc,glob}$ when determined for cells individually is seen in part (b) of Figure 6.22. Here, we see that the influence of the shunt on the overall photocurrent collection efficiency of the cell is actually minor, if the cells would be operated alone without the series connection to other cells.

Figure 6.23 is used to explain the behavior of $f_{\rm pc,loc}$ in a module. It shows the I/V-characteristic of shunted and a non-shunted cell. If the two cells are connected in series it means that the current through the cells will be the same while the voltage across the individual cells can vary. Let us assume we are interested in the

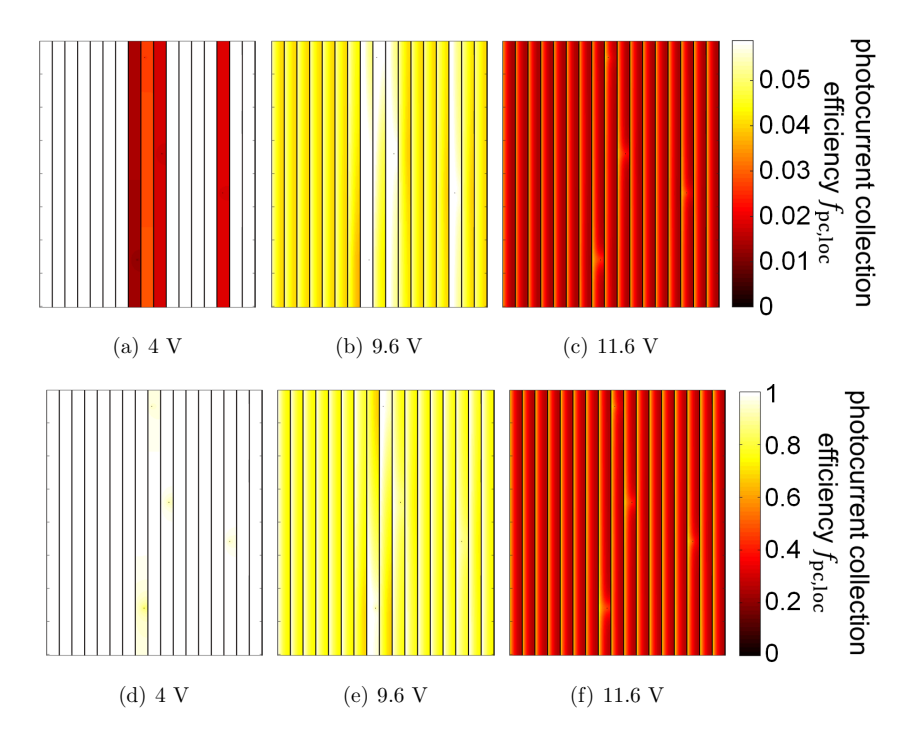


Figure 6.21.: Modelled photocurrent collection efficiency images of a CIGS Module with shunts. In (a),(b) and (c) the $f_{\rm pc,loc}$ was determined for the complete module; (d),(e) and (f) show the corresponding $f_{\rm pc,loc}$ if it would be determined for each cell individually without the influence of the series connection to the other cells. Reprinted from [102], with the permission of AIP Publishing.

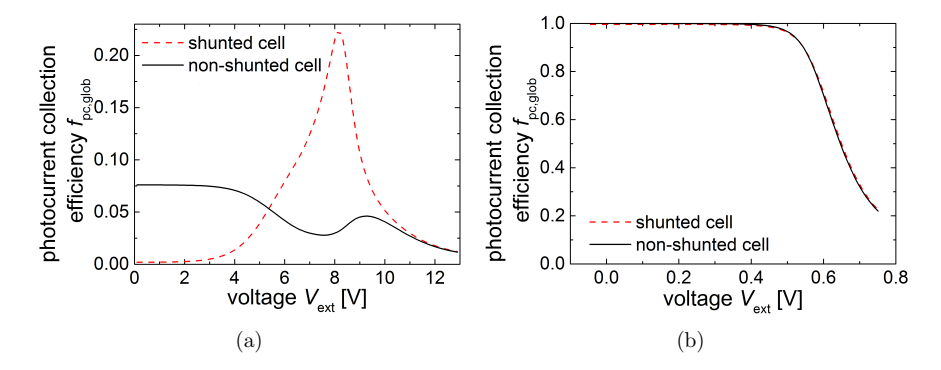


Figure 6.22.: The average photocurrent collection efficiency of a shunted cell (8th from the left) and non-shunted cell (5th from the left) in the simulated module. (a) Determined while the cell is as usually connected in series to the other cells of the module; (b) determined for the cell as it would be seen without the series connection. Reprinted from [102], with the permission of AIP Publishing.

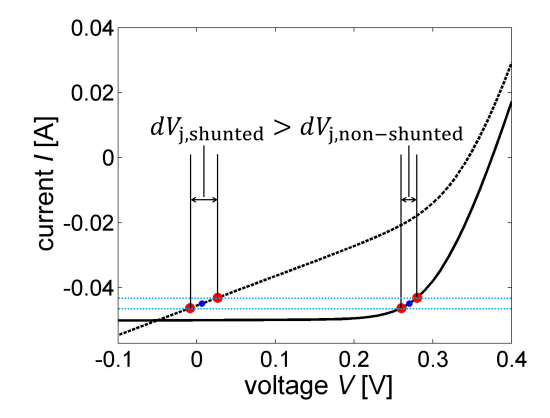


Figure 6.23.: I/V-characteristic of a shunted (black dashed line) and a non-shunted cell (black compact line) to understand how the series connection of cells in a module influences the photocurrent collection efficiency measurement. As the two cells operate in series, an external voltage changes leads in both cells to the same current change (light blue vertical lines). The resulting voltage change across the two individual cells can be larger for the shunted cell resulting in a larger $f_{\rm pc,loc}$ of the shunted cell. Reprinted from [102], with the permission of AIP Publishing.

 $f_{\rm pc,loc}$ of the two cells at the operating point defined by the current of the blue dot. To determine this $f_{\rm pc,loc}$ image the external voltage (across both cells) is varied slightly (by $\delta V_{\rm ext}$), which in turn results in an equal current change through the two cells (illustrated by the red dots and the two light blue vertical lines). Now this current change, leads in the shunted cell to a larger voltage change than for the non-shunted cells. This happens as, at the same current, the differential resistance of a shunted cell can actually be higher than the differential resistance of the non-shunted cell. As we now see, this leads to a change of the junction voltage of the shunted cell that is higher than the change of the junction voltage of the non-shunted cell, which leads then according to Equation 6.4 to a larger $f_{\rm pc,loc}$ of the shunted cell. The effect is reversed at low currents as the differential resistance of the non-shunted cell is high at low currents. At high voltages the differential resistance of both cells align, leading to a similar photocurrent collection efficiency.

This behavior seen for the f_{pc} of shunted cells in solar modules is also described in Equation 6.19 or 6.20. It states that the photocurrent collection efficiency of a cell in a module depends on the ratio between its own series resistance and the series resistance of all cells in series. Thus, we can differentiate between three possible situations. First, if the cell's resistance is lower than the average resistance of all the cells in the module, the cell's photocurrent collection efficiency will also be lower than the average photocurrent collection efficiency of the module. The cell's ability to collect photocurrent is decreased due to recombination within the cell. Second, if the cell's resistance is higher than the average resistance of all the cells in the module, the cell's photocurrent collection efficiency will also be higher. In this case, the recombination within the cell has a higher resistance and it therefore is able to collect more photocurrent. However, the cell also imposes a higher series resistance on the other cells in the module and therefore decreases their photocurrent collection efficiency. The third possible situation would be that a cell's resistance is similar to the resistance of the other cells. In this case the photocurrent collection efficiency is also similar to the other cells.

As discussed with the help of Figure 6.23, the differential resistance of a shunted cell is from low to high currents first lower than the resistance of a non-shunted cell, then becomes larger than it, and then becomes equal to the resistance of the non-shunted cell. Note, that this behavior of the differential resistances is due to a comparison of the individual cell resistances at the same currents instead of the same voltages. The behavior of the differential cell resistance then results in the respective behavior of the photocurrent collection efficiency. The sensitivity of the photocurrent collection efficiency to individual cell resistances and their relation to the average resistance of all the cells in the module makes photocurrent collection efficiency imaging useful to analyze and quantify the role of defects in solar modules.

Total Photocurrent Collection Efficiency

As the differential photocurrent collection efficiency is also measurable for modules (cf. Section 6.3.1), it should be also possible to determine a total photocurrent collection efficiency image of a module. However, we have to consider that the short circuit current has a different relationship to the locally generated photocurrent density for a module than for a cell. For a cell it holds

$$I_{\rm sc} = J_{\rm sc} \times A \tag{6.21}$$

where A is the Area of the sample, while for a module it holds that

$$I_{\rm sc} = \frac{J_{\rm sc} \times A}{n_{\rm cell}} \tag{6.22}$$

where A is again the Area of the entire sample (module). This follows from the series connection of the cells in the module. However, we keep the definition of $I_{\text{coll,glob}}$ the same, so that $J_{\text{coll,glob}} = I_{\text{coll,glob}}/A$. It follows the slightly different definition of $F_{\text{pc,glob}}$ for modules

$$F_{\text{pc,glob}}\left(V_{\text{ext}}, I_{\text{sc}}\right) = \frac{J_{\text{coll,glob}}\left(V_{\text{ext}}, I_{\text{sc}}\right)}{J_{\text{sc}}} = \frac{I_{\text{coll,glob}}\left(V_{\text{ext}}, I_{\text{sc}}\right)}{n_{\text{cell}} \times I_{\text{sc}}}.$$
 (6.23)

By defining $F_{\text{pc,glob}}$ for a module in that way, $F_{\text{pc,glob}}$ is still given by the average of $F_{\text{pc,loc}}$ of a sample (cf. the third term of Equation 6.15).

The base module parameters, discussed before in Section 5.2, are used to demonstrate $F_{\rm pc,loc}$ imaging for modules. The same procedure that is used for cells and is described by Equation 6.14 is applied. The locally generated current density of the solar module is varied between zero and $35\,{\rm mA/cm^2}$ in 7 steps and $f_{\rm pc,loc}$ images determined for each step are used to determine the $F_{\rm pc,loc}$ images at different voltages.

Figure 6.24 shows the images for three slightly different modules at different voltages. A module without any defects was simulated as well as the module with several shunts (same module which was simulated in Section 5.2) and a module where the sheet resistance of one cell was drastically increased. The non-defected module behaves similar to the single cell, showing the typical decrease of photocurrent collection efficiency with increasing voltage. For the module with the shunted cells we see the behavior of $F_{\rm pc,loc}$ mirrors what was already seen for the $f_{\rm pc,loc}$ of modules. This behavior shows that at certain operating points the larger portion of the total photocurrent is actually collected from the shunted cells and that they are limiting the collection from the other cells.

What is also important is that for a module the behavior of $f_{\rm pc,loc}$ with the illumination intensity is also not as straight forward as it is for cells. For cells, a decrease of $f_{\rm pc,loc}$ with the illumination intensity is seen, which leads to the fact that $F_{\rm pc,loc}$ values were always higher than $f_{\rm pc,loc}$ values. This is not necessarily the

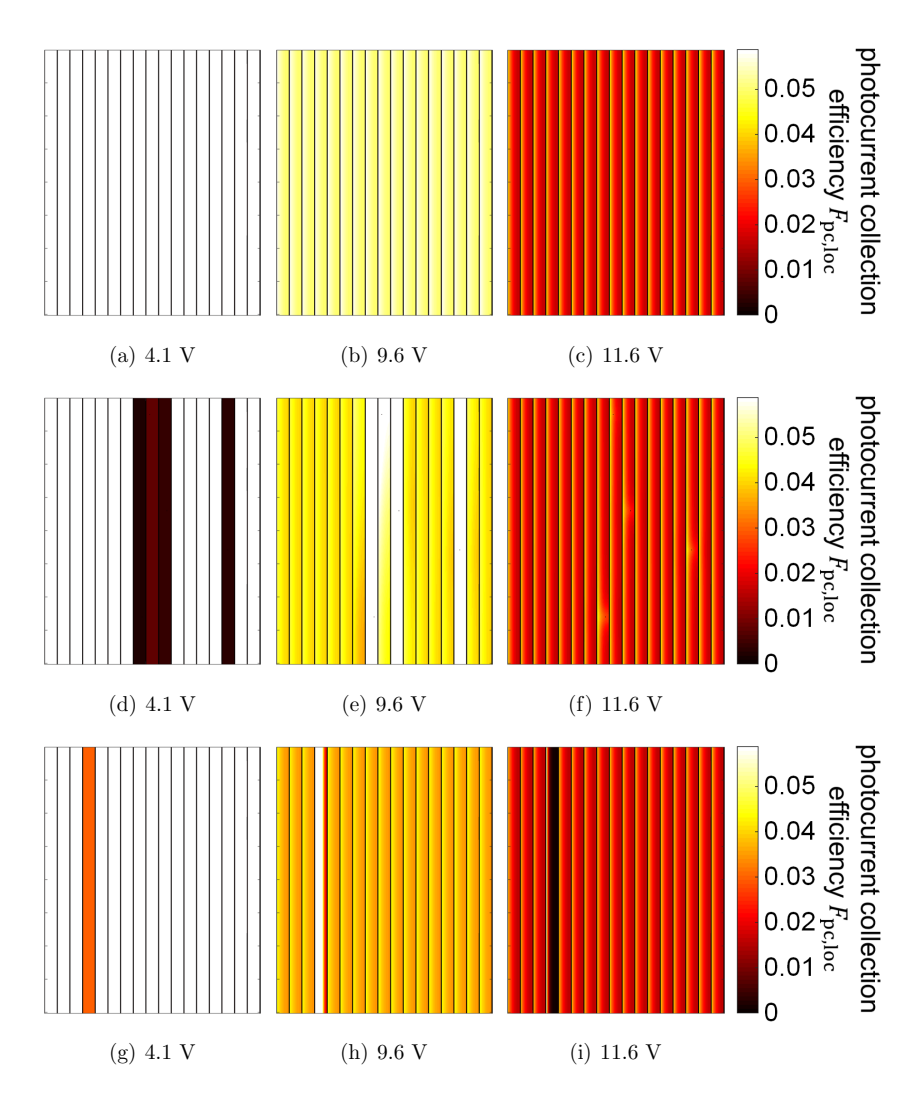


Figure 6.24.: Simulated total photocurrent collection efficiency of three different modules at $J_{\rm sc}=35\,{\rm mA/cm^2}$ and different voltages. Images (a),(b) and (c) show a module without a defect. The second line shows images of a module with several different shunts [(d),(e),(f)] and the third line shows a module where just one cell (4th from the left) is given a higher sheet resistance of $500\,\Omega$ [(g),(h),(i)].

case for a module with defects. Here, the $f_{\rm pc,loc}$ of the different cells can actually decrease or increase with illumination depending of the operating point and the properties of all the cells in the module. This leads for example to lower $F_{\rm pc,loc}$ values for the shunted cell at low voltages (here $f_{\rm pc,loc}$ increases with illumination) than $f_{\rm pc,loc}$ values for the same cell (cf. Figure 6.24 (d) and Figure 6.21 (a)) and lower $F_{\rm pc,loc}$ values than $f_{\rm pc,loc}$ value for the non-shunted cells at 9.6 V (cf. Figure 6.24 (e) and Figure 6.21 (b)). This makes $F_{\rm pc,loc}$ images more valuable for modules as the actual influence of local properties on the photocurrent collection are less predictable from $f_{\rm pc,loc}$ images alone.

Similar to the shunted cells, the cell where the sheet resistance was increased shows lower photocurrent collection efficiency at low and high voltages, while it is increased in between and higher than the remaining cells (cf. Figure 6.24 (g)-(i)). The reasons, for that are similar to the one for shunted cells. The $f_{\rm pc,loc}$ of the cells depend among other things on the relationship of their differential resistance to the differential resistance of the other cells and when the differential resistance of a cell is higher at the same current, $f_{\rm pc,loc}$ of the cell is also higher.

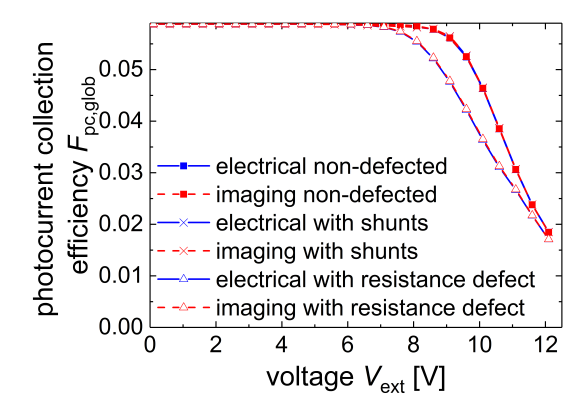


Figure 6.25.: The global total photocurrent collection efficiency of two defected and a non-defected simulated solar module determined for a short circuit current density of $35\,\mathrm{mA/cm^2}$ plotted against the external voltage. The results in blue are determined from external electrical characteristics and the results in red are determined via the averages of the $F_{\mathrm{pc,loc}}$ images. The results for the shunted and non-defected module overlap mostly, as the global total photocurrent collection efficiency is not much reduced by the shunts. The increase of the series resistance in one cell has a much larger influence on the global photocurrent collection efficiency of the respective module.

Once again the total photocurrent collection efficiency images are verified using the global photocurrent collection efficiency for the modules (cf. Equation 6.15 and Equation 6.23). Figure 6.25 shows the resulting $F_{\rm pc,glob}$ values for the different modules and different voltages. Again the values resulting from the images and their respective values determined electrically overlap nicely, showing that total

photocurrent collection efficiency imaging can also be used for modules. What is interesting is that the results for the shunted cell and the non-defected cells are nearly identical. Thus, although the $F_{\rm pc,loc}$ images look heavily influence by the defects, the total photocurrent collection efficiency of the whole module is actually not changed that much. All the decrease or increase of the $F_{\rm pc,loc}$ values in individual cells is compensated by a change in the $F_{\rm pc,loc}$ of the remaining cells. The increase of the sheet resistance in one cell has in the present case a much larger influence on the photocurrent collection properties of a module, decreasing it significantly at higher voltages.

Net Power Imaging

In the previous paragraph it was discussed how $F_{\rm pc,loc}$ images can be determined and interpreted for modules. From these images a CP image can also be calculated for modules similar to the calculation for cell using Equation 6.16. However, determining a DP image for modules is even more complicated than it is for cells. The main property of DP image is that, if you integrate it across the entire module area it results in the power dissipated by the whole module if a voltage is applied to it in the dark. If we used the simple approach that we used for the cells we would greatly overestimate the local dissipated power. For a single cell in the dark it holds that the current flowing in every region through the cell in the z-direction is coming from one contact and flows to the other without adding to the current flowing in the z-direction at another region of the cell. However in a module, we have, due to the series connection, current flowing through one cell in the z-direction and then also through the next one. Therefore, determining the locally dissipated power from the product of the local current flow and the external voltage is wrong.

A solution to the problem can at least be found in simulations. As we want an image that integrated across the complete module area yields the dissipated power of the module, we would be fine by determining an image that provides the dissipated power in each cell. If such an image is added up across all cells, it should automatically yield a dissipated power image of the whole module. Thus, in simulations a DP image is obtained, by first determining again the current flowing in the z-direction of the module and then multiplying the current values with the voltages across the individual cells and not the voltage across the entire module. The local current and individual cell voltages generally cannot be accurately determined in experiments, but it might be possible to approximate them.

Figure 6.26 shows as an example CP, DP and NP images determined for the previously described (cf. Section 5.2 and 6.2.2) solar modules with several shunts. The CP images look of course similar to the $F_{\rm pc,loc}$ image from Section 6.2.2 except that their intensity is multiplied with the external voltage. The dissipated power

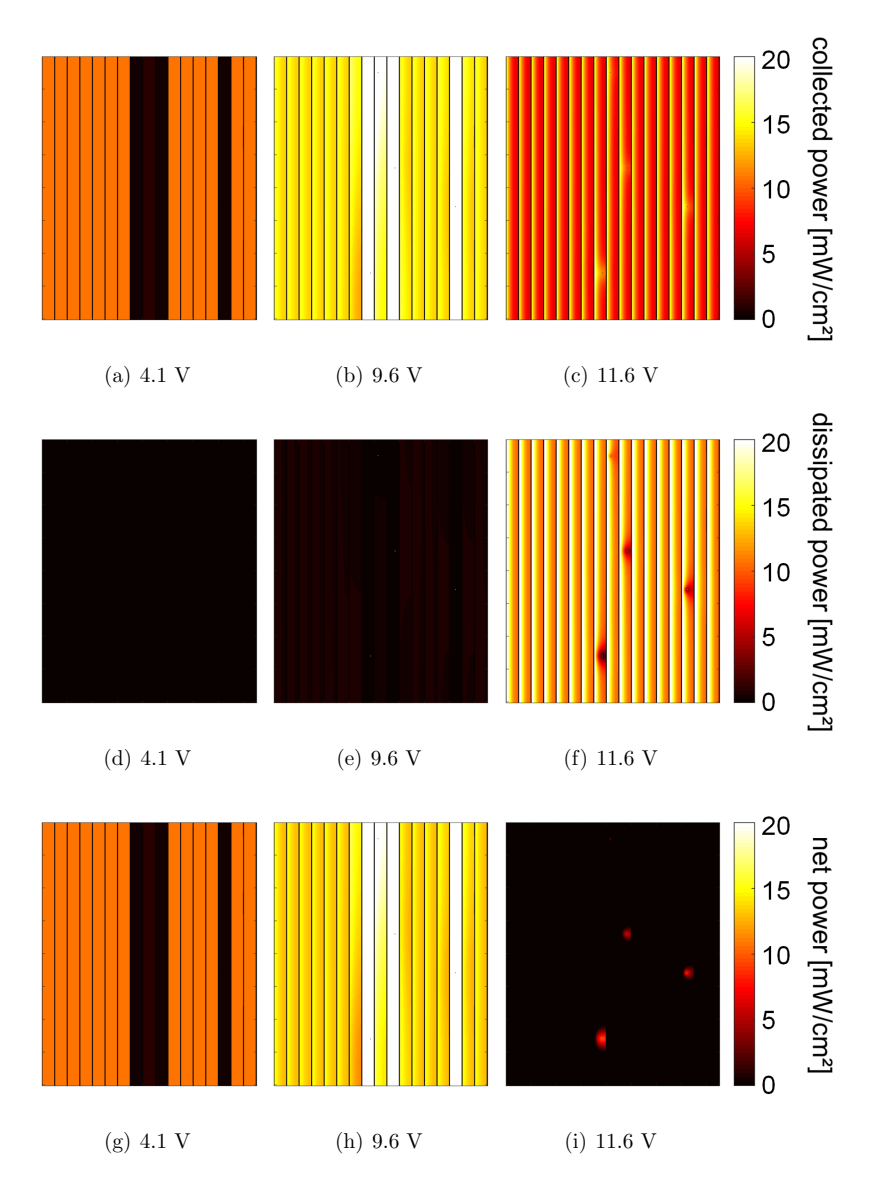


Figure 6.26.: Collected, dissipated and net power images for a defected solar module at different voltages. The net power image result from a subtraction of the dissipated power image from the collected power image.

of the module only plays an important role for the power output of the cell at higher voltages when larger amounts of current start to flow through the module in the dark. Thus, the NP images are defined at low voltages mostly by the photocurrent collection properties.

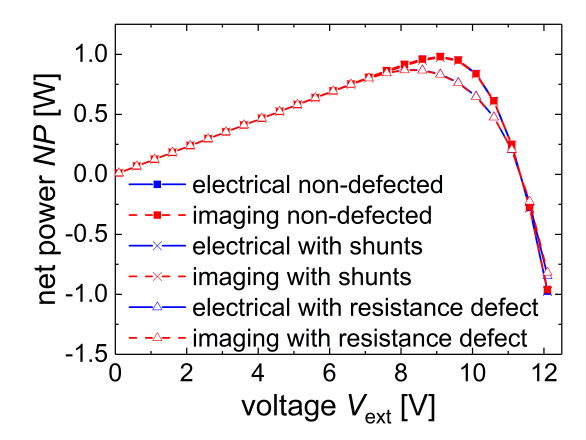


Figure 6.27.: The total power output of two defected simulated solar modules and a non-defected simulated solar module, determined simply from I/V characteristics (blue) and from net power images (red). The overlap shows that the integral over the net power images yields exactly the total power output of the solar modules. The influence of the shunts is nearly not visible.

Similar to the behavior of the cell, we see that from the area around the shunt still positive amounts of power are collected while in the other areas (and of course the shunt itself) power is lost (cf. Figure 6.26 (i)). The results of the net power imaging are in so far important as they show that not only the current collected from shunted cells in the module can be larger than the current collected from non-defected cells but also the final power output of the shunted cells. The loss of performance of a defected module results therefore not from power output loss in the defected cell but rather because the defected cell limits the performance of the remaining cells in the module. It reduces their photocurrent collection properties (cf. Figure 6.24 (e)) and at the same time increases the power dissipated in them as the voltage drop across the shunted cell is decreased and therefore the voltage drop across the remaining cells is increased.

The NP imaging is verified again by comparing the NP images integrated across their area to the external power output of the different modules (Figure 6.27). Additionally to the module with the shunts, the non-defected module and the module where the sheet resistance of one cell was increased were used (cf. Section 6.2.2). Similar to the $F_{\rm pc,glob}$ values a nice overlap for the power values determined from the NP images and the I/V characteristic is obtained. The shunts have little influence on the power output of the solar module, which was

already indicated by the little influence they have on $F_{\rm pc,glob}$. The increased sheet resistance has a larger influence on $F_{\rm pc,glob}$, which is now also seen in the power output of the module. The power output is, as expected less, for the defected modules which does not hold at every voltage for the $F_{\rm pc,glob}$ values. This shows that keeping the dissipated power in mind is important to correctly assess the local quality of a module.

6.4. CIGS Solar Cells

In the final section of this chapter a closer look is taken at the behavior of the photocurrent collection efficiency in CIGS solar cells. We have already seen in the previous section that some special properties of the photocurrent collection efficiency that occur in modules also occur in CIGS modules. However, in this section it is attempted to confirm experimentally that photocurrent collection efficiency images of CIGS samples also reproduce quantitatively what we would expect. To avoid series connection effects, which occur in modules, this analysis focuses on single cells. First, the general behavior of $f_{\rm pc,loc}$ is again shown with a CIGS cell where the series resistance can be easily enhance by disconnecting part of a grid. Afterwards, a homogeneous cell without a grid is used to compare the imaged global photocurrent collection efficiency of a CIGS solar cell to the independently electrically measured global photocurrent collection efficiency. Again, PVMOS simulations are used for the discussion of the results.

6.4.1. Experimental Results

CIGS Cells with a grid

To give a first demonstration that the general principle of $f_{\rm pc,loc}$ imaging also works on CIGS cells, the measured $f_{\rm pc,loc}$ of a cell, which included a grid produced by Bosch CISTech is shown (cf. Section 3.1.4). The cell was measured as it was produced and after part of the grid was disconnected to see how this would influence the $f_{\rm pc,loc}$. It was chosen to image $f_{\rm pc,loc}$ at an operating point of 0.46 V, which is close to the maximum power point of the cell at approximately one sun equivalent illumination. The quantity $\delta V_{\rm ext}$ was chosen to be 0.02 V meaning that the luminescence images used to calculate $f_{\rm pc,loc}$ were taken at an applied voltage of 0.45 V and 0.47 V.

Figure 6.28 shows $f_{\rm pc,loc}$ and EM-PL images taken for the operating point $V_{\rm ext}$ =0.46 V. The EM-PL image 6.28 (a) and $f_{\rm pc,loc}$ image 6.28 (c) show the cell before the contact grid was partly disconnected. The luminescence intensity as well as $f_{\rm pc,loc}$ look mainly homogeneous showing that photocurrent extraction is not limited by local properties. That $f_{\rm pc,loc}$ is still only slightly above 0.6 results from contact and/or bulk resistance that influences the whole cell equally. After

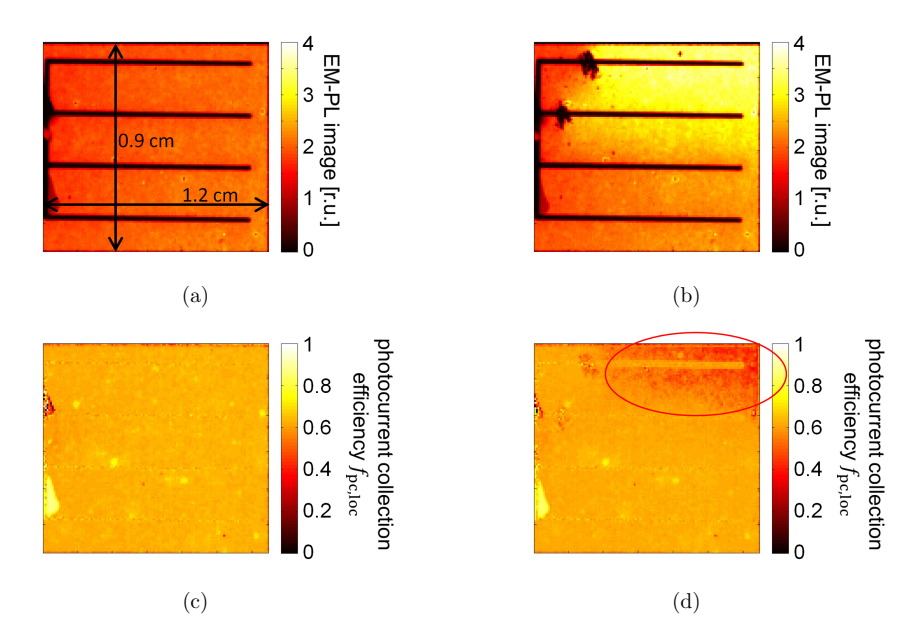


Figure 6.28.: (a) EM-PL image of a $1.2 \times 0.9 \,\mathrm{cm^2}$ CIGS cell (Bosch) with intact grid; (b) EM-PL image of the same cell with the grid broken; (c) differential photocurrent collection efficiency image of the cell with intact grid; (d) differential photocurrent collection efficiency image of the cell with broken grid, all determined at $V_{\rm ext}$ =0.46 V. In the marked area in (d) the decrease of the photocurrent collection efficiency due to the broken grid is clearly visible.

disconnecting the two upper fingers from the contact we can observe from the EM-PL image [Figure 6.28 (b)] that the photocurrent extraction is limited due to the increased resistance. By calculating the $f_{\rm pc,loc}$ image [Figure 6.28 (d)] we see that the differential photocurrent collection is decreased in the area influenced by the broken fingers by up to 0.2.

CIGS Cell without a Grid

After verifying the photocurrent collection efficiency measurement procedure for c-Si solar cells and observing the expected effect of increased series resistance on $f_{\rm pc,loc}$ for CIGS cells, the quantitative behavior of $f_{\rm pc,loc}$ of CIGS cells is analyzed in the following. For the analysis small CIGS cells cut from modules produced by MANZ were used (cf. Section 3.1.4). The cells had no grid and were connected via monolithic interconnection from the neighboring cells.

Figure 6.29 shows $f_{\rm pc,loc}$ images of the CIGS solar cells taken at different external

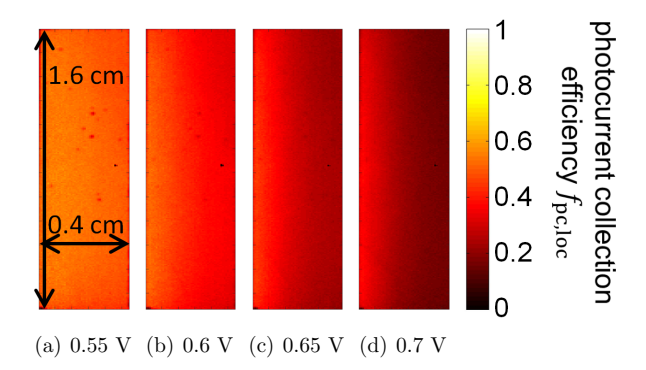


Figure 6.29.: Differential photocurrent collection efficiency images determined for CIGS solar cells produced by MANZ at different V_{ext} .

voltages $V_{\rm ext}$ with $\delta V_{\rm ext}$ =0.02 V. As expected a general decrease of $f_{\rm pc,loc}$ towards higher voltages is seen. Additionally, the change of $f_{\rm pc,loc}$ increases over the width of the cell towards higher voltages. In Figure 6.29 (d) $f_{\rm pc,loc}$ is significantly larger on the left side than on the right. This is seen, as the influence of series resistance effects on $f_{\rm pc,loc}$ increases at higher voltages. The series resistance to the right part of the cell is larger as the photocurrent has to travel the longer distance through the front contact resistance, which is higher than the back contact resistance.

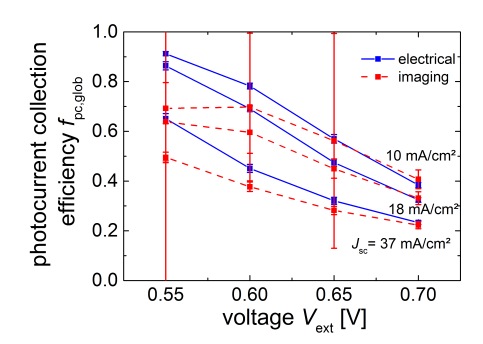


Figure 6.30.: The global differential photocurrent collection efficiency of a CIGS solar cell determined at different illumination conditions (given by the respective short circuit current) plotted against the external voltage. The results in blue are determined from external electrical measurements and the results in red are determined via the averages of the $f_{\rm pc,loc}$ images. The deviations of the two curves at lower voltages show that photocurrent collection efficiency imaging is not working as expected for CIGS solar cells.

The validity of the $f_{pc,loc}$ images is tested with the same procedure that was ap-

plied to the c-Si solar cells. Figure 6.30 shows the global differential photocurrent collection efficiency determined from the images and electrical measurements. At higher voltages around 0.65 V and 0.7 V both measurements yield the same result, which is expected, but at lower voltages both results deviate. It was already mentioned that noise can influence the measurement results and lead to lower determined $f_{\rm pc,loc}$ values. Especially at low voltages and illumination intensity the signal-to-noise ratio decreases. Thus, it was taken a closer look at the voltage dependence of $f_{\rm pc,loc}$.

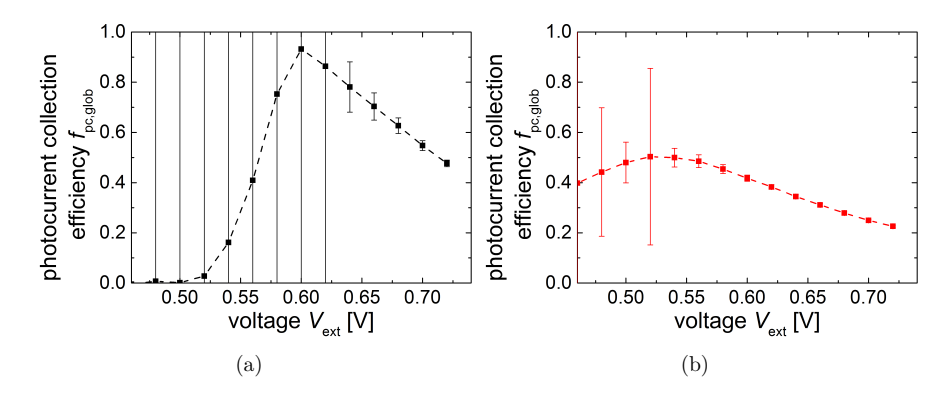


Figure 6.31.: The global differential photocurrent collection efficiency of a CIGS solar cell determined via imaging in the dark (a) and under illumination (b) plotted against the external voltage. The decrease of $f_{\rm pc,glob}$ towards lower voltages looks different depending on the illumination conditions suggesting different causes.

By taking luminescence images of a different sample during a voltage sweep from zero to $0.7\,\mathrm{V}$ in $0.02\,\mathrm{V}$ steps, $f_\mathrm{pc,loc}$ images of the sample are determined at many different voltages using $\delta V_\mathrm{ext} = 0.04\,\mathrm{V}$ this time. The process was performed while the sample was under illumination (1 sun equivalent) and while the sample was kept in the dark. The results are shown in Figure 6.31. Starting at high voltages $f_\mathrm{pc,loc}$ increases at first towards lower voltages, but in both cases $f_\mathrm{pc,loc}$ decreases after a certain voltage point again towards zero. In the dark this decreases is more abrupt than in the light and the results there have a large error leading to the assumption that this drop results from a bad signal-to-noise ratio as describe in Section 6.1.1. Under illumination however the interpretation is less clear. Although the error increases towards lower voltages where $f_\mathrm{pc,loc}$ decreases with decreasing voltage, the behavior looks different compared to the situation in the dark.

The difference is more clearly seen when looking at the actual images. Figure 6.32 shows the luminescence and photocurrent collection efficiency images taken at the first voltage point (seen from large voltages), where $f_{\rm pc,glob}$ starts to decrease

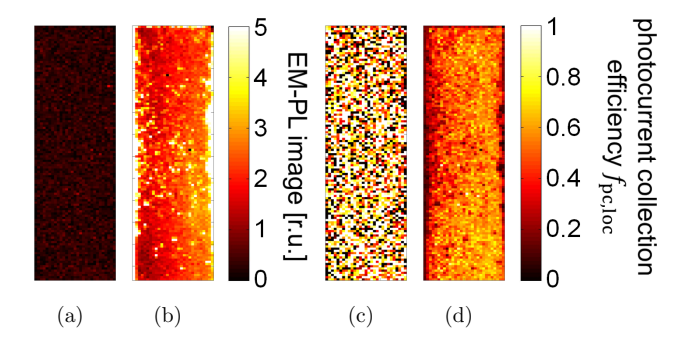


Figure 6.32.: Luminescence images of the analyzed CIGS cell: (a) in the dark at a voltage of 0.58 V; (b) under illumination at a voltage of 0.5 V. (c) and (d) show the corresponding differential photocurrent collection efficiency images. The respective operating points of the images were the voltages at which $f_{\rm pc,glob}$ first started to decrease (seen from high voltages). The $f_{\rm pc,loc}$ image taken under illumination looks much less influenced by noise than the $f_{\rm pc,loc}$ image taken in the dark.

 $(0.58\,\mathrm{V}$ in the dark and $0.5\,\mathrm{V}$ under illumination). The images show that the luminescence intensity in the dark at that voltage is already very low (Figure 6.32 (a)) and therefore also $f_{\rm pc}$ looks very noisy. However, under illumination it is seen that noise plays a much smaller role, as the luminescence intensity is still high and also the $f_{\rm pc}$ image is a lot clearer than the $f_{\rm pc}$ image in the dark. Still, the $f_{\rm pc,glob}$ of the image under illumination is decreased compared to the $f_{\rm pc,glob}$ of the image taken at a higher voltage.

Comparison of Calculation Methods

As luminescence images of a CIGS sample were taken at several voltage steps the results of the preceding paragraph are used to compare the two different calculation methods of $f_{\rm pc,loc}$ images discussed in Section 6.1.1 (cf. Equation 6.5 and 6.6). Figure 6.33 shows the $f_{\rm pc,loc}$ images determined for $V_{\rm ext}$ =0.6 V with the log- and lin-method and with varying $\delta V_{\rm ext}$. The images calculated with the log-method are nearly not influenced at all by the change of $\delta V_{\rm ext}$. In contrast the images determined with the lin-method are more influence by the choice of $\delta V_{\rm ext}$, as there $f_{\rm pc,loc}$ increases with $\delta V_{\rm ext}$, especially on the left side of the cell. This is expected from Equation 6.7 as on the left side $f_{\rm pc,loc}$ is already slightly larger in the first place and the error increases with $f_{\rm pc,loc}$ and $\delta V_{\rm ext}$.

For a more detailed analysis $f_{\rm pc,glob}$ was calculated. Figure 6.34 shows $f_{\rm pc,glob}$ as a function of $V_{\rm ext}$ and $\delta V_{\rm ext}$. We see that at high voltages where $f_{\rm pc,glob}$ is lower the error resulting from the linear approximation is reduced. At lower voltages the error increases and a significant influence of $\delta V_{\rm ext}$ on the measurement results

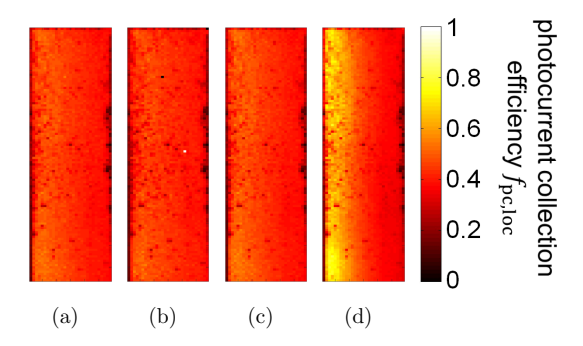


Figure 6.33.: $f_{\rm pc,loc}$ images determined for $V_{\rm ext}$ =0.6 V using the log- and lin-method using different $\delta V_{\rm ext}$. (a) and (b) using the log-method and $\delta V_{\rm ext}$ =0.04 V or $\delta V_{\rm ext}$ =0.2 V, respectively. (c) and (d) using the lin-method and $\delta V_{\rm ext}$ =0.04 V or $\delta V_{\rm ext}$ =0.2 V, respectively. The lin-method is more sensitive to the choice of $\delta V_{\rm ext}$.

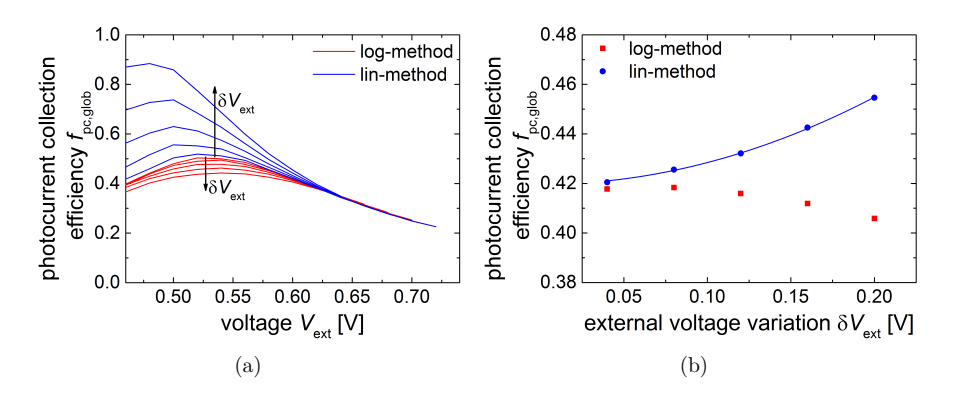


Figure 6.34.: (a) Comparison of the voltage dependence of $f_{\rm pc,glob}$ calculated from images that were determined with the log- and lin-method (red and blue, respectivly). In the direction of the arrow $\delta V_{\rm ext}$ was varied from 0.04 V to 0.2 V in 0.04 V steps. (b) The behavior of $f_{\rm pc,glob}$ determined with the two different methods at $V_{\rm ext}$ =0.6 V with changing $\delta V_{\rm ext}$. The blue line is a quadratic fit that shows the quadratic dependence of $f_{\rm pc,glob}$ determined via the lin-method on $\delta V_{\rm ext}$.

is seen. We also see a small influence of $\delta V_{\rm ext}$ on the images determined with the log-method. In contrast to the lin-method an increase of $\delta V_{\rm ext}$ reduces $f_{\rm pc,glob}$ for the log-method. The effect is easily understood as increasing $\delta V_{\rm ext}$ increases the finite step size that is used for the determination of the gradient, which is $f_{\rm pc}$. This makes the determination of $f_{\rm pc}$ less accurate.

Total Photocurrent Collection Efficiency

Up to now the experiments focussed on the differential photocurrent collection efficiency. The total photocurrent collection efficiency was also tested for the CIGS solar cells. However, as the differential photocurrent collection efficiency could not be verified at low voltages (cf. Figure 6.30) it is expected that also the $F_{\rm pc,loc}$ imaging leads to results contradicting external electrical measurements.

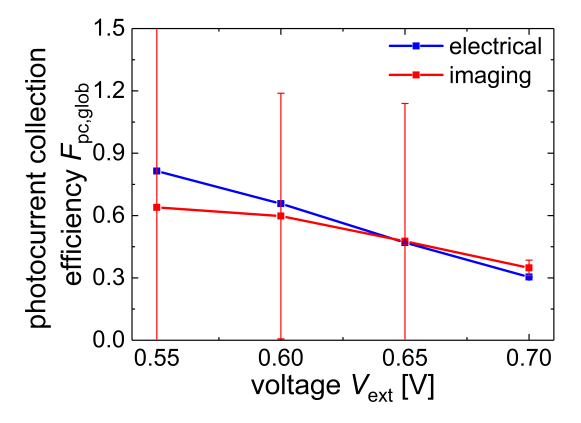


Figure 6.35.: The global total photocurrent collection efficiency of a CIGS solar cell determined for a short circuit current density of $37\,\mathrm{mA/cm^2}$ plotted against the external voltage. The results in blue are determined from external electrical measurements and the results in red are determined via the averages of the $F_{\mathrm{pc,loc}}$ images. As there is no clear overlap between the two curves, photocurrent collection efficiency measurements seem to be problematic for CIGS solar cells. The errors for the imaged photocurrent collection efficiency are so large at lower voltages due to influences of very noisy differential photocurrent collection efficiency images determined at low illuminations. It is expected that the results are more accurate than the error bars indicate.

For the sake of completeness Figure 6.35 shows the $F_{\rm pc,glob}$ values calculated via imaging and electrical measurements for several voltages. Indeed, the $F_{\rm pc,glob}$ computed from imaging is inaccurate and deviates from the $F_{\rm pc,glob}$ determined from electrical measurements. We observe that for low voltages the $F_{\rm pc,glob}$ from the imaging is underestimated while above 0.65 V $F_{\rm pc,glob}$ is overestimated. This was already indicated by the bad overlap of the $f_{\rm pc,glob}$ results and is therefore not

surprising. In the following it will be discussed if the discrepancy can be explained by effects resulting from larger noise at lower voltages.

6.4.2. Simulations and Discussion

In this section the discrepancy between the imaged photocurrent collection efficiency and electrical measurement is discussed with the use of PVMOS simulation. In the experiments a decrease of $f_{\rm pc,glob}$ towards lower voltages is seen, which is not expected by any model based on an one or two-diode equivalent circuit network. A possible reason for this is noise, as lower voltages lead to a lower signal and therefore more values for which the photocurrent collection efficiency cannot be reliably determined. However, in the illuminated case it was unclear if all of the decrease can be explained purely by noise.

To understand the effect better the expected noise was added to simulation results. Meaning that from a simulated voltage image first a luminescence image was calculated with Equation 3.3. The proportionality constant was chosen so that the simulated luminescence intensity was roughly equal to the experimentally measured luminescence intensity. To this luminescence signal a constant background value of 20000, which is in the same order of magnitude of the background of the camera, was added. In reality this value can vary across the image. In principle the constant part is not important as in the simulations and the experiment it is removed by a background image subtraction. However, it is important for the noise calculations. The camera signal is assumed to be normal distributed with a mean equal the luminescence signal plus the background signal and a standard deviation equal to the square root of this sum. Thus, the added background means that the noise can be a lot larger than the luminescence signal at low voltages.

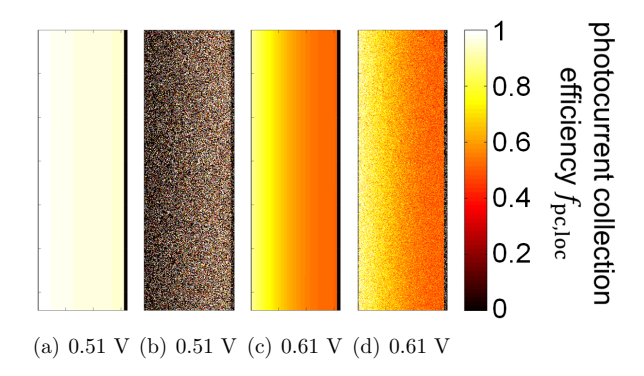


Figure 6.36.: Simulated photocurrent collection efficiency images under illumination at different voltages without [(a) and (c)] and with [(b) and (d)] additionally added noise. The noise influences the measurement result more at lower voltages.

For the PVMOS model a cell was designed which had the same geometric properties as the CIGS cell from MANZ analyzed in the previous section. The electrical properties of the cell are given in Table 3.6. In Figure 6.36 $f_{\rm pc,loc}$ images are shown with and without the added noise at two different voltages, for the simulated cell. As expected the influence of noise on the results is more important at lower voltages.

To analyze the results again more quantitatively Figure 6.37 shows the global photocurrent collection efficiency calculated from the images influences by the noise. The behavior looks very similar to Figure 6.31 (a) as the $f_{\rm pc,glob}$ drops very steeply after a certain voltage, strengthening the assumption that such a behavior is caused by noise. However, the simulation was performed with illumination and in the experiment that lead to the result seen in Figure 6.31 (b). In this figure a less abrupt decrease of $f_{\rm pc,glob}$ with decreasing voltage is seen. This behavior cannot be reproduced by artificial noise added to simulations.

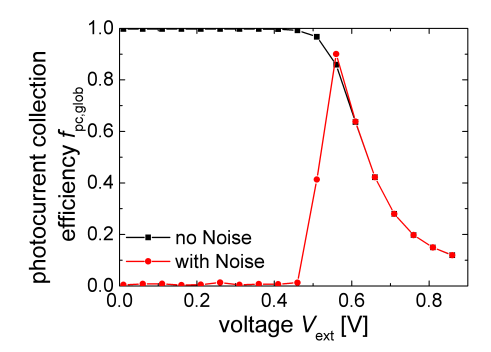


Figure 6.37.: The quantity $f_{pc,glob}$ calculated from $f_{pc,loc}$ images at different voltages for a simulated solar cell under illumination with and without added noise. The noise leads to an abrupt drop of the photocurrent collection efficiency when measured below a certain voltage. The drop was similar for experiments in the dark but looked different for experiments under illumination (cf. Figure 6.31).

The same result is also seen by comparing Figure 6.36 (d) and 6.32 (d). Both images are similarly influenced by noise, but while the experimental one already shows a decrease in $f_{\rm pc,glob}$ this is not seen for the simulated image. Here, $f_{\rm pc,glob}$ is close to the simulated result without added noise. Thus, the decrease of $f_{\rm pc,glob}$ towards low voltages in the experiments determined under illumination for the CIGS solar cells is not a measurement artifact resulting from a bad signal to noise ratio, but is rather connected directly to the properties of the solar cell.

That the imaged $f_{\rm pc}$, which is determined by $dV_{\rm j}/dV_{\rm ext}$, decreases towards lower voltages suggests that the voltage drop across a series resistance rises, while the external voltage decreases. This rise of a voltage drop across a series resistance under the nearly constant current, which flows under illumination at low voltages,

can only be resulting from a series resistance that increases with decreasing external voltage. Such a behavior for the series resistance was already observed in [103] for thin-film silicon solar cells. Thus, the behavior of the series resistance for CIGS solar cells will be analyzed in Chapter 7 and the role of the series resistance for the photocurrent collection efficiency imaging will be discussed in detail (Section 7.4).

6.5. Conclusion

This chapter introduces the recently developed concept of the differential photocurrent collection efficiency, shows how it can be imaged with luminescence, and explains how its behavior yields valuable information about a solar cells local properties. The method is extended to provide the total local photocurrent collection efficiency that is directly linked to a solar cells dark and light current/voltage characteristic. Additionally, it is discussed how a total local photocurrent collection efficiency image can be used to provide a net power image, which describes exactly the contribution a local region has on the power output of a solar cell.

The photocurrent collection efficiency methods are first experimentally verified with a crystalline silicon solar by comparison with independent electrical measurements of the global photocurrent collection efficiency and it is shown how an obtained total photocurrent collection efficiency image may be used to calculate collection losses from certain regions. Afterwards, with the use of PVMOS the differential photocurrent collection efficiency measurements are verified also on local scale. Furthermore, PVMOS simulations are used to explain the influence of various defects on the photocurrent collection efficiency images in more detail and to demonstrate the concept of net power imaging.

Afterwards the imaging methods are extended towards modules. It is shown experimentally and in simulations that the photocurrent collection properties are influenced by the series connection. The series connection of cells leads to a shunted cell being able to collect more photocurrent than the non-shunted cells of the same module at specific operating points. A model was developed to explain this result. Further simulations of the total photocurrent collection efficiency and net power images of modules reveal that in a module a defected cell may contribute even more to a solar modules performance than the remaining cells. This complicates, the interpretation of the presented imaging techniques for outdoor measurements where solar cells are connected in series to modules and strings. Each cell influences the performance of the complete module, and cells which provide the largest power output might be actually be the ones limiting the performance of other cells ultimately reducing the power output of a module.

In the final section of this chapter, photocurrent collection efficiency imaging was tested also for CIGS solar cells by comparing the images to independent electrical measurements of the global photocurrent collection efficiency. Although the

general properties seem to be the same, the viability of photocurrent collection efficiency measurements for CIGS solar cells could not be confirmed as the electrical measurements were different to the imaging results. The global differential photocurrent collection efficiency imaged for CIGS solar cells decreases towards lower voltage, which was not seen in the electrical measurements. PVMOS simulations cannot explain the discrepancies with noise influencing the imaging procedure. Therefore, it is assumed that special material properties of CIGS solar cells are in conflict with the equivalent circuit network assumed for the development of photocurrent collection efficiency imaging. A possible cause could be the presence of an injection dependent series resistance. The idea behind such a series resistance and its influence on the imaging methods used in this work is discussed in detail in the following chapter.

7. Injection Dependent Series Resistance in CIGS

In the two previous Chapters 5 and 6 the luminescence imaging experiments of CIGS samples showed effects that could not be explained. In Chapter 5 it was seen that the EL characteristics may significantly differ from EM-PL characteristics at low injected currents, while in Chapter 6 a decrease of the differential photocurrent collection efficiency was seen towards low voltages. Additionally, the imaged photocurrent collection efficiency values deviated from the electrically measured ones. These effects could not be reproduced with simulations based on one or two diode models or a network of them.

A possible property of the CIGS samples that would not be included in such models is an injection dependent series resistance. It was shown in [103] how the series resistance changes depending on the applied voltage for thin film silicon solar cells. In this chapter it is shown that a similar behavior of the series resistance can be observed for CIGS solar cells, as the series resistance will be measured under different operating conditions using luminescence images. Afterwards, device simulations with the program SCAPS will be used to analyze the injection dependence of the series resistance in detail and to explain its origin in the solar cell stack. Finally, an equivalent circuit model is proposed that includes the found characteristics of the series resistance. This model is subsequently used to explain the special features seen in the luminescence measurements for the CIGS samples in the previous chapters.

7.1. Theory

The electrical resistivity $\rho_{\rm c/v}$ of materials depends on the number of free charge carriers $n_{\rm e/h}$ and their mobilities $\mu_{\rm e/h}$ and reads

$$\rho_{\rm c/v} = \frac{1}{e\mu_{\rm e/h}n_{\rm e/h}} \tag{7.1}$$

The mobility of a semiconductor is expected to stay mostly constant. The number of free charge carriers in the bands of a semiconductor depends on the density of states and exponentially on the positioning of the quasi-Fermi level (cf. Equation 2.1a), which means that the number of free charge carriers changes depending on illumination or applied voltage. Thus, the resistance of a solar cell is dependent

on the injection conditions. Whether an injection dependent resistant is relevant for the effective resistance of a solar cell depends on it magnitude compared to other resistances of solar cells.

The Distributed Nature of the Bulk Series Resistance

For the determination of injection dependent series resistance measurements of the junction voltage were used. From the junction voltage the series resistance was calculated as described in Section 3.1.3 and Equation 3.6. In the following it is discussed in more detail how the series resistance determined in that way is actually related to the local resistivities described by Equation 7.1.

As mentioned in Section 2.4.1 the junction voltage describes the average quasi-Fermi level splitting through the depth z of a device. Thus, we write

$$V_{\rm j} = \frac{\int_0^d (E_{\rm fn}(z) - E_{\rm fp}(z)) dz}{ed}.$$
 (7.2)

The change in the quasi-Fermi levels is depending on the local currents $J_{\rm e/h}$ and resitivities $\rho_{c/v}$ (cf. Equation 2.3a and 2.3b). Their product $J_{\rm e/h}\rho_{c/v}$ describes the bending of the quasi-Fermi levels and therefore the position of the quasi-Fermi levels at z is obtained by integrating over $J_{\rm e/h}\rho_{c/v}$ from the edges of the device to z. It follows for the quasi-Fermi level splitting

$$\frac{E_{\rm fn}(z) - E_{\rm fp}(z)}{e} = V_{\rm ext} - \int_{z}^{d} J_{\rm e}(z') \rho_{\rm c}(z') dz' - \int_{0}^{z} J_{\rm h}(z') \rho_{\rm v}(z') dz'. \tag{7.3}$$

In other words, $J_{e/h}\rho_{c/v}$ describes the voltage loss per distance z due to the resistance of the conduction/valence band. By inserting Equation 7.3 into Equation 7.2 and subtracting the external voltage we obtain the voltage loss $V_{\rm Rs}$ due to series resistance as assumed by the determination via luminescence

$$V_{\rm Rs} = \frac{\int_0^d \left(\int_z^d J_{\rm e}(z') \rho_{\rm c}(z') dz' + \int_0^z J_{\rm h}(z') \rho_{\rm v}(z') dz' \right) dz}{d}$$
(7.4)

This voltage loss across the series resistance $V_{\rm Rs}$ divided by the total current through the device yields the effective series resistance as measured by luminescence.

Equation 7.4 shows that not only the local resistivities are relevant for the effective series resistance but also the local currents. Thus, the influence of large resistivities, which usual affect minority carrier transport due to the lower number of free charge carriers, on the effective resistance depends also on the amount of current flowing as minority charge carriers.

7.2. Experimental Results

The measurements of the total series resistance were performed on the same CIGS solar cells produced by MANZ, which were already used in Section 6.4.1. Luminescence images were taken of the sample at 0.02 V steps between zero and 0.72 V simultaneously with current voltage characteristics. From the images the junction voltages were calculated as described in Section 3.1.3. However, with the assumption that an increase of the series resistance takes place towards lower voltages, we can no longer expect that the junction voltage is zero under short circuit conditions. Thus, no short circuit image was subtracted from the luminescence images taken under illumination and instead just a background image taken in the dark was used. From the local junction voltage images then the effective cell junction voltage was determined from the average across the cell area and from that effective junction voltage the effective series resistance was calculated.

Figure 7.1 shows the J/V and $J/V_{\rm j}$ characteristics determined for an example cell. The difference between the curves is always showing the voltage loss across a series resistance. The junction voltage $V_{\rm j}$ is smaller than the external voltage $V_{\rm ext}$ in the dark and larger under illumination, due to the direction of the respective current flow.

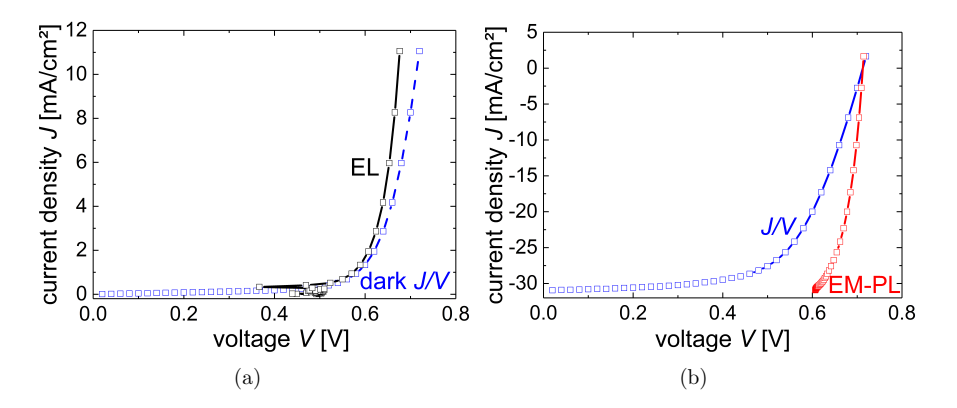


Figure 7.1.: J/V and J/V_j characteristics of a CIGS solar cell. (a) in the dark, (b) under illumination. From the difference between the two curves and the respective current the series resistance can be determined depending on the injection conditions.

From the characteristics the total series resistance $R_{\rm s}$ is calculated using Equation 3.6. The results are shown in Figure 7.2 on a linear and logarithmic scale. Both in the dark and under illumination the series resistance decreases significantly with increasing voltage. In the dark the decrease is exponential which was already seen in [103] for thin-film silicon solar cell. In that work the series resistance was not determined under illumination. Here, we see that the decrease

of the series resistance under illumination with increasing voltage is more linear and that the starting resistance at zero voltage is much lower. The resistance in the dark could not be measured at lower voltages as the bad signal to noise ratio at low voltage does prevent a clear determination of the junction voltage. In the dark and the illuminated case the series resistance seems to approach a constant value of about $3.5\,\Omega\mathrm{cm}^2$ at larger voltages. The difference under illumination and in the dark underlines the injection dependence of the analyzed series resistance.

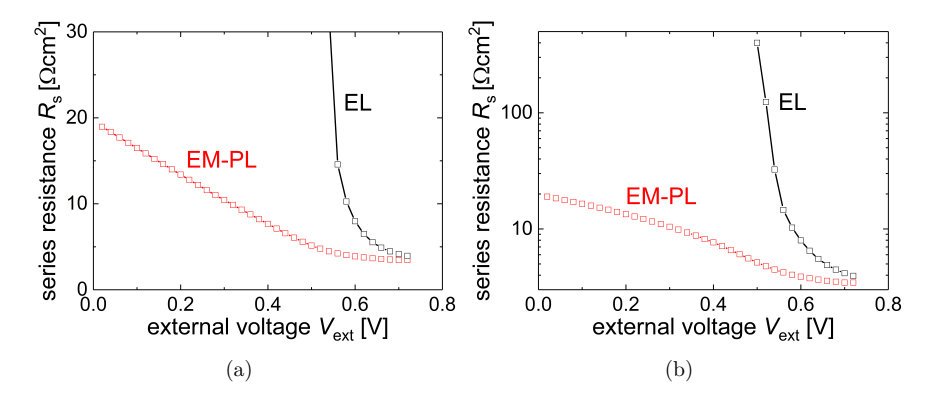


Figure 7.2.: Injection dependent series resistance measured using luminescence under illumination (red) and in the dark (black). (a) plotted using a linear y-axis, (b) plotted using a logarithmic y-axis. In the dark the resistance decreases exponentially with the applied voltage while under illumination the decrease is rather linear.

7.3. SCAPS Modelling

In order to demonstrate that the explanation of an injection dependent series resistance with transport through the semiconductor bands is viable, a CIGS solar cell was modeled using the 1-D device simulator SCAPS. Additionally, various parameters of the model were systematically altered to better understand the effect responsible for injection dependent series resistance. As the base parameter set, the set describing the light soaked solar cell given in Section 3.2.1 (Table 3.5) was used. The series resistance was determined as discussed in Section 3.2.1 from the simulated total luminescence signal. This approach is very similar to the approach used in the experiments.

In Figure 7.3 the energy-band profile under illumination at short circuit and forward bias (0.6 V) of the simulated device (without ZnO) is shown. A large shift of the electron quasi-Fermi level is seen due to the illumination, which shows that not all generated charge carriers are collected even at short circuit. Furthermore, we observe a gradient of the quasi-Fermi levels close to the junction that indicates

voltage losses due to the transport of the charge carriers through the semiconductor. This gradient is reduced at a forward bias as the current decreases and therefore transport losses decrease as well.

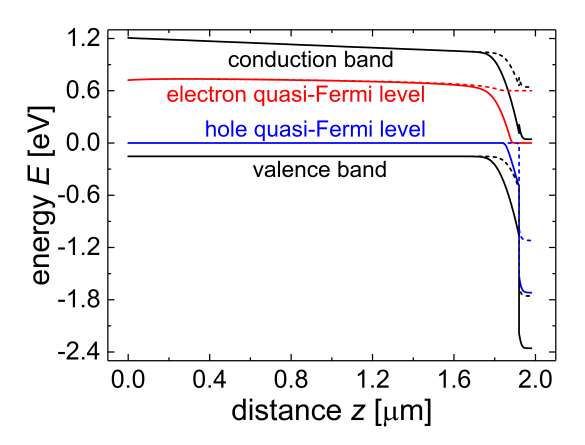


Figure 7.3.: Energy-band profile of the simulated CIGS solar cell, without the ZnO layers, under illumination at short circuit (solid line) and at an applied bias of 0.6 V (dashed line). The electron quasi-Fermi level is shifted up due to the illumination and incomplete charge carrier extraction. The band bending indicates voltage losses.

Figure 7.4 shows the simulated J/V characteristic and series resistance with and without ZnO front contact. For the simulations under illumination, the illumination was adjusted so that the short circuit current is similar to the one measured in the experiments. For that the intensity had to be set to $580\,\mathrm{W/m^2}$, as a similar spectrum to the experiment was used (800 nm with a linewidth of 5 nm). It is clearly visible that the behavior of the series resistance in the simulations shows a very similar behavior to the experimentally measured one. Under illumination it decreases linearly with the external voltage and in the dark it decreases exponentially. At large voltages the series resistance approaches the constant external resistance. This underlines that the measured series resistance shows properties of a solar cell that are also included within the SCAPS simulation.

To better locate the origin of the series resistance the front contact ZnO layers were removed from the simulations to see if that influences the simulations results. As visible in Figure 7.4 the influence of the front contact on the series resistance is minor. Only the short circuit current increases a bit, due to the reduced parasitic absorption. Thus, the injection dependence of the series resistance needs to result from either the CdS or the CIGS layer.

Due to Equation 7.1, we know that the mobility of the different bands should influence the series resistance if it results from the transport of charge carriers through the band. Thus, the in-depth analysis of the system is started by varying the different mobilities of the device. First the electron mobility of the CdS layer

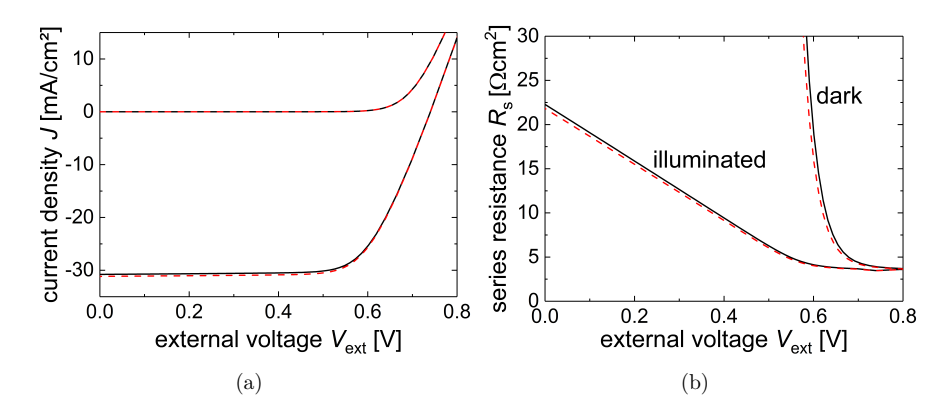


Figure 7.4.: (a) J/V characteristics of a simulated CIGS solar cell with ZnO front contact (black, solid) and without ZnO front contact (red, dashed). (b) Series resistance of the simulated solar cell with ZnO front contact (black, solid) and without ZnO front contact (red, dashed).

was varied from $5 \,\mathrm{cm^2/Vs}$ to $85 \,\mathrm{cm^2/Vs}$ in $20 \,\mathrm{cm^2/Vs}$ steps. This variation had no significant influence on the results (cf. Appendix B). The electron density in the conduction band of the CdS is so large and the layer itself so thin that its resistance becomes negligible, independent of the mobility (cf. Equation 3.6).

Thus, after ensuring that the CdS does not have a significant effect on the series resistance, the mobilities in the CIGS are altered. Figure 7.5 (a) and (b) show how different electron mobilities influence the J/V characteristic and series resistance of the solar cell. Decreasing the electron mobility significantly increases the series resistance of the device, and due to it also the short circuit current decreases.

Compared to that, changes in the hole mobility in the CIGS have a negligible effect on the J/V characteristics and the series resistance (cf. Figure 7.5 (c) and (d)). Even decreasing the hole mobility by more than an order of magnitude has no effect, although in the larger region of the CIGS bulk current is carried by holes. This result shows that the hole density is so large that even low hole mobilities do not increase the resistance of the valence band above the resistance resulting from the conduction band. Therefore, the injection dependence of the series resistance seems to result primarily from the transport of electrons through the conduction band of the solar cell.

In the following parameters are altered that affect the free electron density in the CIGS, as a change in the carrier density should also influence the series resistance (cf. 7.1). In Figure 7.6 the band gap and the valence and conduction band density of states were varied and their influence on the J/V characteristics and the series resistance is shown. The changes in the bandgap [Figure 7.6 (a) and (b)] mainly result in a change of the $V_{\rm oc}$ of the device. The series resistance curve is shifted in

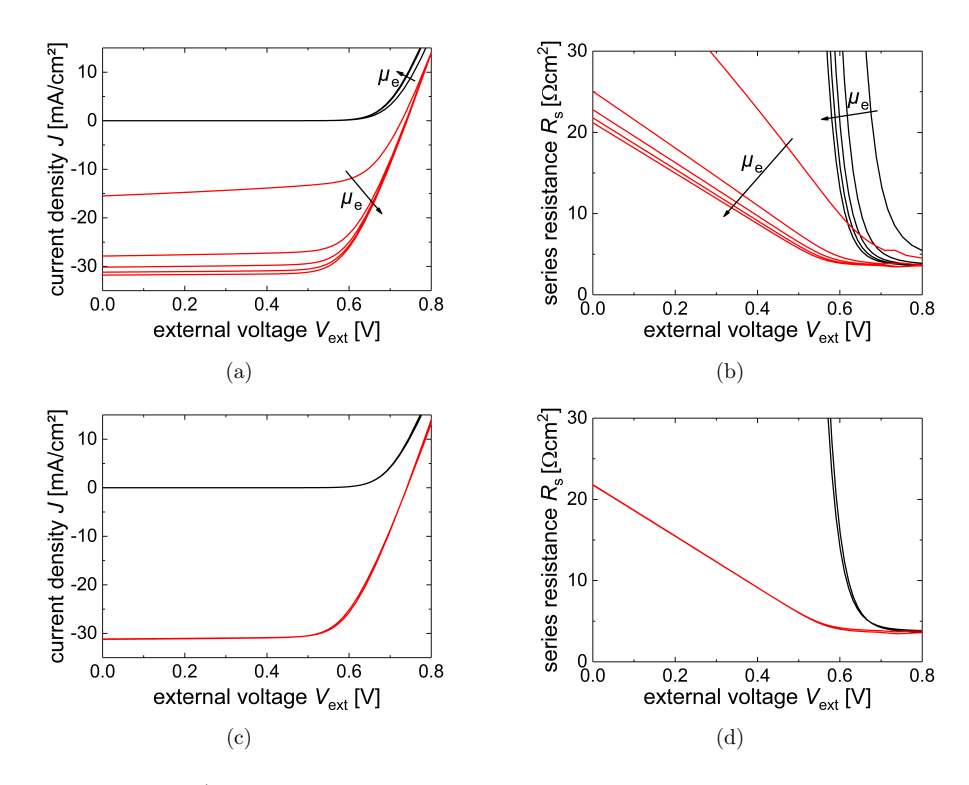


Figure 7.5.: J/V characteristics and series resistance simulated with varying mobilities in the dark (black) and under illumination (red): (a),(b) electron mobility varied from $1 \text{ cm}^2/\text{Vs}$ to $81 \text{ cm}^2/\text{Vs}$ in $20 \text{ cm}^2/\text{Vs}$ steps; (c),(d) hole mobility varied from $0.1 \text{ cm}^2/\text{Vs}$ to $80.1 \text{ cm}^2/\text{Vs}$ in $20 \text{ cm}^2/\text{Vs}$ steps.

the voltage direction with each step of the bandgap by the amount of the bandgap step. An increase of the bandgap leads to a decrease of the electron density in the CIGS, which increases its resistance. The electron density reduction can be offset by an increase of the external voltage resulting in the shifting of the resistance curves.

An increase in the conduction and valence band density of states both lead to a decrease of the open circuit voltage and the series resistance [Figure 7.6 (c)-(f)]. The influence of the density of states in the conduction band influences the series resistance more, which is obvious as it influence the electron density in the conduction band (cf. Equation 2.1a). However, it is less obvious why the density of state in the valence band influences the series resistance. As CIGS is a p-type material the doping determines the amount of holes in the valence band. The Fermi-energy is determined by the number of holes and the valence band

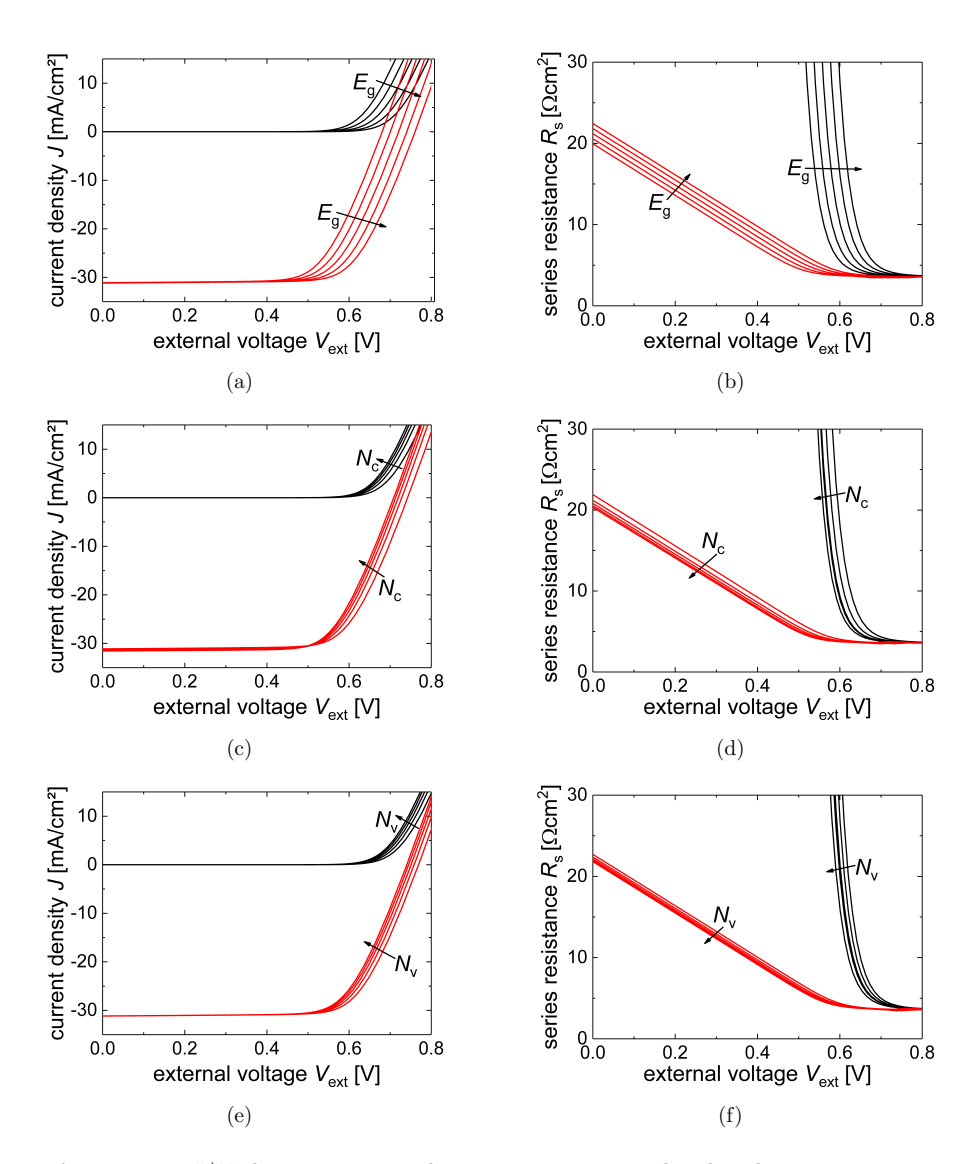
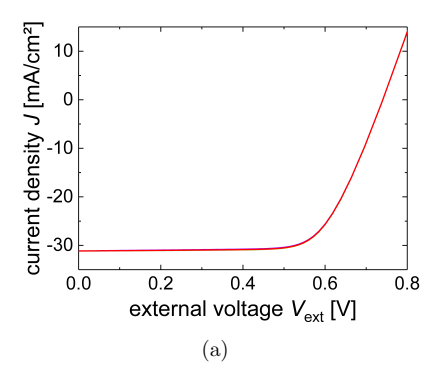


Figure 7.6.: J/V characteristics and series resistance simulated with varying parameters in the dark (black) and under illumination (red): (a),(b) Bandgap varied from 1.3-1.1208 eV to 1.38-1.2008 eV in 0.02 eV steps (the grading was kept constant); (c),(d) conduction band density of states varied from $2\times10^{18}\,\mathrm{cm}^{-3}$ to $10^{19}\,\mathrm{cm}^{-3}$ in $2\times10^{18}\,\mathrm{cm}^{-3}$ steps; (e),(f) valence band density of states varied from $0.6\times10^{19}\,\mathrm{cm}^{-3}$ to $1.8\times10^{19}\,\mathrm{cm}^{-3}$ in $0.3\times10^{19}\,\mathrm{cm}^{-3}$ steps.

density of states according to Equation 2.1b. Therefore, an increase of the valence band density of states shifts the Fermi-level upwards if the number of holes is fixed by the doping. The upward shifting of the Fermi-level changes in the following the density of electrons in the conduction band, which influences in turn the series resistance.

Equation 7.1 describes how the series resistance of a device is influenced by its mobilities and charge carrier densities. However, as discussed Section 7.1 the effective resistance of a device as it is measured is not only depending on local resistance properties but also on the local current densities (cf. Equation 7.4). This dependency on local current densities is demonstrated by simulating the series resistance of the CIGS device under varying illumination spectra. By decreasing the wavelength of the illuminating spectrum, the light is absorbed closer to the pn-junction and the generated electrons have to travel a shorter distance through the conduction band of the device. This variation should decrease the effective series resistance measured, as the overall current is carried more by holes traveling through the valence band of the device, which has a significantly smaller resistance.



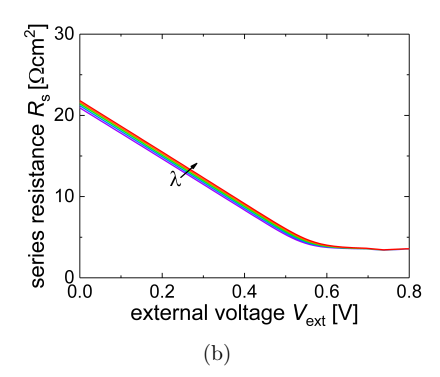
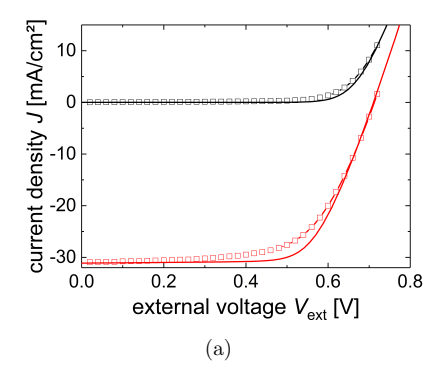


Figure 7.7.: J/V characteristics (a) and series resistance (b) simulated with varying illumination wavelength. The wavelength was varied between 400 nm and 700 nm in 100 nm steps. The intensity of the of illumination was also varied so that the device stayed at approximately the same short circuit current.

The results of simulations, where the illumination spectrum was change from $400 \,\mathrm{nm}$ and $700 \,\mathrm{nm}$ in $100 \,\mathrm{nm}$ steps are shown in Figure 7.7. As the total absorption of the device depends on the wavelength, the illumination intensity for the different wavelength was adjusted so that the overall short circuit current density stayed constant. This variation of the intensity ensured similar overall electron densities in the device, so that the resulting differences of the series resistance actually result from different (shorter) current paths through the conduction band. There is no significant influence seen of the illumination wavelength for the J/V characteristic. However, as expected the series resistance shows indeed a decrease

with decreasing illumination wavelength.

Now, that it is known how different parameters take effect it is possible to adjust the cell parameters so that the simulation results better fit to the experimental results. The outcome of the adjustment of the SCAPS model to the experimental results is shown in Figure 7.8. It was chosen to decrease the bandgap by $30\,\mathrm{mV}$, as it decreases the $V_{\rm oc}$ and series resistance of the device, without influencing the rest to much. Optimizing all parameter is not done due to the amount of possible parameters and interdependencies. The shown adjustment of the parameters confirms that a reasonable set of parameters exists that fits to the experimental results and explains the experimental finding of the injection dependent series resistance.



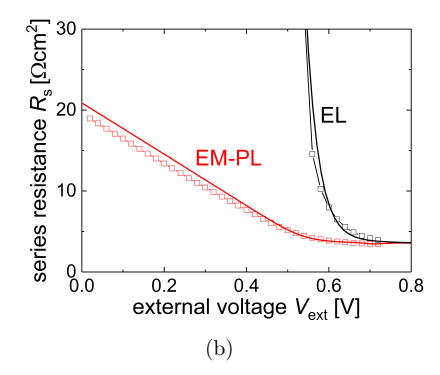


Figure 7.8.: Experimentally measured (squares) J/V characteristics (a) and series resistance (b) compared to simulated results using SCAPS (line). The results show that the injection dependence of the series resistance can be explained by reasonable set of solar cell simulation parameters.

7.4. Equivalent Circuit Model

To analyze the influence an injection dependent series resistance has on electrical and luminescence measurements, an equivalent circuit model is developed that includes the properties of the found resistance. Using such a model it is easier to develop mathematical descriptions of the found effects. The new equivalent circuit is based on the simple one diode model that is introduced in Section 2.2. The difference is that its series resistance is no longer simply ohmic, but injection dependent. As a formula to describe the injection dependence, formula (16) from [103] is used and adjusted (a similar form was also proposed in [112]). The equation reads

$$R_{\rm s} = R_{\rm c} + R_0 \times \exp\left(-\frac{eV_{\rm j}}{n_{\rm id}kT}\right).$$
 (7.5)

Here, $R_{\rm c}$ is a constant ohmic resistance, describing the standard series resistance resulting from contacts or the like, and R_0 is a parameter determined by the material properties of the CIGS, like the mobility, but also by the dominating current paths through the device (cf. Section 7.1 and 7.3). The exponential term including the junction voltage describes the injection dependence of the series resistance as it mirrors the change of the charge carrier density with the operating point. The ideality factor $n_{\rm id}$ used here is equal to the ideality factor of the diode.

The adjustment to the original equation was that the junction voltage is used in the exponential term instead of the total device voltage. This substitution was done to implement the observed decrease of the series resistance under illumination. Due to the series resistance, the junction voltage is increased under illumination compared to a situation in the dark with the same external device voltage. This will reduce the series resistance under illumination.

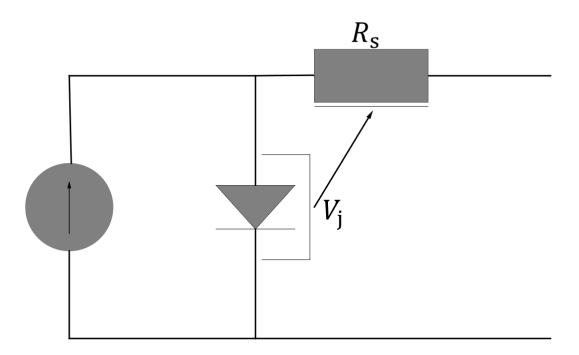
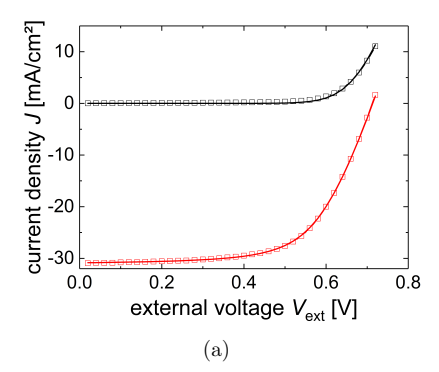


Figure 7.9.: Sketch of an equivalent circuit including an injection dependent series resistance. A one diode model is altered in a way that makes its series resistance R_s depending on the junction voltage V_i across the diode.

A sketch of the new equivalent circuit is shown in Figure 7.9. A shunt is not considered, yet. It's influence on the results will be discussed in a later paragraph.

The equivalent circuit was solved using a bisection method [113]. The dark and illuminated J/V characteristic of the equivalent circuit were fitted simultaneously automatically to the experimental results using the simplex search method implemented in Matlab [114] to see how well the equivalent circuit reproduces the results.

Figure 7.10 shows the fitting results. We see that especially the J/V characteristics but also the corresponding series resistances are reproduced well by the new equivalent circuit. The exponential decrease of the series resistance with the voltage in the dark and the linear decrease under illumination are clearly visible. The found fitted parameters are $J_0=9.31\times10^{-8}\,\mathrm{mA/cm^2}$, $R_0=6.9\times10^7\,\Omega\mathrm{cm^2}$, $R_c=3.26\,\Omega\mathrm{cm^2}$, $n_{\mathrm{id}}=1.4$, and $J_{\mathrm{sc}}=31.3\,\mathrm{mA/cm^2}$. In the following, the unexplained



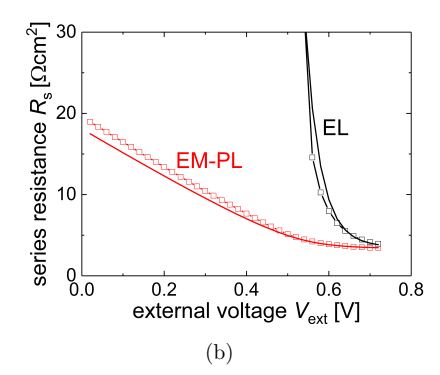


Figure 7.10.: Experimentally measured (squares) J/V characteristics (a) and series resistance (b) compared to simulated results using an equivalent circuit (line). The equivalent circuit using an injection dependent series resistance is able to reproduce the experimental results well.

phenomenon found in the imaging experiments of the previous chapters are reproduced using the newly developed model.

Differences of EL and EM-PL characteristics

In Section 5.1 it was found that the EL and and EM-PL junction voltages differ at the (assumed) same amount of injected currents. Using the new equivalent circuit it is possible to explain that result. Figure 7.11 shows the junction voltages measured, plotted, in the illuminated case, versus the current density for which it was measured. The junction voltages measured in the dark are plotted versus the current density shifted in two different ways (solid and dashed line). The solid line represents the case that was performed in the experiment. The current is shifted down by the measured short circuit current. It was assumed that this makes the illuminated and dark case comparable as the the current values should then correspond to the operating points where the same amounts of current recombine within the sample. However, similar to the experiment we see that the junction voltages in the dark case and illuminated case vary, when the junction voltage in the dark is shifted that way.

In contrast, when the current density is shifted by the real short circuit density that was put into the equivalent circuit model the junction voltages determined from EL and EM-PL now overlap perfectly (Figure 7.11). Thus, the surprising result that the junction voltages determined under illumination and in the dark were not compatible in the experimental results at low voltages simply results from the fact that the voltages were compared at different operating points, meaning different amounts of injected current. The measured short circuit cannot be used

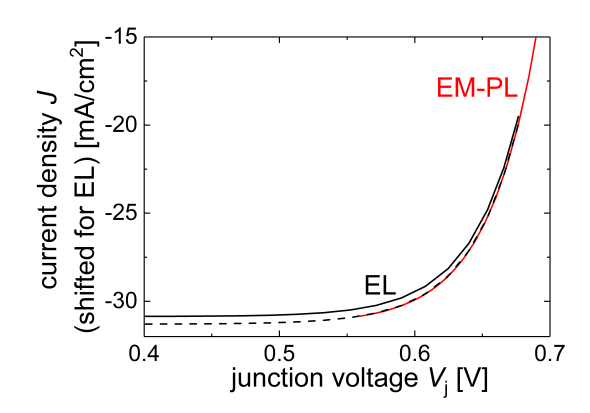


Figure 7.11: Junction voltages simulated using the new equivalent circuit model. The red line shows the junction voltage determined under illumination versus the corresponding current densities. The black lines show the junction voltage determine in the dark versus the corresponding (shifted) current densities. The solid line is shifted by the measured short circuit current (current at zero voltage under illumination), while the dashed line is shifted by the actual short circuit (set as a parameter for the equivalent circuit).

to shift the characteristic and make them comparable, as the high series resistance that is found at low voltages reduces the short circuit current that is measured at the terminals of device. The assumption that the recombining (injected) current in the device is zero under short circuit conditions does not hold for the analyzed CIGS solar cells.

The Influence of Shunts

In Section 5.1 it was additionally observed that the difference between the $J/V_{\rm j}$ characteristics determined in the dark and under illumination for shunted cells is especially large. We take a detailed look at this effect to see if it also only results from an incomplete collection of photocurrent at short circuit. In the new equivalent circuit a shunt is added as an external shunt. An external shunts means that the shunt is added between the terminals of the device in parallel to the series resistance and the diode. This was done for two reasons. Firstly, it is probably closer to reality, as a shunt usually appears only at one position of the cell, meaning that the bulk series resistance has to be between the shunt and photocurrent source. The photocurrent generated in the bulk at one position has to travel through the bulk and the contacts towards the shunt to recombine across the shunt. Secondly, the equivalent circuit yields unrealistic results if the shunt is placed in parallel only to the diode. A parallel resistance at this position, would significantly decrease the voltage drop across the diode (and the parallel

resistance), as the overall resistance of the two components is much smaller, than of the diode alone. This would lead in turn to a very large resistance of the series resistance as it only decreases if the voltage across the diode decreases. Thus, the whole equivalent circuit will be dominated by the large series resistance, which is in reality not the case. By implementing the shunt in parallel to the whole equivalent circuit, the circuit including the shunt can be easily solved by just adding the current through the shunt at every operating point to the already solved equivalent circuit currents without the shunt.

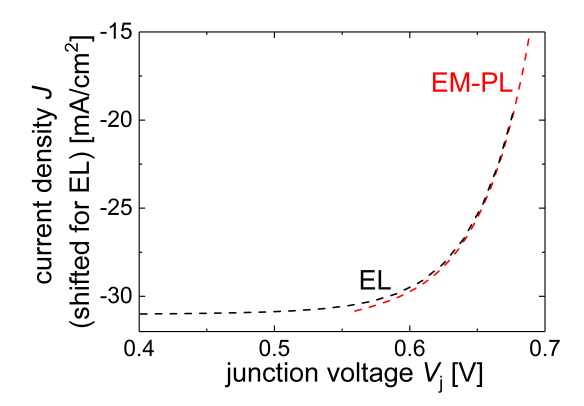


Figure 7.12.: Junction voltages simulated using the new equivalent circuit model including an external shunt of $2000 \,\Omega \text{cm}^2$. The red line shows the junction voltage determined under illumination versus the corresponding current densities. The black lines show the junction voltage determine in the dark versus the corresponding current densities shifted by the actual short circuit (set as a parameter for the equivalent circuit).

A shunt of $2000\,\Omega\mathrm{cm}^2$ was chosen as it was found be a realistic value looking at the dark J/V characteristic. In Figure 7.12 the junction voltage determined in the dark and under illumination is shown again, now plotted versus the currents including a shunt. The currents corresponding to the junction voltages in the dark (EL) are already shifted by the right short circuit current. Still, it is visible that the EL characteristic shows lower junction voltages at low currents than the EM-PL characteristic. Thus, we can also explain the larger difference between the EL and EM-PL characteristics, which were observed for the shunted cell (cf. Figure 5.5), with the new equivalent circuit.

The difference between the EL and EM-PL characteristic results from the different recombination paths the currents take under illumination and in the dark. Although the overall current recombining in the solar cell is the same at the operating points compared, under illumination a larger portion of that current recombines across the diode, increasing the junction voltage, while in the dark a smaller portion recombines across the diode and more across the shunt. Note, that such an effect would also be existing in a case without an injection dependent

series resistance, when a shunt is added externally, but the effect is more significant with an injection dependent series resistance, as the resistance gets larger at low voltages. Thus, determining a shunt resistance from $J/V_{\rm j}$ characteristics of CIGS solar cells is more reliable by using EL characteristic than the EM-PL characteristic. In the dark at low voltages the junction voltage is more similar to the shunt voltage, as the voltage loss across the series resistance is smaller, due to smaller currents.

The Influence on the Photocurrent Collection Efficiency

In Section 6.2 it was found that for CIGS solar cells the imaged photocurrent collection efficiency is especially at lower voltages not in alignment with the electrically measured one (cf. Figure 6.30). The imaged photocurrent collection efficiency was decreasing towards lower voltages while the electrically measured photocurrent collection efficiency only increases. Furthermore, are models based on the one-or two diode models not able to reproduces this effect. Having found that the CIGS solar cells contain an injection dependent series resistance we can now test, if that also causes the error in the $f_{\rm pc}$ imaging. For that we use again the new equivalent circuit that contains the injection dependent series resistance. First Equation 6.4 (the basis for the f_{pc} imaging using luminescence) is tested in the new equivalent circuit. The f_{pc} values are calculated at different voltages using the second term of the equation, i.e. changing the short circuit of the equivalent circuit slightly and observing the current at the terminals, and using the third term of the equation, i.e. determining the change of the junction voltage with the change of the external voltage. From the derivation of Wong both should be expected to be equal. However, in Figure 7.13 it is shown that the two terms are no longer equal. In fact, we see the characteristic increase and decrease of $f_{\rm pc}$ towards higher voltages, which was also seen in the experiments for the imaged $f_{\rm pc}$. Thus, the derivation of 6.4 does not seem to hold anymore for a system including an injection dependent series resistance.

The failure of Equation 6.4 for the new equivalent circuit can be proven mathematically by analyzing the total differentials of the currents in the equivalent circuit. For the current across the series resistance $J_{\rm R}$ it states:

$$dJ_{R} = \frac{\delta J_{R}}{\delta V_{R}} dV_{R} + \frac{\delta J_{R}}{\delta V_{j}} dV_{j}$$
(7.6)

The quantity $V_{\rm R}$ denotes the voltage drop across the series resistance. For the current through the diode and the photocurrent source the total differential states:

$$dJ_{j} = \frac{\delta J_{j}}{\delta V_{j}} dV_{j} + dJ_{ph}$$
(7.7)

Due to Kirchhoff's law both are equal so we use $dJ_j = dJ_R = dJ$. By additionally

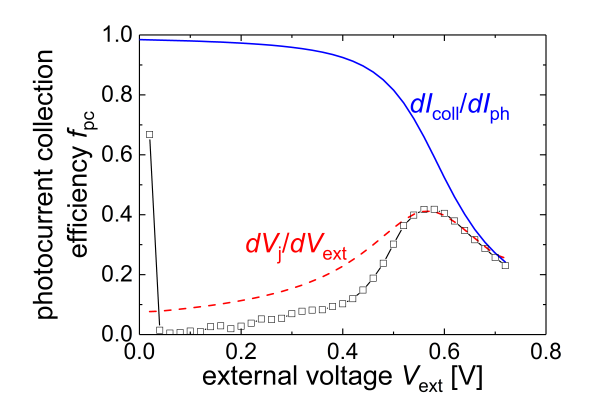


Figure 7.13.: The photocurrent collection efficiency of the new equivalent circuit model (including an injection dependent series resistance) under illumination. The blue line is calculated directly, by changing the short circuit current in the circuit slightly and determining the resulting current change. The red line is calculated with the derivation of Wong using the junction voltage differentiated with respect to the external voltage. As the two lines deviated the derivation of Wong does not hold for the new equivalent circuit. The black squares show the experimentally measured photocurrent collection efficiency. It is visible that the new equivalent circuit model reproduces the measurement well.

using

$$dV_{R} = dV_{\text{ext}} - dV_{i} \tag{7.8}$$

and setting $V_{\rm ext}$ constant (d $V_{\rm ext}=0$) we find for the photocurrent collection efficiency:

$$f_{\rm pc} = \frac{\mathrm{d}J}{\mathrm{d}J_{\rm ph}}\Big|_{dV_{\rm ext}=0} = \frac{\frac{\delta J_{\rm R}}{\delta V_{\rm R}} - \frac{\delta J_{\rm R}}{\delta V_{\rm j}}}{\frac{\delta J_{\rm j}}{\delta V_{\rm i}} + \frac{\delta J_{\rm R}}{\delta V_{\rm p}} - \frac{\delta J_{\rm R}}{\delta V_{\rm i}}}$$
(7.9)

Using Equation 7.6 and 7.7 but setting the photocurrent constant $(dJ_{ph} = 0)$ we find:

$$\frac{\mathrm{d}V_{\mathrm{j}}}{\mathrm{d}V_{\mathrm{ext}}}\bigg|_{dJ_{\mathrm{ph}}=0} = \frac{\frac{\delta J_{\mathrm{R}}}{\delta V_{\mathrm{R}}}}{\frac{\delta J_{\mathrm{j}}}{\delta V_{\mathrm{j}}} + \frac{\delta J_{\mathrm{R}}}{\delta V_{\mathrm{R}}} - \frac{\delta J_{\mathrm{R}}}{\delta V_{\mathrm{j}}}}$$
(7.10)

As Equation 7.9 and 7.10 are no longer equal, it proves that Equation 6.4 does not hold for an equivalent circuit including an injection dependent series resistance.

From the equations we can also understand why the imaged $f_{\rm pc}$ is lower under illumination and low voltages than the real $f_{\rm pc}$. The partial differential of the current through the resistance with respect to the junction voltage is

$$\frac{\delta J_{\rm R}}{\delta V_{\rm i}} = V_{\rm R} \frac{\delta \sigma_{\rm s}}{\delta V_{\rm i}}.$$
(7.11)

Here, σ_s is the conductivity of the series resistance, which increases with increasing junction voltage. Below $V_{\rm oc}$, under illumination $V_{\rm R}$ is negative and therefore $\delta J_{\rm R}/\delta V_{\rm j}$ is also negative. Thus, the imaged $f_{\rm pc}$ determined using Equation 7.10 underestimates the true photocurrent collection efficiency below $V_{\rm oc}$. Above $V_{\rm oc}$, $V_{\rm R}$ becomes positive leading to an overestimation of the true $f_{\rm pc}$. Without the term responsible for the injection dependent series resistance $\delta \sigma_{\rm s}/\delta V_{\rm j}$ the error disappears. Additionally, in the dark $V_{\rm R}$ is much lower at low voltages, which reduces the influence of the injection dependence of the series resistance on the results.

Voltage Dependent Photocurrent

For CIGS solar cells it was found that the photocurrent may show a significant voltage dependence [35, 115, 116]. This means, that the superposition principle does not hold for these cells, even in voltage regions where a series resistance should have no effect. The effect was often modeled by making the photocurrent depending on the applied voltage of the device using certain simplifications [117, 118]. However, for CIGS solar cells it was found that more sophisticated device simulations are needed [35, 119].

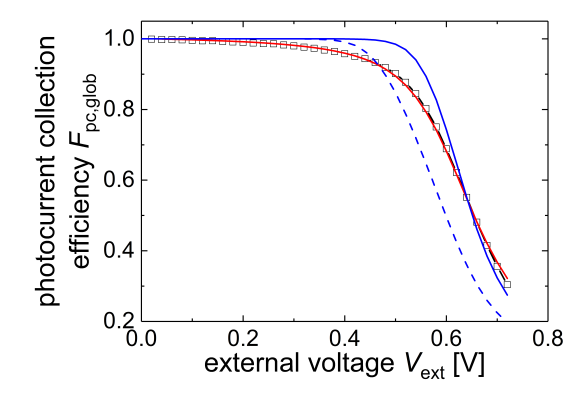


Figure 7.14.: Total global photocurrent collection efficacy determined for different cases, to visualize the voltage dependence of the photocurrent. Experimental data (black squares); fitted new equivalent circuit including an injection dependent series resistance (red); and equivalent circuit without an injection dependent series resistance and a constant resistance of $3.24\,\Omega\mathrm{cm}^2$ and $6\,\Omega\mathrm{cm}^2$ (blue solid and dashed line, respectively)

In the following, it will be shown, that an extension of the equivalent circuit with an injection dependent series resistance will also result in J/V characteristics that show a voltage dependent photocurrent, although the photocurrent source is set constant. The voltage dependence of the photocurrent can be easily seen in the total global photocurrent collection efficiency (c.f. Equation 6.15). In Figure

7.14 the $F_{\rm pc,glob}$ values are shown for different cases. Note, that these values are directly calculated from the J/V-characteristics using the second term of Equation 6.15. The two blue curves shows the behavior of the photocurrent in a normal equivalent circuit without an injection dependent series resistance. We see that the superposition principle breaks down at larger voltage $(F_{pc,glob} < 1)$ due to the series resistance. However, at low voltages the photocurrent is voltage independent $(F_{pc,glob} = 1)$ and the superposition principle holds. Increasing the series resistance, shifts the position at which $F_{\rm pc,glob}$ starts to decrease to smaller voltages. For the experimental data, and the fitted new equivalent circuit including the injection dependent series resistance we observe a much less abrupt decrease of $F_{\rm pc,glob}$, which starts already at zero volts. Such a decrease cannot be reproduced with an equivalent circuit including only a constant series resistance. Thus, the behavior needs to be explained by voltage dependent photocurrent or an effect that produces a similar result. In the new equivalent circuit the actual generated photocurrent source is constant, thus the seen voltage dependence of the photocurrent at the contacts needs to result from the injection dependence of the series resistance. In the following it will be taken a closer look at the mathematics of the new equivalent circuit, which lead to the results that look like voltage dependent photocurrent.

The total differential given by Equation 7.6 is used again to determine the change of the current through the device depending on the external voltage. By making additionally use of Equation 7.8 and 7.11 we find

$$\frac{\mathrm{d}J}{\mathrm{d}V_{\mathrm{ext}}} = \frac{\delta J_{\mathrm{R}}}{\delta V_{\mathrm{R}}} \left(1 - \frac{\mathrm{d}V_{\mathrm{j}}}{\mathrm{d}V_{\mathrm{ext}}} \right) + V_{\mathrm{R}} \frac{\delta \sigma_{\mathrm{s}}}{\delta V_{\mathrm{j}}} \frac{\mathrm{d}V_{\mathrm{j}}}{\mathrm{d}V_{\mathrm{ext}}}. \tag{7.12}$$

The second term of the sum is close to zero in the dark at lower voltages due to $V_{\rm R}$ being very small. Also ${\rm d}V_{\rm j}/{\rm d}V_{\rm ext}$ is close to one in this regime in the dark, as the resistance of the diode is still higher than the series resistance (even with it being larger due to the injection dependence). Thus, in the dark at lower voltages the change of the current with the external voltage is close to zero. Under illumination this changes. As ${\rm d}V_{\rm j}/{\rm d}V_{\rm ext}$ is now much smaller at low voltages and ${\rm d}J_{\rm R}/{\rm d}V_{\rm R}$ (the differential conductivity of the series resistance) is also larger, the first term now plays a role for the gradient of the current. Furthermore, it can be seen in calculations that the second term is also relevant as the magnitude of $V_{\rm R}$ is larger and counterbalances the lower ${\rm d}V_{\rm j}/{\rm d}V_{\rm ext}$. As the second term is negative due to $V_{\rm R}$ being negative, the gradient of the current results from the interplay of the two terms and happens to be larger than the gradient of the current in the dark. The changing gradient of the J/V characteristics at low voltages with increasing illumination, is seen as voltage dependent photocurrent.

7.5. Conclusion

Due to some unexplained imaging results for CIGS solar cells, a closer look was taken at the properties of the CIGS samples. It was found, that the CIGS samples contain an injection dependent series resistance. This resistance effect could also be shown in SCAPS simulations. Further analysis of the simulation showed that the resistance effect results from the transport of electrons through the CIGS absorber, as the resistance is mainly depending on the electron mobility in the CIGS conduction band.

To analyze the influence of an injection dependent series resistance on the luminescence imaging methods an equivalent circuit was developed that reproduced the characteristics of the injection dependent series resistance. The new equivalent circuit explains the effects that were beforehand not understood. The differences between EL and EM-PL characteristics are explained by an incomplete collection of photocurrent at short circuit. When using the real generated photocurrent and not the measured short circuit current to shift the EL or EM-PL characteristic the results are consistent. The failure of the photocurrent collection efficiency imaging on CIGS solar cells at low voltages is also explained, as the equations used for the imaging method do not hold in the new equivalent circuit. Additionally, it was found that the injection dependent series resistance also reproduces voltage dependent photocurrent. This might offer the new equivalent circuit as a possible tool to better analyze solar cells that show these kind of effects.

8. Conclusion and Outlook

Luminescence imaging techniques are able to obtain spatially resolved information about a solar cells or modules properties, which is excellent in the research and development of solar cells but also for the monitoring of production processes or modules operating in a solar power plants. However, to correctly interpret imaging results the underlying models used need to be confirmed. An independent diode model is not applicable in many situations and in this work it was found that also an interconnected model using only standard equivalent circuits might not be adequate for describing CIGS solar cell imaging results.

This work started by analyzing the metastable changes that happen to CIGS solar cells during luminescence measurements. The already found effect of decreasing non-radiative recombination and decreasing series resistance, due to an excitation with light or bias, was confirmed. A closer look at the time dependence at different conditions was performed, showing that the effects happen fast, but also over long timescales. This behavior complicates the reduction of metastable changes in imaging experiments on CIGS solar cells. However, in this works further experiments the influence of metastable effects were successfully avoided by automation and repetition of the experiments under varying order.

To begin the quantitative luminescence imaging, a method to reconstruct current / junction voltage characteristics of solar cells connected into a module using electroluminescence is tested and extended to measurements under illumination (using electro-modulated photoluminescence). The measurements under illumination are important to understand how the method changes due to daylight luminescence imaging compared to electroluminescence imaging in the dark. Within the simple illustration of solar cells with one- or two-diode equivalent circuits the results should not change depending on the illumination condition. However, a closer look revealed deviations in the experiments, when comparing current / junction voltage characteristics measured in the dark and under illumination. PVMOS simulations were used to analyze the results. They showed that deviations at higher voltages result from a geometrical effect. The current distribution in a solar cell in the dark and under illumination is different especially at higher voltages around the $V_{\rm oc}$, which leads to an error when using the average of local voltages to describe the effective cell voltage. The deviation at lower voltages was found to be due to an injection dependent series resistance, leading to an incomplete collection of photocurrent under short circuit conditions and therefore to wrong assumptions about the amount of internal recombination under illumination.

Furthermore, a large part of this work focuses on an imaging technique based on

an independent diode model. A method called photocurrent collection efficiency imaging is tested, discussed in detail, and further developed. The Photocurrent collection efficiency describes the portion of the locally generated photocurrent that contributes to the current at the terminals of the sample. In the original form it was defined for differential changes, i.e. describing the probability of an infinitesimal small change in the photocurrent to contribute to the current at the terminals. The method was tested and confirmed on a global scale using a mono-crystalline silicon solar cell and independent electrical measurements obtained from small changes in the illumination. PVMOS simulations confirmed the method also on a local scale.

The differential photocurrent collection efficiency method was further developed in this work to yield a total photocurrent collection efficiency. This method, uses differential photocurrent collection efficiency images measured at various illumination intensities to show exactly where the amount of total photocurrent collected by a solar cell originates from. The method was also confirmed and demonstrated on crystalline silicon solar cells using experiments and PVMOS simulations. Furthermore, it was discussed with the help of PVMOS simulations which additional information would be needed to determine from the total collected photocurrent image a net power output image that describes the actual contribution of each region to a solar cells power output.

Photocurrent collection efficiency imaging was additionally applied to solar modules and the results were discussed in detail. The physical meaning of the photocurrent collection efficiency stays the same in modules, but the understanding is less straight forward. Defected solar cells in modules may show a larger photocurrent collection efficiency as they are limiting the current through the module. An illumination change on the defected cells has therefore a larger effect on the overall current output. Thus, regions of a larger photocurrent collection efficiency in a module correspond no longer to the regions of better quality. Net power imaging applied in simulations showed furthermore, that the limiting, defected solar cells in modules may even provide a larger power output then the other cells.

Photocurrent collection efficiency imaging was also tested on CIGS solar cells. Although it was expected to work as the reciprocity relation should hold and the underlying model was an interconnected diode model, discrepancies with the imaging results and independent electrical measurements were found at lower voltages. The effect could not be reproduced using PVMOS. However, by taking an injection dependent series resistance into account the discrepancies can be explained.

Thus, in the final part of this work the origin and influence of an injection dependent series resistance was analyzed. SCAPS simulations showed that it results from the minority carrier transport through the bulk of the CIGS absorber. By including the injection dependent series resistance into a standard one-diode equivalent circuit, it was shown that such a resistance can explain the photocurrent collection efficiency measurements of CIGS solar cells as well as discrepancies with

current/junction voltage characteristics determined from luminescence images under illumination and in the dark. Furthermore, it was found that such a series resistance can explain voltage dependent photocurrent, even when the photocurrent in the equivalent circuit is not made voltage dependent. Thus, such a model might prove to be useful for further characterization or modeling of solar cells affected by transport properties that result in voltage dependent photocurrent.

In summary, this work discussed in detail two imaging methods, what can be learned from them and what their limitations are. It was found that special properties of CIGS solar cells, which are not clearly visible with only electrical characterization methods, influence luminescence imaging results. Thus, even if the reciprocity relation holds and an interconnected diode model is used for the analysis, the special properties of each analyzed solar cell technology need to be considered in the interpretation of luminescence imaging results.

It will be a question for further work, if the expenditures are worth the information obtained from the luminescence imaging methods described, to actually apply the methods to solar cells and modules in solar power plants or in production lines. The methods can be quite extensive as several images at different working points are needed and they need a contacting of the sample. However, the discussed methods provide quantitative information that make them more valuable then simple luminescence images. Additionally, it remains the question if a model using an injection dependent series resistance will replace models using voltage dependent photocurrents. A model using an injection dependent series resistance is less straight forward to understand, but it is able to explain imaging results that voltage dependent photocurrent models cannot explain.

A. Appendix - Chapter 6

Noise in the Local Differential Photocurrent Collection Efficiency Image

In the following it is shortly derived how noise in a luminescence image is propagated to the local differential photocurrent collection efficiency image $f_{\rm pc,loc}$. The $f_{\rm pc,loc}$ is calculated in the following from the luminescence images $S_{\rm cam,1}, S_{\rm cam,2}, S_{\rm cam,bg}$

$$f_{\rm pc,loc} = \ln \left(\frac{S_{\rm cam,1} - S_{\rm cam,bg}}{S_{\rm cam,2} - S_{\rm cam,bg}} \right) \frac{V_{\rm th}}{\delta V_{\rm ext}},\tag{A.1}$$

which we can rewrite to

$$f_{\text{pc,loc}} = \frac{V_{\text{th}}}{\delta V_{\text{ext}}} \left(\ln \left(S_{\text{cam},1} - S_{\text{cam,bg}} \right) - \ln \left(S_{\text{cam},2} - S_{\text{cam,bg}} \right) \right). \tag{A.2}$$

The error in the luminescence images S_{cam} is equal to $\sqrt{S_{\text{cam}}}$. Thus, the error $\sigma_{-,1/2}$ on $(S_{\text{cam},1/2} - S_{\text{cam},\text{bg}})$ is

$$\sigma_{-,1/2} = \sqrt{S_{\text{cam},1/2} + S_{\text{cam,bg}}}.$$
 (A.3)

Furthermore, the error $\sigma_{\ln,1/2}$ on $\ln \left(S_{\text{cam},1/2} - S_{\text{cam,bg}} \right)$ is given by

$$\sigma_{\ln,1/2} = \frac{\sigma_{-,1/2}}{S_{\text{cam},1/2} - S_{\text{cam,bg}}}.$$
 (A.4)

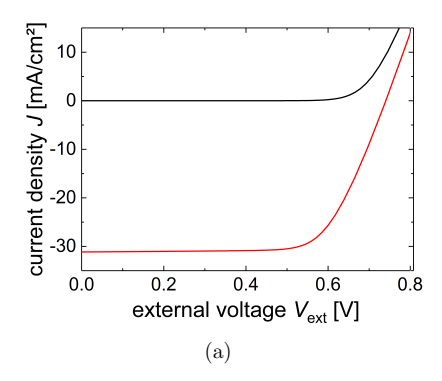
From equation A.2 we see that the error $\sigma f_{\rm pc,loc}$ of the photocurrent collection efficiency reads

$$\sigma f_{\rm pc,loc} = \frac{V_{\rm th}}{\delta V_{\rm ext}} \sqrt{\sigma_{\rm ln,1}^2 + \sigma_{\rm ln,2}^2}$$
 (A.5)

which after insertion reads

$$\sigma f_{\text{pc,loc}} = \frac{V_{\text{th}}}{\delta V_{\text{ext}}} \sqrt{\left(\frac{\sqrt{S_{\text{cam,1}} + S_{\text{cam,bg}}}}{S_{\text{cam,1}} - S_{\text{cam,bg}}}\right)^2 + \left(\frac{\sqrt{S_{\text{cam,2}} + S_{\text{cam,bg}}}}{S_{\text{cam,2}} - S_{\text{cam,bg}}}\right)^2}.$$
(A.6)

B. Appendix - Chapter 7



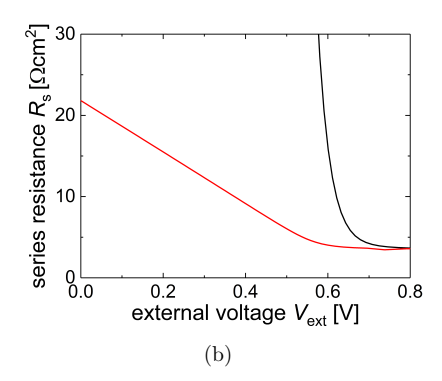


Figure B.1.: J/V characteristics and series resistance simulated in the dark (black) and under illumination (red) with varying CdS electron mobilities from $5\,\mathrm{cm^2/Vs}$ to $85\,\mathrm{cm^2/Vs}$ in $20\,\mathrm{cm^2/Vs}$ steps. No influence of the CdS electron mobility on the solar cells properties are visible

Bibliography

- [1] Natural Resources Defense Council. The cost of climate change: what we'll pay if global warming continues unchecked., 2007.
- [2] U.S. National Climate Assessment. Climate change impacts in the united states, 2007.
- [3] H. Lesch and K. Kamphausen. *Die Menschheit schafft sich ab*, pages 354–361. Komplett-Media, 2017.
- [4] Fraunhofer-Institute for Solar Energy Systems. Current and future cost of photovoltaics, 2015.
- [5] Solar Power Europe. Global market outlook for solar power, 2017.
- [6] ISE Fraunhofer Institute for Solar Energy Systems. Photovoltaics report, 2017.
- [7] H. Denio. Aerial solar thermography and condition monitoring of photovoltaic systems. In 2012 38th IEEE Photovoltaic Specialists Conference, pages 000613–000618, 2012.
- [8] PI Berlin. https://www.pi-berlin.com/en/el-test_en.html. accessed 13/09/2017.
- [9] Y. Augarten, A. Wrigley, A. Gerber, B. Pieters, and U. Rau. Quantitative outdoor imaging: Analysis of solar modules in daylight. In 32nd European Photovoltaic Solar Energy Conference and Exhibition, pages 1846 – 1848, 2016.
- [10] K. Ramspeck, K. Bothe, J. Schmidt, and R. Brendel. Correlation between spatially resolved solar cell efficiency and carrier lifetime of multicrystalline silicon. J. Mater. SCI. - Mater. El., 19:4–8, 2008. doi:10.1007/s10854-008-9671-8.
- [11] F. Frühauf and O. Breitenstein. DLIT- versus ILIT-based efficiency imaging of solar cells. Sol. Energ. Mat. Sol. Cells., 169:195 202, 2017. doi:10.1016/j.solmat.2017.05.015.

- [12] O. Breitenstein, M. Langenkamp, O. Lang, and A. Schirrmacher. Shunts due to laser scribing of solar cells evaluated by highly sensitive lock-in thermography. *Sol. Energ. Mat. Sol. Cells.*, 65:55 62, 2001. doi:10.1016/S0927-0248(00)00077-5.
- [13] O. Breitenstein, J. P. Rakotoniaina, A. S. H. van der Heide, and J. Carstensen. Series resistance imaging in solar cells by lock-in thermography. *Prog. Photovolt. Res. Appl.*, 13:645–660, 2005. doi:10.1002/pip.623.
- [14] T. Fuyuki, H. Kondo, T. Yamazaki, Y. Takahashi, and Y. Uraoka. Photographic surveying of minority carrier diffusion length in polycrystalline silicon solar cells by electroluminescence. *Appl. Phys. Lett.*, 86:262108, 2005. doi:10.1063/1.1978979.
- [15] U. Rau. Reciprocity relation between photovoltaic quantum efficiency and electroluminescent emission of solar cells. *Phys. Rev. B*, 76:085303, 2007. doi:10.1103/PhysRevB.76.085303.
- [16] U. Rau. Superposition and reciprocity in the electroluminescence and photoluminescence of solar cells. *IEEE J. Photovolt.*, 2:169–172, 2012. doi:10.1109/JPHOTOV.2011.2179018.
- [17] D. Han, K. Wang, and L. Yang. Recombination and metastability in amorphous silicon p-i-n solar cells made with and without hydrogen dilution studied by electroluminescence. J. Appl. Phys., 80:2475–2482, 1996. doi:10.1063/1.363083.
- [18] D. Prządo, M. Igalson, R. Bacewicz, and M. Edoff. The influence of metastabilities on the luminescence in the Cu(In,Ga)Se₂ solar cells. *Acta Phys. Pol. A*, 112:183, 2007.
- [19] O. Breitenstein, J. Bauer, M. Kittler, T. Arguirov, and W. Seifert. EBIC and luminescence studies of defects in solar cells. *Scanning*, 30:331–338, 2008. doi:10.1002/sca.20112.
- [20] U. Hoyer, M. Wagner, Th. Swonke, J. Bachmann, R. Auer, A. Osvet, and C. J. Brabec. Electroluminescence imaging of organic photovoltaic modules. *Appl. Phys. Lett.*, 97:233303, 2010. doi:10.1063/1.3521259.
- [21] T. Trupke, E. Pink, R. A. Bardos, and M. D. Abbott. Spatially resolved series resistance of silicon solar cells obtained from luminescence imaging. *Appl. Phys. Lett.*, 90:093506, 2007. doi:10.1063/1.2709630.
- [22] M. Glatthaar, J. Haunschild, M. Kasemann, J. Giesecke, W. Warta, and S. Rein. Spatially resolved determination of dark saturation current and series resistance of silicon solar cells. *Phys. Status Solidi RRL*, 4:13–15, 2010. doi:10.1002/pssr.200903290.

- [23] K. Ramspeck, K. Bothe, D. Hinken, B. Fischer, J. Schmidt, and R. Brendel. Recombination current and series resistance imaging of solar cells by combined luminescence and lock-in thermography. *Appl. Phys. Lett.*, 90:153502, 2007. doi:10.1063/1.2721138.
- [24] O. Breitenstein, A. Khanna, Y. Augarten, J. Bauer, J.-M. Wagner, and K. Iwig. Quantitative evaluation of electroluminescence images of solar cells. *Phys. Status Solidi RRL*, 4:7–9, 2010. doi:10.1002/pssr.200903304.
- [25] J. Haunschild, M. Glatthaar, M. Kasemann, S. Rein, and E. R. Weber. Fast series resistance imaging for silicon solar cells using electroluminescence. *physica status solidi* (*RRL*) *Rapid Research Letters*, 3:227–229, 2009. doi:10.1002/pssr.200903175.
- [26] M. A. Green, Y. Hishikawa, W. Warta, E. D. Dunlop, D. H. Levi, J. Hohl-E-binger, and A. W.H. Ho-Baillie. Solar cell efficiency tables (version 50). *Prog. Photovolt. Res. Appl.*, 25:668–676, 2017. doi:10.1002/pip.2909.
- [27] T. C. M. Müller. Light Absorbtion and Radiative Recombination in Thin-Film Solar Cells. PhD thesis, Rheinisch-Westfälischen Technischen Hochschule Aachen, 2015.
- [28] M. Siegloch. Failure Analysis of Thin Film Solar Modules using Lockin Thermography. PhD thesis, Rheinisch-Westfälischen Technischen Hochschule Aachen, 2014.
- [29] J. Wong and M. A. Green. From junction to terminal: Extended reciprocity relations in solar cell operation. *Phys. Rev. B*, 85:235205, 2012. doi:10.1103/PhysRevB.85.235205.
- [30] J. Wong. Perturbation theory for solar cell efficiency II delineating series resistance. *IEEE Trans. Electron Devices*, 60:917–922, 2013. doi:10.1109/TED.2012.2236334.
- [31] P. Würfel. Physics of Solar Cells, pages 132–142. Wiley-VCH, 2009.
- [32] P. Würfel. Physics of Solar Cells, pages 43–96. Wiley-VCH, 2009.
- [33] D. Abou-Ras, T. Kirchartz, and U. Rau. Advanced Characterization Techniques for Thin Film Solar Cells, pages 16–18. Wiley-VCH, 2011.
- [34] D. Abou-Ras, T. Kirchartz, and U. Rau. Advanced Characterization Techniques for Thin Film Solar Cells, pages 36–41. Wiley-VCH, 2011.
- [35] M. Gloeckler, C. R. Jenkins, and J. R. Sites. Explanation of light/dark superposition failure in CIGS solar cells. MRS Proceedings, 763, 2003. doi:10.1557/PROC-763-B5.20.

- [36] R. Scheer and H.-W. Schock. Chalcogenide Photovoltaics, pages 252–275. Wiley-VCH, 2012.
- [37] T. Tinoco, C. Rincón, M. Quintero, and G. Sánchez Pérez. Phase diagram and optical energy gaps for $Cu(In_y,Ga_{1-y})Se_2$ alloys. *Phys. Status Solidi A*, 124:427-434, 1991. doi:10.1002/pssa.2211240206.
- [38] N. E. Gorji, U. Reggiani, and L. Sandrolini. Graded band gap CIGS solar cells considering the valence band widening. In 38th IEEE Photovoltaic Specialists Conference, pages 000906–000908, 2012.
- [39] A. M. Gabor, J. R. Tuttle, D. S. Albin, M. A. Contreras, R.l Noufi, and A. M. Hermann. High-efficiency $Cu(In_{1-x},Ga_x)Se_2$ solar cells made from $(In_x,Ga_{1-x})_2Se_3$ precursor films. *Appl. Phys. Lett.*, 65:198–200, 1994. doi:10.1063/1.112670.
- [40] W. K. Metzger, I. L. Repins, M. Romero, P. Dippo, M. Contreras, R. Noufi, and D. Levi. Recombination kinetics and stability in polycrystalline Cu(In,Ga)Se₂ solar cells. *Thin Solid Films*, 517:2360 2364, 2009. doi:10.1016/j.tsf.2008.11.050.
- [41] R. Hunger, M.V. Lebedev, K. Sakurai, T. Schulmeyer, Th. Mayer, A. Klein, S. Niki, and W. Jaegermann. Junction formation of CuInSe₂ with CdS: A comparative study of "dry" and "wet" interfaces. *Thin Solid Films*, 515:6112 6118, 2007. doi:10.1016/j.tsf.2006.12.120.
- [42] L. C. Olsen, P. Eschbach, and Sambhu Kundu. Role of buffer layers in CIS-based solar cells. In Conference Record of the Twenty-Ninth IEEE Photovoltaic Specialists Conference, pages 652–655, 2002.
- [43] Z. A. Wang, J. B. Chu, H. B. Zhu, Z. Sun, Y. W. Chen, and S. M. Huang. Growth of ZnO:Al films by rf sputtering at room temperature for solar cell applications. *Solid State Electron*, 53:1149 1153, 2009. doi:10.1016/j.sse.2009.07.006.
- [44] B. Misic, B. E. Pieters, J. P. Theisen, A. Gerber, and U. Rau. Shunt mitigation in ZnO:Al/i-ZnO/CdS/Cu(In,Ga)Se₂ solar modules by the i-ZnO/CdS buffer combination. *Phys. Status Solidi A*, 212:541–546, 2015. doi:10.1002/pssa.201431496.
- [45] P.-O. Westin, U. Zimmermann, and M. Edoff. Laser patterning of P2 interconnect via in thin-film CIGS PV modules. *Sol. Energ. Mat. Sol. Cells*, 92:1230 1235, 2008. doi:10.1016/j.solmat.2008.04.015.
- [46] A. Buzás and Z. Geretovszky. Patterning ZnO layers with frequency doubled and quadrupled nd:yag laser for pv application. *Thin Solid Films*, 515:8495 8499, 2007. doi:10.1016/j.tsf.2007.04.026.

- [47] D. L. Staebler and C. R. Wronski. Reversible conductivity changes in discharge-produced amorphous Si. Appl. Phys. Lett., 31:292–294, 1977. doi:10.1063/1.89674.
- [48] M. N. Ruberto and A. Rothwarf. Time—dependent open—circuit voltage in CuInSe₂/CdS solar cells: Theory and experiment. *J. Appl. Phys.*, 61:4662–4669, 1987. doi:10.1063/1.338377.
- [49] H.-W. Schock, T. Walter, and R. Herberholz. Distribution of defects in polycrytalline chalcopyrite thin films. In *Polycrystalline Semiconductors IV*, volume 51 of *Solid State Phenomena*, pages 309–316. Trans Tech Publications, 1996.
- [50] D. Willett and S. Kuriyagawa. The effects of sweep rate, voltage bias and light soaking on the measurement of CIS-based solar cell characteristics. In *Conference Record of the Twenty Third IEEE Photovoltaic Specialists Conference*, pages 495–500, 1993. doi:10.1109/PVSC.1993.347131.
- [51] R.A Sasala and J.R. Sites. Time dependent voltage in CuInSe₂ and CdTe solar cells. In Conference Record of the Twenty Third IEEE Photovoltaic Specialists Conference, pages 543–548, 1993. doi:10.1109/PVSC.1993.347036.
- [52] M. Igalson and H. W. Schock. The metastable changes of the trap spectra of $CuInSe_2$ —based photovoltaic devices. *J. Appl. Phys.*, 80:5765–5769, 1996. doi:10.1063/1.363631.
- [53] U. Rau, M. Schmitt, J. Parisi, W. Riedl, and F. Karg. Persistent photoconductivity in Cu(In,Ga)Se₂ heterojunctions and thin films prepared by sequential deposition. *Appl. Phys. Lett.*, 73:223–225, 1998. doi:10.1063/1.121762.
- [54] F. Engelhardt, M. Schmidt, Th. Meyer, O. Seifert, J. Parisi, and U. Rau. Metastable electrical transport in Cu(In,Ga)Se₂ thin films and ZnO/CdS/Cu(In,Ga)Se₂ heterostructures. *Phys. Lett. A*, 245:489–493, 1998. doi:10.1016/S0375-9601(98)00401-0.
- [55] R. Scheer and H.-W. Schock. Chalcogenide Photovoltaics, pages 292–298. Wiley-VCH, 2012.
- [56] T. Eisenbarth. *Identifkation von Defekten und Metastabilitäten in Cu(In,Ga)Se*₂-Dünnschichtsolarzellen. PhD thesis, Freie Universität Berlin, 2010.
- [57] M. Igalson, A. Kubiaczyk, and P. Zabierowski. Deep centers and fill factor losses in the CIGS devices. In Symposium H II-IV Compound Semiconductor Photovoltaic Materials, volume 668 of MRS Proceedings, 2001. doi:10.1557/PROC-668-H9.2.

- [58] T. Meyer, M. Schmidt, F. Engelhardt, J. Parisi, and U. Rau. A model for the open circuit voltage relaxation in Cu(In,Ga)Se₂ heterojunction solar cells. *Eur. Phys. J. AP*, 8:43–52, 1999. doi:10.1051/epjap:1999228.
- [59] J. T. Heath, J. D. Cohen, and W. N. Shafarman. Distinguishing metastable changes in bulk CIGS defect densities from interface effects. *Thin Solid Films*, 431:426–430, 2003. doi:10.1016/S0040-6090(03)00189-5.
- [60] I. L. Eisgruber, J. E. Granata, J. R. Sites, J. Hou, and J. Kessler. Blue-photon modification of nonstandard diode barrier in Cu(In,Ga)Se₂ solar cells. Sol. Energ. Mat. Sol. Cells., 53:367–377, 1998. doi:10.1016/S0927-0248(98)00035-X.
- [61] M. Igalson, M. Cwil, and M. Edoff. Metastabilities in the electrical characteristics of CIGS devices: Experimental results vs theoretical predictions. Thin Solid Films, 515:6142–6146, 2007. doi:10.1016/j.tsf.2006.12.038.
- [62] V. Nadazdy, M. Yakushev, E. H. Djebbar, A. E. Hill, and R. D. Tomlinson. Switching of deep levels in CuInSe₂ due to electric field-induced Cu ion migration. J. Appl. Phys., 84:4322–4326, 1998. doi:10.1063/1.368651.
- [63] P. Zabierowski, U. Rau, and M. Igalson. Classification of metastabilities in the electrical characteristics of ZnO/CdS/Cu(In,Ga)Se₂ solar cells. *Thin Solid Films*, 387:147–150, 2001. doi:10.1016/S0040-6090(00)01850-2.
- [64] M. Igalson, M. Bodegard, L. Stolt, and A. Jasenek. The 'defected layer' and the mechanism of the interface-related metastable behavior in the $\rm ZnO/CdS/Cu(In,Ga)Se_2$ devices. Thin Solid Films, 431:153–157, 2003. doi:10.1016/S0040-6090(03)00221-9.
- [65] M. Cwil, M. Igalson, P. Zabierowski, C. A. Kaufmann, and A. Neisser. Capacitance profiling in the CIGS solar cells. *Thin Solid Films*, 515:6229–6232, 2007. doi:10.1016/j.tsf.2006.12.102.
- [66] A. Niemegeers, M. Burgelman, R. Herberholz, U. Rau, D. Hariskos, and H.-W. Schock. Model for electronic transport in Cu(In,Ga)Se₂ solar cells. *Prog. Photovolt. Res. Appl.*, 6:407–421, 1998. doi:10.1002/(SICI)1099-159X(199811/12)6:6<407::AID-PIP230>3.0.CO;2-U.
- [67] M. Igalson, M. Bodegard, and L. Stolt. Reversible changes of the fill factor in the ZnO/CdS/Cu(In,Ga)Se₂ solar cells. *Sol. Energ. Mat. Sol. Cells.*, 80:195–207, 2003. doi:10.1016/j.solmat.2003.06.006.
- [68] J.-F. Guillemoles, L. Kronik, D. Cahen, U. Rau, A. Jasenek, and H.-W. Schock. Stability issues of Cu(In,Ga)Se₂-based solar cells. *J. Phys. Chem. B*, 104:4849–4862, 2000. doi:10.1021/jp993143k.

- [69] S. Lany and A. Zunger. Light- and bias-induced metastabilities in $Cu(In,Ga)Se_2$ based solar cells caused by the $(V_{Se}-V_{Cu})$ vacancy complex. J. Appl. Phys., 100:113725, 2006. doi:10.1063/1.2388256.
- [70] M. Cwil, M. Igalson, P. Zabierowski, and S. Siebentritt. Charge and doping distributions by capacitance profiling in Cu(In,Ga)Se₂ solar cells. *J. Appl. Phys.*, 103:063701, 2008. doi:10.1063/1.2884708.
- [71] T. Eisenbarth, R. Caballero, M. Nichterwitz, C. A. Kaufmann, H.-W. Schock, and T. Unold. Characterization of metastabilities in Cu(In,Ga)Se₂ thin-film solar cells by capacitance and current-voltage spectroscopy. *J. Appl. Phys.*, 110:094506, 2011. doi:10.1063/1.3656453.
- [72] M. Igalson and M. Edoff. Compensating donors in Cu(In,Ga)Se₂ absorbers of solar cells. Thin Solid Films, 480:322–326, 2005. doi:10.1016/j.tsf.2004.11.205.
- [73] M. Maciaszek and P. Zabierowski. On the magnitude of the persistent photoconductivity (ppc) effect in CIGS layers with and without sodium. In *IEEE 42nd Photovoltaic Specialist Conference (PVSC)*, pages 1–3, 2015.
- [74] F. Obereigner, N. Barreau, W. Witte, and R. Scheer. Open-circuit and doping transients of Cu(In,Ga)Se₂ solar cells with varying Ga content. J. Appl. Phys., 117:055704, 2015. doi:10.1063/1.4907391.
- [75] K. Macielak, M. Maciaszek, M. Igalson, P. Zabierowski, and N. Barreau. Persistent photoconductivity in polycrystalline Cu(In,Ga)Se₂ thin films: Experiment versus theoretical predictions. *IEEE J. Photovolt.*, 5:1206–1211, 2015. doi:10.1109/JPHOTOV.2015.2423491.
- [76] S. Dittmann, A. Virtuani, G. Friesen, and F. Serrano. Current-soaking and dark storage effects of polycrystalline thin film solar modules. In *IEEE 40th Photovoltaic Specialist Conference (PVSC)*, pages 2639–2643, 2014.
- [77] M. G. Deceglie, T. J. Silverman, K. Emery, D. Dirnberger, A. Schmid, S. Barkaszi, N. Riedel, L. Pratt, S. Doshi, G. Tamizhmani, B. Marion, and S. R. Kurtz. Validated method for repeatable power measurement of CIGS modules exhibiting light-induced metastabilities. *IEEE J. Photovolt.*, 5:607–612, 2015. doi:10.1109/JPHOTOV.2014.2376056.
- [78] P. Würfel. The chemical potential of radiation. J. Phys. C: Solid State Phys., 15:3967, 1982.
- [79] T. Kirchartz and U. Rau. Detailed balance and reciprocity in solar cells. *Phys. Status Solidi A*, 205:2737–2751, 2008. doi:10.1002/pssa.200880458.

- [80] T. Kirchartz, A. Helbig, W. Reetz, M. Reuter, J. H. Werner, and U. Rau. Reciprocity between electroluminescence and quantum efficiency used for the characterization of silicon solar cells. *Prog. Photovolt. Res. Appl.*, 17:394–402, 2009. doi:10.1002/pip.895.
- [81] W. Gong, M. A. Faist, N. J. Ekins-Daukes, Z. Xu, D. D. C. Bradley, J. Nelson, and T. Kirchartz. Influence of energetic disorder on electroluminescence emission in polymer:fullerene solar cells. *Phys. Rev. B*, 86:024201, 2012. doi:10.1103/PhysRevB.86.024201.
- [82] T.M.H. Tran. Quantitative analysis of spatially resolved electroluminescence of $Cu(In,Ga)Se_2$ and a-Si:H thin-film solar cells and modules. PhD thesis, Rheinisch-Westfälischen Technischen Hochschule Aachen, 2014.
- [83] T. Kirchartz, U. Rau, M. Kurth, J. Mattheis, and J.H. Werner. Comparative study of electroluminescence from Cu(In,Ga)Se₂ and Si solar cells. *Thin Solid Films*, 515:6238 6242, 2007. doi:10.1016/j.tsf.2006.12.105.
- [84] O. Breitenstein, J. Bauer, D. Hinken, and K. Bothe. The reliability of thermography- and luminescence-based series resistance and saturation current density imaging. *Sol. Energ. Mat. Sol. Cells.*, 137:50 60, 2015. doi:10.1016/j.solmat.2015.01.017.
- [85] O. Breitenstein, J. Bauer, K. Bothe, D. Hinken, J. Müller, W. Kwapil, M. C. Schubert, and W. Warta. Can luminescence imaging replace lock-in thermography on solar cells and wafers? *IEEE J. Photovolt.*, 1:159–167, 2011. doi:10.1109/JPHOTOV.2011.2169394.
- [86] M. Glatthaar, J. Giesecke, M. Kasemann, J. Haunschild, M. The, W. Warta, and S. Rein. Spatially resolved determination of the dark saturation current of silicon solar cells from electroluminescence images. *J. Appl. Phys.*, 105:113110, 2009. doi:10.1063/1.3132827.
- [87] O. Breitenstein, J. Bauer, D. Hinken, and K. Bothe. Towards an improved laplacian-based photoluminescence image evaluation method. *Sol. Energ. Mat. Sol. Cells.*, 142:92 101, 2015. doi:10.1016/j.solmat.2015.06.020.
- [88] F. Frühauf and O. Breitenstein. Laplacian PL image evaluation implying correction of photon scattering in the luminescence detector. *Energy Procedia*, 92:24 28, 2016. doi:10.1016/j.egypro.2016.07.005.
- [89] F. Frühauf, J. Wong, J. Bauer, and O. Breitenstein. Finite element simulation of inhomogeneous solar cells based on lock-in thermography and luminescence imaging. *Sol. Energ. Mat. Sol. Cells.*, 162:103 113, 2017. doi:10.1016/j.solmat.2016.12.037.

- [90] D. Abou-Ras, T. Kirchartz, and U. Rau. Advanced Characterization Techniques for Thin Film Solar Cells, page 41. Wiley-VCH, 2011.
- [91] M. Wolf and H. Rauschenbach. Series resistance effects on solar cell measurements. Advanced Energy Conversion, 3:455 – 479, 1963. doi:10.1016/0365-1789(63)90063-8.
- [92] A. Helbig, T. Kirchartz, R. Schaeffler, J. H. Werner, and U. Rau. Quantitative electroluminescence analysis of resistive losses in Cu(In,Ga)Se₂ thin-film modules. Sol. Energ. Mat. Sol. Cells, 94:979 984, 2010. doi:10.1016/j.solmat.2010.01.028.
- [93] M. Burgelman, P. Nollet, and S. Degrave. Modelling polycrystalline semiconductor solar cells. *Thin Solid Films*, 361:527–532, 2000. doi:10.1016/S0040-6090(99)00825-1.
- [94] S.J. Heise, V. Gerliz, M.S. Hammer, J. Ohland, J. Keller, and I. Hammer-Riedel. Light-induced changes in the minority carrier diffusion length of Cu(In,Ga)Se₂ absorber material. *Sol. Energ. Mat. Sol. Cells.*, 163:270 276, 2017. doi:10.1016/j.solmat.2017.01.045.
- [95] J.F. López Salas, S.J. Heise, M. Richter, V. Gerliz, M.S. Hammer, J. Ohland, and I. Hammer-Riedel. Simulation of metastable changes in time resolved photoluminescence of Cu(In,Ga)Se₂ thin film solar cells upon light soaking treatment. *Thin Solid Films*, pages –, 2016. doi:10.1016/j.tsf.2016.08.035.
- [96] B. E. Pieters. A free and open source finite-difference simulation tool for solar modules. In 2014 IEEE 40th Photovoltaic Specialist Conference (PVSC), pages 1370–1375, 2014.
- [97] T. C. M. Müller, T. M. H. Tran, B. E. Pieters, A. Gerber, R. Carius, and U. Rau. Effect of light soaking on the electro- and photoluminescence of Cu(In,Ga)Se₂ solar cells. *Appl. Phys. Lett.*, 103:183504, 2013. doi:10.1063/1.4827260.
- [98] T.M.H. Tran, B.E. Pieters, C. Ulbrich, A. Gerber, T. Kirchartz, and U. Rau. Transient phenomena in Cu(In,Ga)Se₂ solar modules investigated by electroluminescence imaging. *Thin Solid Films*, 535:307 310, 2013. doi:10.1016/j.tsf.2012.10.039.
- [99] D. Abou-Rasa, T. Kirchartz, and U. Rau. Advanced Characterization Techniques for Thin Film Solar Cells, page 46. Wiley-VCH, 2011.
- [100] M. Köntges, M. Siebert, D. Hinken, U. Eitner, K. Bothe, and T. Potthof. Quantitative analysis of pv-modules by electroluminescence images for quality control. In 24th European Photovoltaic Solar Energy Conference, pages 3226–3231, 2009.

- [101] A. Mansouri, M. Zettl, O. Mayer, M. Lynass, M. Bucher, O. Stern, and R. Burhenne. Defect detection in photovoltaic modules using electroluminescence imaging. In 27th European Photovoltaic Solar Energy Conference, pages 3374 – 3378, 2012.
- [102] V. Huhn, A. Gerber, Y. Augarten, B. E. Pieters, and U. Rau. Analysis of $Cu(In,Ga)Se_2$ thin-film modules by electro-modulated luminescence. *J. Appl. Phys.*, 119:095704, 2016. doi:10.1063/1.4942654.
- [103] T. C. M. Müller, B. E. Pieters, U. Rau, and T. Kirchartz. Analysis of the series resistance in pin-type thin film silicon solar cells. J. Appl. Phys., 113:134503, 2013. doi:10.1063/1.4798393.
- [104] V. Huhn, B. E. Pieters, Y. Augarten, A. Gerber, D. Hinken, and U. Rau. Imaging photocurrent collection losses in solar cells. *Appl. Phys. Lett.*, 109:223502, 2016. doi:10.1063/1.4971266.
- [105] U. Rau, V. Huhn, L. Stoicescu, M. Schneemann, Y. Augarten, A. Gerber, and B. E. Pieters. Photocurrent collection efficiency mapping of a silicon solar cell by a differential luminescence imaging technique. *Appl. Phys. Lett.*, 105:163507, 2014. doi:10.1063/1.4898008.
- [106] J. R. Carson. A generalization of the reciprocal theorem. Bell Syst. Tech. J., 3:324–346, 1924.
- [107] A. Delamarre, L. Lombez, K. Watanabe, M. Sugiyama, Y. Nakano, and J. F. Guillemoles. Experimental demonstration of optically determined solar cell current transport efficiency map. *IEEE J. Photovolt.*, 6:528–531, 2016. doi:10.1109/JPHOTOV.2016.2516249.
- [108] W. Schottky. Über spontane stromschwankungen in verschiedenen elektrizitätsleitern. Ann. Phys., 362:541–567. doi:10.1002/andp.19183622304.
- [109] H. H. Ku. Notes on the use of propagation of error formulas. *National Institute of Standards and Technology*, 9011, 1965. doi:10.6028/NBS.RPT.9011.
- [110] J. Isenberg and W. Warta. Realistic evaluation of power losses in solar cells by using thermographic methods. J. Appl. Phys., 95:5200–5209, 2004. doi:10.1063/1.1690103.
- [111] R. B. Wehrspohn, U. Rau, and A. Gombert. *Photon Management in Solar Cells*, pages 31–33. Wiley-VCH, 2015.
- [112] U. Würfel, D. Neher, A. Spies, and S. Albrecht. Impact of charge transport on current–voltage characteristics and power-conversion efficiency of organic solar cells. *Nat. Commun.*, 6:6951, 2015. doi:10.1038/ncomms7951.

- [113] Bisection method. http://mathworld.wolfram.com/Bisection.html accessed 16/05/2018.
- [114] J. C. Lagarias, J. A. Reeds, M. H. Wright, and P. E. Wright. Convergence properties of the nelder–mead simplex method in low dimensions. SIAM J. Optim., 9:112–147, 1998. doi:10.1137/S1052623496303470.
- [115] J. E. Moore, S. Dongaonkar, R. V. K. Chavali, M. A. Alam, and M. S. Lundstrom. Correlation of built-in potential and I-V crossover in thin-film solar cells. *IEEE J. Photovolt.*, 4:1138–1148, 2014. doi:10.1109/JPHOTOV.2014.2316364.
- [116] X. Sun, J. Raguse, R. Garris, C. Deline, T. Silverman, and M. A. Alam. A physics-based compact model for CIGS and CdTe solar cells: From voltage-dependent carrier collection to light-enhanced reverse breakdown. In IEEE 42nd Photovoltaic Specialist Conference (PVSC), pages 1–6, 2015.
- [117] S. S. Hegedus. Current-voltage analysis of a-Si and a-SiGe solar cells including voltage-dependent photocurrent collection. Prog.Photovolt. Res.Appl.,5:151-168,1997. doi:10.1002/(SICI)1099-159X(199705/06)5:3<151::AID-PIP167>3.0.CO;2-W.
- [118] X. X. Liu and J. R. Sites. Solar cell collection efficiency and its variation with voltage. J. Appl. Phys., 75:577–581, 1994. doi:10.1063/1.355842.
- [119] R. V. K. Chavali, J. E. Moore, X. Wang, M. A. Alam, M. S. Lundstrom, and J. L. Gray. The frozen potential approach to separate the photocurrent and diode injection current in solar cells. *IEEE J. Photovolt.*, 5:865–873, 2015. doi:10.1109/JPHOTOV.2015.2405757.

List of Abbreviations

Common Abbreviations

Acronym	Meaning
AM 1.5 G	air mass coefficient with 1.5 path length, global
CIGS	copper indium gallium diselenide
CIS	copper indium diselenide
DC	direct current
EL	electroluminescence
EM-PL	electro-modulated photoluminescence
FF	fill factor
LED	light emitting diode
MPP	maximum power point
P1	scribing line in the back contact
P2	scribing line in the absorber
P3	scribing line in the absorber and front contact
PL	photoluminescence
PPC	persistent photo conductivity
PVMOS	photovoltaic module simulator
SCAPS	solar cell capacitance simulator
SCR	space charge region
SRH	shockley-read-hall
TCO	transparent conductive oxide

Formula Abbreviations

Symbol	Description	Typical Unit
A	sample area	${ m cm}^2$
B	radiative recombination constant	$\mathrm{cm}^{3}\mathrm{s}^{-1}$
C	junction voltage calibration constant	V
C_{cell}	capacitance	\mathbf{F}
CP	collected power	\mathbf{W}
c	velocity of light	$\mathrm{ms^{-1}}$

Symbol	Description	Typical Unit
c_{stab}	stabilization parameter	ms^{-1}
χ	electron affinity	${ m eV}$
\overline{DP}	dissipated power	W
d	thickness	$\mu\mathrm{m}$
E	energy	eV
$E_{\rm field}$	electric field	$ m Vm^{-1}$
$E_{\rm g}$	band gap	eV
$E_{\rm c}$	conduction band edge	eV
$E_{\mathbf{v}}$	valence band edge	eV
E_{fn}	electron quasi Fermi-level	eV
$E_{\rm fp}$	hole quasi Fermi-level	eV
E_{T}	defect position	eV
$F_{\rm pc,glob}$	total global photocurrent collection efficiency	-
$F_{ m pc,loc}$	total local photocurrent collection efficiency	-
$f_{ m pc,glob}$	differential global photocurrent collection efficiency	-
$f_{ m pc,loc}$	differential local photocurrent collection efficiency	-
$f_{\rm pc,loc}$	approx. differential local photocurrent collection efficiency	-
$\sigma f_{ m pc,loc}$	error of differential local photocurrent collection efficiency	-
$\epsilon_{ m r}$	relative permittivity	-
η	efficiency	%
G	generation rate	${\rm cm}^{-3} {\rm s}^{-1}$
I	current	A
$I_{\rm coll,glob}$	total global collected photocurrent	A
$I_{ m ext}$	external current	A
$I_{ m ph}$	photocurrent	A
$I_{ m sc}$	short circuit current	A
J	current density	$\mathrm{Acm^{-2}}$
$J_{\rm coll,glob}$	total global collected photocurrent density	$\mathrm{Acm^{-2}}$
J_0	dark saturation current density	$\mathrm{Acm^{-2}}$
$J_{0,1/2}$	two-diode model dark saturation current densities	$\mathrm{Acm^{-2}}$
J_{MPP}	maximum power point current density	Acm^{-2}
$J_{ m e}$	electron current density	Acm^{-2}
$J_{ m h}$	hole current density	Acm^{-2}
$J_{ m R}$	current density across series resistance	Acm^{-2}
$J_{ m sc}$	short circuit current density	Acm^{-2}
$j_{ m ph}$	photocurrent density	Acm^{-2}
$j_{ m coll,loc}$	total locally collected photocurrent density	A
$\mu_{ m e}$	electron mobility	$cm^2V^{-1}s^{-1}$
$\mu_{ m h}$	hole mobility	${\rm cm}^2 {\rm V}^{-1} {\rm s}^{-1}$
$N_{ m A}$	acceptor doping	cm^{-3}
$N_{ m c}$	conduction band density of states	${\rm cm}^{-3}$

Symbol	Description	Typical Unit
$N_{ m D}$	donor doping	${ m cm^{-3}}$
NP	net Power	W
$N_{ m v}$	valence band density of states	${\rm cm}^{-3}$
$N_{ m T}$	defect density	$\mathrm{eV^{-1}cm^{-3}}$
$n_{\rm cell}$	number of cells in a module	-
$n_{ m e}$	density of electrons	${ m cm^{-3}}$
$n_{ m e,0}$	equilibrium density of electrons	cm^{-3}
$n_{ m h}$	density of holes	cm^{-3}
$n_{ m h,0}$	equilibrium density of holes	cm^{-3}
$n_{ m i}$	intrinsic charge carrier density	${ m cm}^{-3}$
n_{id}	ideality factor	-
P	power density	$ m Wm^{-2}$
P_{MPP}	maximum power density output	$ m Wm^{-2}$
ϕ^{em}	spectral luminescence distribution	$ m Wm^{-2}eV^{-1}$
ϕ^{sc}	photoluminescence signal at short circuit	$ m Wm^{-2}eV^{-1}$
$\phi_{ m bb}$	hemispherical black-body radiation	$\mathrm{Wm^{-2}eV^{-1}}$
Ψ	electrostatic potential	V
$Q_{\rm e}$	external quantum efficiency	-
$Q_{\rm cam}$	camera sensitivity	$\mathrm{W^{-1}m^2eV}$
S_{cam}	camera image	-
σ	conductivity	Scm^{-1}
$\sigma_{ m s}$	conductance of injection dependent $R_{\rm s}$	Scm^{-2}
$\sigma_{ m e}$	electron capture cross section	cm^2
$\sigma_{ m h}$	hole capture cross section	${ m cm}^2$
$\sigma^E_{ m T}$	characteristic energy of defect distribution	${ m eV}$
R	recombination rate	${\rm cm^{-3} s^{-1}}$
R_0	parameter for injection dependence of $R_{\rm s}$	Ω
$R_{\rm b}$	back contact resistance	Ω
$R_{\rm c}$	constant resistance in new equivalent circuit	$\Omega \mathrm{cm}^2$
$R_{\rm j}$	junction resistance	Ω
$R_{ m f}$	front contact resistance	Ω
$R_{ m i}$	internal series resistance	$\Omega \mathrm{cm}^2$
$R_{\rm ohm}$	ohmic resistance	$\Omega \mathrm{cm}^2$
$R_{\rm p}$	shunt resistance	$\Omega \mathrm{cm}^2$
$R_{\rm p2}$	p2 scribing line resistance	$\Omega \mathrm{cm}^2$
$R_{\rm SRH}$	shockley-read-hall recombination rate	${\rm cm}^{-3}{\rm s}^{-1}$
$R_{\rm rad}$	radiative recombination rate	$cm^{-3}s^{-1}$
$R_{\rm s}$	series resistance	$\Omega \mathrm{cm}^2$
$r_{ m j}$	differential junction resistance	Ω
$r_{\rm s}$	differential series resistance	Ω
$\Delta R_{ m s}$	change of the series resistance	$\Omega \mathrm{cm}^2$

Symbol Description Typical Unit C/m^3 space charge density ρ resistivity (conduction / valence band) $\Omega \mathrm{m}$ $\rho_{\mathrm{c/v}}$ temperature K t. time S lifetime S V voltage V $V_{\rm ext}$ external voltage $V_{\rm ext,max}$ maximum voltage within a time frame V minimum voltage within a time frame V $V_{\rm ext,min}$ average voltage within a time frame $V_{\rm ext,mean}$ $\Delta V_{\rm ext}$ change of external voltage $V_{\rm i}$ junction voltage change of junction voltage $\Delta V_{\rm i}$ V V $V_{\rm i}$ non-calibrated junction voltage maximum power point voltage V V_{MPP} V $V_{\rm oc}$ open circuit voltage $V_{\rm R}$ voltage across series resistance $V_{\rm th}$ thermal voltage thermal velocity V $v_{ m th}$ Xcounts distance vertically to solar cell surface zm

Chemical Smybols

Cu	copper
CdS	Cadmium sulfide
e	electron
Ga	gallium
h	hole
Indium	indium
Mo	molybdenum
S	sulfur
Se	selenium
ZnO	zinc oxide
ZnO:Al	aluminum doped zinc oxide
ZnO:i	intrinsic zinc oxide
$V_{ m Se}$	selenium vacancy
V_{Cu}	copper vacancy

Constants

 $\begin{array}{lll} e & \text{elementary charge} & 1.6021766208(98)\times 10^{-19} \; \text{C} \\ h & \text{Planck constant} & 4.135667662(25)\times 10^{-15} \; \text{eV s} \\ k & \text{Boltzmann constant} & 8.6173324(78)\times 10^{-5} \; \text{eV K}^{-1} \\ \epsilon_0 & \text{electric constant} & 8.854187817\times 10^{-12} \; \text{Fm}^{-1} \\ \pi & \text{pi} & 3.14159 \end{array}$

List of Publications

Journal Publications

- <u>V. Huhn</u>, B. E. Pieters, Y. Augarten, A. Gerber, D. Hinken, and U. Rau. Imaging photocurrent collection losses in solar cells, *Appl. Phys. Lett.*, 109:223502, 2016
- V. Huhn, A. Gerber, Y. Augarten, B. E. Pieters, and U. Rau. Analysis of Cu(In,Ga)Se₂ thin-film modules by electro-modulated luminescence, J. Appl. Phys., 119:095704, 2016
- A. Gerber, <u>V. Huhn</u>, T. M. H. Tran, M. Siegloch, Y. Augarten, B. E. Pieters, and U. Rau. Advanced large area characterization of thin-film solar modules by electroluminescence and thermography imaging techniques, *Sol. Energ. Mat. Sol. Cells.*, 135:35 42, 2015
- U. Rau, <u>V. Huhn</u>, L. Stoicescu, M. Schneemann, Y. Augarten, A. Gerber and B. E. Pieters. Photocurrent collection efficiency mapping of a silicon solar cell by a differential luminescence imaging technique, *Appl. Phys. Lett.*, 105:163507, 2014

Conference Presentations

with Papers

- V. Huhn, B. E. Pieters, A. Gerber, Y. Augarten and <u>U. Rau</u>. Determination and modeling of injection dependent series resistance in CIGS solar cells, 44th IEEE Photovoltaic Specialist Conference (PVSC), Washington, USA, Jun 2017, (Poster)
- V. Huhn, B. E. Pieters, Y. Augarten, A. Gerber, D. Hinken and U. Rau. Collected photocurrent imaging via electro-modulated luminescence under different illumination conditions, 43rd IEEE Photovoltaic Specialist Conference (PVSC), Portland, USA, Jun 2016, (Poster)
- <u>V. Huhn</u>, A. Gerber, B. E. Pieters, Y. Augarten, and U. Rau. Photocurrent collection efficiency mapping of CIGS solar modules by a differential

luminescence imaging technique, 30th European Photovoltaic Solar Energy Conference (EU PVSEC), Hamburg, Germany, Sep 2015, (Oral)

without Papers

- <u>V. Huhn</u>, B. E. Pieters, Y. Augarten, A. Gerber, and U. Rau. Spatially resolved determination of the absolute collected photocurrent from solar cells using electro-modulated luminescence, *32nd European Photovoltaic Solar Energy Conference (EU PVSEC)*, Munich, Germany, Jun 2016, (Oral)
- <u>V. Huhn</u>, A. Gerber, M. Schneemann, B. E. Pieters, C. Zahren, R. Schäffler, J-P. Theisen and U. Rau. Study of metastable effects in Cu(In,Ga)Se₂ solar modules during illumination and current injection, *29th European Photo-voltaic Solar Energy Conference (EU PVSEC)*, Amsterdam, Netherlands, Sep 2014, (Oral)

Curriculum Vitae

Personal details

Name Vito Konrad Wulfila Huhn

Date of birth November 1st, 1989 Place of birth Bonn, Germany

Citizenship German

Education

1996-2000	Grundschule Eckenhagen
2000-2008	Gymnasium Moltkestraße, Gummersbach
2008-2009	Civilian service at the City Hall of Reichshof
2007-2010	Bachelor of Science in Physics at the RWTH Aachen
	Bachelor thesis at the Institute of Physics
	${\bf Title:}\ Preparation\ and\ characterisation\ of\ organic\ solar\ cells$
2010-2013	Master of Science in Physics at the RWTH Aachen
	Main subject: experimental solid state physics
	Master thesis at the Forschungszentrum Jülich GmbH,
	IEK5-Photovoltaics
	Title: Study of metastable effects in CIGS solar modules by
	current/voltage characteristics and luminescence
2014-2018	PhD thesis at the Forschungszentrum Jülich GmbH,
	IEK5-Photovoltaics

Acknowledgment

This part is a big thanks to every person who supported me during the making of this thesis.

Firstly, I want to thank Prof. Dr. Rau for giving me the opportunity to write this thesis under his supervision. He was interested in my work and constantly supported me not only in the writing of this thesis, but also in the writing of publications.

I am also grateful to Prof. Dr. Jean-François Guillemoles for examining this thesis.

I want to thank Dr. Andreas Gerber for bringing me into the institute and suggested me as a possible PhD candidate. He helped me with any issue concerning my work and gave me a lot of freedom to chose my own goals. Especially on organizational question he always had an open ear.

Thanks go to Dr. Bart Pieters, whose help in the making of this thesis was more on the scientific side. He was always happy to listen to my thoughts and shared his own ideas freely. I am especially grateful to him for helping me on the aspect of simulating solar cells and for developing the awesome simulation tool PVMOS. Without this program this thesis would not have been possible. Furthermore, his input was essential to come up with the idea of injection dependent series resistance in CIGS solar cells. Additionally, his feedback during the writing of this thesis was invaluable. Bart Pieters was and remains a great teacher for me.

Furthermore, I want to thank Dr. Yael Augarten, for improving my English, valuable lessons about the luminescence of solar cells and for believing in my capabilities, which motivated me greatly. I also want to thank Andrew Wrigley for improving the luminescence imaging setup significantly by awesome programming and cable management.

A big thank also goes to Sabine Kasper, who basically has a solution to any problem you ask her and Christoph Zahren who supported me with current/voltage measurements. I am also grateful to the rest of the 'Messtechnik' group who were always helpful when asked and patiently listened to my discursive talks during the group meetings.

Another thanks goes to the partners from Manz, especially Raymund Schäffler, and Bosch who provided the samples used in this work. In this context I also want to mention the OptiCIGS project, which provided the funding of this work.

Without Dr. Johnson Wong, this work would also not have been possible as he laid the foundation for photocurrent collection efficiency imaging. He also allowed

me in the scope of the HITEC graduate school to visit him in Singapore, which was a great experience.

I am furthermore thankful to all the colleagues who supported this work especially morally, above all my office mates Daniel Weigand and Karen Wilken, but also the great football team Manuel Pomaska, Florian Staub, Alexei Richter, Jan Flohre, Phillipe Czaja, David Grabowski, Maurice Nuys, Betrand Kisife, and Aryak Singh.

I additionally want to thank:

my friends who made the studies of physics much more pleasurable Nicolas Gross-Weege, David Hübscher, Marcel Friedrichs, Daniel Böckenhoff, Arne Hollmann, Katharina Menne, Janina Felter, Kristof Keller, Marc Peiter and Jan-Michael Mol.

my best man Dominik Klinkenberg, who I know for longer than I can think,

my Family who is always there for me in any manner possible.

And last but not least I want to thank my smart, beautiful wife Carina Huhn, for bearing with me during all this work, for finding simple solutions for unsolvable problems, for helping me relax and for getting me to work.

Band / Volume 426

Proton Conduction and Gas Permeation through Polymer Electrolyte Membranes during Water Electrolysis

M. Schalenbach (2018), VI, 212 pp

ISBN: 978-3-95806-333-4

Band / Volume 427

Improved characterization of root zone soil moisture by assimilating groundwater level and surface soil moisture data in an integrated terrestrial system model

H. Zhang (2018), x, 125 pp ISBN: 978-3-95806-335-8

Band / Volume 428

Manipulation of magnetism in iron oxide nanoparticle / BaTiO₃ composites and low-dimensional iron oxide nanoparticle arrays

L. Wang (2018), VI, 151 pp ISBN: 978-3-95806-338-9

Band wurde nicht veröffentlicht. Erscheint als Schlüsseltechnologieband 180

Band / Volume 429

Characterization of spatial-temporal varying riverbed hydraulic conductivity and its role on the estimation of river-aquifer exchange fluxes with data assimilation

Q. Tang (2018), xv, 117 pp ISBN: 978-3-95806-339-6

Band / Volume 430

Der Einfluss von Wasserdampf auf den Sauerstofftransport in keramischen Hochtemperaturmembranen

F. Thaler (2018), ii, 93, XXXI pp ISBN: 978-3-95806-340-2

Band / Volume 431

Analysis & modeling of metastable photovoltaic technologies: towards dynamic photovoltaic performance models

M. Görig (2018), 246 pp ISBN: 978-3-95806-342-6

Band / Volume 432

Laser Treatment of Silicon Thin-Films for Photovoltaic Applications

C. Maurer (2018), vii, 165 pp ISBN: 978-3-95806-347-1 Band / Volume 433

Mentalitäten und Verhaltensmuster im Kontext der Energiewende in NRW

K. Schürmann & D. Schumann (Hrsg.) (2018), 236 pp

ISBN: 978-3-95806-349-5

Band / Volume 434

Adhäsionsverhalten von wässrigen Nafion-Lösungen an dispersen Phasengrenzen

A. Schulz (2018), xii, 129 pp ISBN: 978-3-95806-354-9

Band / Volume 435

Alterungs- und fehlertolerante optimale Betriebsführung eines Direktmethanol-Brennstoffzellensystems

R. Keller (2018), XX, 175 pp ISBN: 978-3-95806-355-6

Band / Volume 436

Chamber study of biogenic volatile organic compounds: plant emission, oxidation products and their OH reactivity

Y. Zhujun (2018), ix, 139 pp ISBN: 978-3-95806-356-3

Band / Volume 437

Characterization of High Temperature Polymer Electrolyte Fuel Cells

Y. Rahim (2018), iii, 162 pp ISBN: 978-3-95806-359-4

Band / Volume 438

Lattice Boltzmann Simulation in Components of Polymer Electrolyte Fuel Cell

J. Yu (2018), ii, 173 pp ISBN: 978-3-95806-360-0

Band / Volume 439

Quantitative Luminescence Imaging of Solar Cells

V. Huhn (2018), 155 pp ISBN: 978-3-95806-363-1

Weitere Schriften des Verlags im Forschungszentrum Jülich unter

http://wwwzb1.fz-juelich.de/verlagextern1/index.asp

Energie & Umwelt / Energy & Environment Band / Volume 439 ISBN 978-3-95806-363-1

